

A FIBER-OPTIC COUPLED POINT DOSIMETRY SYSTEM FOR THE
CHARACTERIZATION OF MULTI-DETECTOR COMPUTED TOMOGRAPHY

By

WILLIAM EDWARD MOLONEY

A THESIS PRESENTED TO THE GRADUATE SCHOOL
OF THE UNIVERSITY OF FLORIDA IN PARTIAL FULFILLMENT
OF THE REQUIREMENTS FOR THE DEGREE OF
MASTER OF SCIENCE

UNIVERSITY OF FLORIDA

2008

© 2008 William Moloney

To my family —
Mom, Dad, Matt, John, Rob, Liz, Pete and Connor, I love you

ACKNOWLEDGMENTS

First I would like to thank my advisor, David Hintenlang, Ph.D., for his guidance and patience during my time at the University of Florida. His teaching and tutelage have given me the knowledge and direction needed to continue my path in the field of medical physics. He has devoted invaluable time in my research, but more importantly has always held his door open to all his students and it is for his friendship that I will be forever grateful.

I would like to thank Dr. Manuel Arreola and Dr. Wesley Bolch for their time and effort in guiding my graduate career. Their invaluable instruction both in and outside the classroom has provided me with the knowledge and understanding of where I want to be both academically and professionally. I would also like to thank Dr. Alireza Haghghat for the opportunities he has afforded me here at UF. Finally, I need to thank both the faculty and staff in the Department of Nuclear & Radiological Engineering, especially Diana Dampier and Terri Sparks for making life easier on a daily basis.

Without the help and friendship of my fellow students that worked alongside me these past few years, I would not be where I am today. I would like to thank Dr. Kyle Jones, Ryan Fisher, James Winslow, and Dan Hyer for all their support, advice, and most often, their cars. It is without a doubt a reflection of our advisor that we have not only worked together well as colleagues, but have also become such great friends.

I would like to extend no small thank you to Dr. Paul J. Angiolillo for introducing me to the field of medical physics. Another special thank you goes to Dr. David Gandolfo. Their friendship and counsel kept me focused both in and outside academics when I needed it most. Their teaching and advisement helped shape my life more than I can possibly thank them for and I will never forget it.

Most importantly, I would like to thank my family and friends who mean the absolute world to me, especially my parents, Jane and Bill, to whom I owe everything. I cannot thank them enough for their time, patience, love, and support. They have instilled in their children a love and faith that is immeasurable and we love them more than anything. Finally, I need to thank Elizabeth who keeps me as level headed as I can be and who has put up with me somehow these last few months. I love her more than words can say.

TABLE OF CONTENTS

	<u>page</u>
ACKNOWLEDGMENTS	4
LIST OF TABLES	9
ABSTRACT	12
CHAPTER	
1 INTRODUCTION	14
Computed Tomography Dose	14
Computed Tomography Dose Contributors	15
Computed Tomography Dose Descriptors	15
Multiple scan average dose (MSAD)	15
Computed tomography dose index (CTDI)	15
Computed tomography dose index (CTDI) phantoms	17
Weighted and volume CTDI	17
Dose-length product (DLP)	17
Axial Scans	18
Helical Scanning	18
2 FIBER OPTICS	21
History of Fiber Optics	21
Electromagnetic Spectrum	23
Fiber Optic Properties	26
Refractive Index and Total Internal Reflection	26
Numerical Aperture	29
Light Collection Efficiency and Transmission	30
Fiber attenuation	31
Absorption	31
Scattering	31
Light leakage in the cladding	31
Bending losses	32
3 CONSTRUCTION & CHARACTERIZATION OF A FIBER-OPTIC COUPLED DOSIMETRY SYSTEM	33
Introduction	33
System Overview	33
Optical Fibers	34
Scintillation Phosphor	34
Photon Counting Head	37
Photomultiplier Tube	38

Software.....	39
System Characterization	40
Energy Dependence.....	40
Dose Linearity	40
Angular Dependence	41
Table attenuation.....	42
Radiation incidence.....	43
Angular dependence in a scattering medium	46
Conclusions	47
4 COMPUTED TOMOGRAPHY DOSE PROFILES	48
Introduction.....	48
Materials and Methods	48
Head & Body Phantoms.....	50
Tube Potential (kVp) & Tube Current-Time Product (mAs).....	50
Pitch.....	51
Slice Thickness.....	51
Results and Discussion	52
Head Phantom	52
Body Phantom	56
Pitch.....	58
Head phantom	58
Body phantom	60
Slice Thickness.....	62
Head phantom	62
Body phantom	64
Conclusions.....	67
CTDI Phantom Position	67
Head vs. Body Phantom	68
Pitch.....	69
Slice Thickness.....	70
5 COMPUTED TOMOGRAPHY DOSE INDEX	71
Introduction.....	71
CTDI ₁₀₀	71
Pencil Ion Chamber	71
Small Volume Ion Chamber.....	72
Material and Methods	74
Fiber-Optic Coupled Dosimeters.....	74
CTDI Efficiency	74
Need for Longer Phantoms.....	75
Novel method for predicting helical scan dose profiles.....	76
CTDI _{L(mm)}	80
Results and Discussion	81
CTDI ₁₀₀ Efficiency.....	81

CTDI _{L(mm)}	82
CTDI ₁₀₀ Efficiency Revisited.....	88
Conclusions.....	90
Novel Method for Predicting Helical Scan Dose Profiles.....	90
Need for Longer Phantoms.....	90
6 CONCLUSIONS	92
Prototypical Fiber-Optic Coupled Point Dosimetry System	92
Helical Computed Tomography Dose Profiles.....	92
Novel Method for Predicting Helical Scan Dose Profiles.....	94
Need for Longer Phantoms.....	94
Future Work.....	95
Extended Characterization of the Point Dosimetry System	95
Verification of Predicted Dose Profiles in Extended Length Phantoms	95
Multi-Fiber-Optic Coupled Dosimeter System	96
Anthropomorphic Phantoms.....	96
Final Thoughts.....	97
LIST OF REFERENCES.....	98
BIOGRAPHICAL SKETCH	103

LIST OF TABLES

<u>Table</u>	<u>page</u>
4-1 Helical scan dose profiles – Operating conditions.....	49
4-2 Head phantom - Ratios of integrated counts (dose) show the effect of pitch on the helical scan dose profile.....	60
4-3 Body phantom - Ratios of integrated counts (dose) show the effect of pitch on the helical scan dose profile.....	62
4-4 Head Phantom - Ratios of integrated counts (dose) show the effect of slice thickness on the helical scan dose profile.....	64
4-5 Body Phantom - Ratios of integrated counts (dose) show the effect of slice thickness on the helical scan dose profile.....	66
5-1 Helical scan dose profiles – Operating conditions.....	76
5-2 Calculated percent difference in accumulated dose across a 15 cm scan length for the measured single head phantom profile and the reflected first 7.5 cm of the 300 mm length phantom profile.....	80
5-3 CTDI ₁₀₀ efficiency (ϵ_{150}) calculated as the ratio of the accumulated dose measured in the center 100 mm of a standard PMMA phantom divided by the total 150 mm scan length of the phantom	82
5-4. Variance of ϵ_{150} efficiencies calculated from helical scan dose profiles acquired at three pitches for each combination of slice thickness and phantom position utilized	83
5-5 Accumulated dose ratios measured from helical dose profiles of 450 mm and 150 length PMMA <i>head</i> phantoms	84
5-6 Accumulated dose ratios measured from reflected helical dose profiles of 450 mm and 150 length PMMA <i>head</i> phantoms	84
5-7 Accumulated dose ratios measured from helical dose profiles of 450 mm and 150 length PMMA <i>body</i> phantoms	87
5-8 CTDI ₁₀₀ efficiency ($CTDI_{100} / CTDI_L$) calculated as the ratio of the accumulated dose measured in the center 100 mm of a standard PMMA phantom divided by the total scan length L of the phantom	88
5-9 Variance of ϵ_{450} efficiencies calculated from helical scan dose profiles acquired at the three pitches for each combination of slice thickness and phantom position utilized	88

LIST OF FIGURES

<u>Figure</u>	<u>page</u>
1-1 Single scan dose profile $f(x)$ convolved with rectangular function $\Pi(x/L)$ to produce the cumulative dose profile $D(x)$, where L represents the total helical scan length.....	20
2-1 Optical fiber and cladding.....	22
2-2 The electromagnetic spectrum.....	24
2-3 Wave-particle duality of light.....	25
2-4 Light refraction in glass.....	27
2-5 Light refraction through different media.....	28
2-6 Refraction and total internal reflection.....	28
2-7 Total internal reflection.....	29
2-8 Numerical aperture.....	30
2-9 Bending losses.....	32
3-1 Diagram of the fiber-optic coupled dosimetry system and component.....	34
3-2 Photo of typical optical fiber dosimeter assembly.....	35
3-3 X-ray interactions probability.....	35
3-4 Probability of photoelectric absorption for gadolinium oxy-sulfate as a function of incident photon energy.....	36
3-5 Spectral output of gadolinium oxy-sulfate light photons.....	36
3-6 Photo of photon counting head and housing.....	37
3-7 Diagram of photomultiplier tube used in the fiber-optic coupled dosimeter.....	38
3-8 Spectral response of H7467 photon counting head and photomultiplier tube.....	39
3-9 Tube potential (energy) dependence of the fiber-optic coupled dosimeter.....	41
3-10 Dose linearity of the fiber-optic coupled dosimeter.....	41
3-11 CT tube angular dependence and table attenuation.....	42
3-12 Fiber-optic coupled dosimeter's angular dependence.....	44

3-13	Angular dependence of several fiber optic coupled dosimeters	45
3-14	FOCD angular dependence in a scattering medium	46
4-1	Photograph of the standard PMMA CTDI phantoms	49
4-2	Comparison of measured data in the five positions of the CTDI head phantom. Center and four peripheral (left and right responses are identical) measurement locations indicated	53
4-3	Expanded view of the helical dose profile measured in the 12 o'clock (top) position of the CTDI head phantom	54
4-4	Expanded view of the helical dose profile measured in the center position of the CTDI head phantom.....	55
4-5	Comparison of measured data in the five modules of the CTDI body phantom: center and four peripheries.....	57
4-6	Effect of pitch on measured helical dose profiles in the CTDI head phantom.....	59
4-7	Effect of pitch on measured helical dose profiles in the CTDI body phantom.....	61
4-8	Effect of slice thickness on measured helical dose profiles in the CTDI head phantom...63	
4-9	Effect of slice thickness on measured helical dose profiles in the CTDI body phantom.....	65
5-1	Diagram of the 300 mm length phantom setup.....	77
5-2	Helical scan dose profiles in the center position of CTDI head phantoms measured with fiber-optic coupled dosimeters.....	78
5-3	Helical scan dose profiles in the 12 o'clock position of CTDI head phantoms measured with fiber-optic coupled dosimeters	79
5-4	Helical scan dose profiles in the center position of CTDI head phantoms measured with fiber-optic coupled dosimeters.....	86
5-5	Helical scan dose profiles in the 12 o'clock (top) position of CTDI head phantoms measured with fiber-optic coupled dosimeters	87

Abstract of Thesis Presented to the Graduate School
of the University of Florida in Partial Fulfillment of the
Requirements for the Degree of Master of Science

A FIBER-OPTIC COUPLED POINT DOSIMETRY SYSTEM FOR THE
CHARACTERIZATION OF MULTI-DETECTOR COMPUTED TOMOGRAPHY

By

William Edward Moloney

August 2008

Chair: David Hintenlang
Major: Nuclear Engineering Sciences

The importance of radiation dose and the associated risk from x-ray computed tomography (CT) has been highlighted by the scientific community as recent developments in technology have greatly improved the capabilities of CT scanners. As image quality rapidly improves, it is necessary to quantify the radiation dose delivered from new imaging modalities, and evaluate the means for reducing patient dose to as low a level as possible. Developments in computed tomography technology have thus offered a change in the clinical use of CT, prompting the need to evaluate the radiation risk versus medical benefit and calling into question traditional dosimetry methods that may no longer be applicable to new scanner capabilities.

The goal of this work was to develop a prototype point dosimeter for the characterization of the radiation dose associated with diagnostic imaging modalities. A fiber-optic coupled point dosimetry system was constructed based on the scintillation properties of a gadolinium oxy-sulfate phosphor coupled to a fused silica optical fiber. The dosimeter system was then evaluated for its performance across the diagnostic energy range and implemented in profiling the dose delivery methods of helical, multi-detector computed tomography (MDCT).

The fiber-optic coupled (FOC) dosimeters showed strong sensitivity, reproducibility, and excellent dose linearity in the diagnostic range and provided remote, real-time detection of the dose associated with helical CT. Helical scan dose profiles measured with FOC dosimeters provided information of CT characteristics that traditional computed tomography dosimetry metrics lacks, specifically the isolation of the effects of primary and scatter radiation. The dose profiles display the attenuation and scatter effects of phantom size, length, and position, and quantify the effect of changes in CT scan parameters (pitch and slice thickness) on the absorbed dose to the patient.

The evaluation of the computed tomography dose index and its efficiency in predicting the dose delivered from clinically relevant scan lengths has shown that the standard 100 mm long pencil ion chamber synonymous with CT dosimetry fails to sufficiently measure the dose due to scatter radiation for scan lengths longer than 100 mm. The analysis of helical dose profiles show that the $CTDI_{100}$ metric greatly underestimates dose for large phantom diameters and calls for the use of longer length phantoms for computed tomography dose measurements.

CHAPTER 1 INTRODUCTION

The importance of radiation dose and the associated risk from x-ray computed tomography (CT) has been highlighted by the scientific community as recent developments in technology have greatly improved the capabilities of CT scanners.¹⁻³ With the introduction of helical CT in the early 1990s came the implementation of multi-detector as well as multi-slice systems.⁴⁻⁷ The number of slices acquired per axial rotation has increased greatly from 16- and 64- slice systems to recently developed 256-slice scanners.⁸ Developments in computed tomography technology have thus offered a change in the clinical use of CT, prompting the need to evaluate the radiation risk versus medical benefit.

According to 2006 data, approximately 62 million CT examinations were performed in hospitals and outpatient imaging facilities in the United States.⁹ The dose levels imparted in CT exceed those from conventional radiography and fluoroscopy. Furthermore, its use continues to grow, making CT a significant contributor to the total collective dose delivered to the public from medical procedures involving ionizing radiation.¹⁰⁻¹¹

Computed Tomography Dose

Mettler et al. state that the increasing use of computed tomography in clinical practices coupled with its relatively high radiation doses compared to general radiography makes CT a significant contributor to patient population dose from medical x-rays.¹⁰⁻¹¹ It is therefore necessary to establish an accurate and easily reproducible method for CT dosimetry. Fundamental definitions of CT dose parameters require review and possibly reinterpretation with advances in CT technology. Traditional CT parameters have not been used consistently (or are even out of date), while some may be more relevant than others with respect to patient risk or new scanner capabilities.

Computed Tomography Dose Contributors

Four aspects of CT image acquisition are unique in comparison to x-ray projection imaging. First, the volume of tissue being irradiated by the primary beam is much smaller. Second, the volume of tissue being irradiated is exposed from almost all angles, and thus the dose is more evenly distributed to the tissues in the beam. Third, CT requires a high signal to noise ratio to achieve higher contrast resolution, and therefore the higher techniques (kV and mAs) lead to higher dose to the slice volume. Finally, scatter radiation is a significant contributor to CT radiation dose. Compton scattering is the principle interaction mechanism in CT and the scatter dose can often be higher than that of the primary beam. The acquisition of a CT slice also delivers a considerable amount of dose from scatter to adjacent tissues outside the collimated primary beam.¹²

Computed Tomography Dose Descriptors

Quality assurance programs and optimization procedures in diagnostic radiology require the assessment of patient doses. Commonly adopted dose descriptors based on phantom measurements that are easy to measure and define are described below. They include the MSAD and the CTDI.

Multiple scan average dose (MSAD)

The multiple scan average dose (MSAD) is the standard for CT radiation dosimetry. It is defined by the International Atomic Energy Agency (IAEA) as the average dose, at a particular depth from the surface, resulting from a large series of CT slices.¹²⁻¹³ It is the dose to tissue including the dose that is attributable to scattered radiation from all adjacent slices.

Computed tomography dose index (CTDI)

An estimate of the MSAD can be accomplished with a measurement of the CTDI (Computed Tomography Dose Index).¹⁴ $CTDI_{FDA}$ is defined by the U.S. Food and Drug

Administration as the radiation dose to any point in the patient including the scatter radiation contribution from 7 CT slices in both directions, for a total of 14 slices.¹⁵

One method used to measure the $CTDI_{FDA}$ is with an array of thermoluminescent dosimeters (TLDs) placed in holes along 14-slice thickness increments in a specified CTDI phantom. A single CT slice is acquired at the center of the array, and the $CTDI_{FDA}$ is determined by summing the individual TLD dose measurements. Another $CTDI_{FDA}$ measurement method requires the use of a thin pencil ionization chamber.¹⁶⁻¹⁷

Whether it is an ion chamber or TLD array, the length of the detector must be long enough to average the variations produced by the scan interval, but not so long that the average is distorted by the dose fall off at the edge of the scan length. As a result, $CTDI_{FDA}$ can greatly underestimate the MSAD for small slice thicknesses, because a significant amount of radiation is scattered beyond seven slice thicknesses and $CTDI_{FDA}$ defines no standardization of slice width in determining dose measurements.

A much better CT Dose Index has been defined by the IEC as the exposure measured over a 100 mm length for *all* slice thicknesses.¹⁸ This $CTDI_{100}$ uses a 10 cm long, 3 cc pencil ion chamber and a single CT slice is produced at the center of the chamber in the standardized CTDI phantoms described below. The active area of the pencil chamber provides an “exposure reading” that represents an average exposure (air kerma) over the chamber length (100 mm).

$$CTDI_{100} \text{ (rad or Gy)} = \frac{C \cdot f(\text{rad/R}) \cdot 100 \text{ (mm)} \cdot \text{exposure reading } (R)}{N \cdot T(\text{mm})} \quad (1-1)$$

where R is the exposure reading, T is the slice thickness, N is the number of slices, C is the temperature and pressure corrected chamber calibration factor, and f is the appropriate exposure-to-dose conversion factor.

Computed tomography dose index (CTDI) phantoms

Specified CTDI phantoms are composed of polymethylmethacrylate (PMMA) and are 15 cm in length, with diameters of 16 and 32 cm corresponding to the head and body phantoms, respectively.^{2-3,19} There are five drilled holes parallel to the z axis (couch direction) to allow for the placement of dosimeters for the measurement of the central and peripheral (top, left, right, and bottom, with respect to the couch and at 1 cm from the surface) CTDI.

Weighted and volume CTDI

The weighted CTDI is defined as

$$\text{CTDI}_{(w)} = \frac{1}{3} \text{CTDI}_{(c)} + \frac{2}{3} \text{CTDI}_{(p)} \quad (1-2)$$

where $\text{CTDI}_{(c)}$ is the central CTDI and $\text{CTDI}_{(p)}$ is the average of all four peripherals.²⁰⁻²¹ The volume CTDI (CTDI_{vol}) is then used to represent the dose for a specific scan protocol, usually involving a series of scans and taking into account protocol-specific information such as pitch. It is defined as

$$\text{CTDI}_{\text{vol}} = \frac{N \times T}{I} \text{CTDI}_{(w)} = \frac{1}{\text{pitch}} \text{CTDI}_{(w)} \quad (1-3)$$

where I is the table increment (mm) per axial scan.

Dose-length product (DLP)

CTDI_{vol} only estimates the average dose for a 100 mm scan length even though the actual volume-averaged dose will increase with scan length. A better representation of the overall energy delivered by a given protocol is to integrate the absorbed dose along the scan length.

This metric is known as the Dose-Length Product (DLP):

$$\text{DLP (mGy} \cdot \text{cm)} = \text{CTDI}_{\text{vol}} \text{ (mGy)} \times \text{scan length (cm)} \quad (1-4)$$

The DLP thus reflects the total energy absorbed due to a complete scan acquisition and offers a potential for quantifying biological effect.

Axial Scans

For a narrow, fan-shaped beam of x rays rotating around a CT phantom in the (x,y) plane producing a single slice image (or for multiple slices through consecutive rotations with couch movement in the z direction between scans), the CTDI may be defined by the formula

$$\text{CTDI}_{\infty} = \frac{1}{T} \int_{-\infty}^{+\infty} D(z) dz \quad (1-5)$$

where $D(z)$ is the single, axial scan dose profile (sum of the primary radiation within the imaged volume and the scattered radiation within and outside the imaged volume) along a line parallel to the z axis of the scanner for nominal slice thickness T .²² For multiple slices through consecutive rotations with couch movement in the z direction between scans, the formula requires division by the number of slices N in a single scan. In clinical applications, the integration in Eq. (1-5) is carried out for either a total thickness of 14 slices (CTDI_{FDA}) or 100 mm (CTDI_{100}).²³⁻²⁴

While the CTDI_{100} remains an accurate prediction of MSAD for axial CT, it begins to fail for multiple scan dose profiles of pitch $\neq 1$ and for helical CT scanning. This method of measuring the integral of the single-slice dose profile using a 10 cm long ion chamber to predict the MSAD can greatly underestimate dose as radiation beam widths for multi-slice scanners get wider. If the ion chamber is not long enough to integrate the total areas under the single slice dose profile (Eq. 3-4), the scatter tails of the beam profile are omitted, thus underestimating the dose significantly.²⁵

Helical Scanning

Metrics, introduced by *Robert Dixon*, based on the use of convolution mathematics to evaluate CT scan dose profiles provide a method of dosimetry where the 10 cm ion chamber

fails.²⁶ In helical CT, continuous translation of the single-scan dose profile results in a continuum of contributions to the cumulative dose profile. To visualize this, consider a helical scan in which the table and phantom are translated along the longitudinal axis with constant velocity v . Let $f(x)$ be the single slice axial dose profile that travels a length L of the phantom (from $-L/2$ to $L/2$). The cumulative dose profile can thus be obtained by integrating across the entire scan length,

$$D(x) = \frac{1}{v\tau} \int_{-L/2}^{+L/2} f(x) dx \quad (1-6)$$

where τ is the time for one rotation of the scanner.

Figure 1-1 displays the single slice dose profile $f(x)$. It can be seen that the maximum dose, $D(x=0)$, occurs in the center of the scan length. The right side of the figure displays the convolution of the single slice dose profile $f(x)$ with the rectangular function $\Pi(x/L)$, which has unit height and width L . The cumulative dose profile $D(x)$ builds up as the single slice profile slides into the box $(-L/2, L/2)$ and the product integrated. The dose in the central region flattens out and reaches an equilibrium value when L is large enough to encompass the scatter tails of $f(x)$.²⁶⁻²⁷ The equilibrium dose value is then given by

$$D_{eq}(0) = \frac{1}{v\tau} \int_{-\infty}^{+\infty} f(x) dx \quad (1-7)$$

Physically measured dose profiles will have an accumulated dose $D(x)$ that is non-uniform. Instead it is useful to obtain the line integral of the dose along the axis. This metric is the dose line integral (DLI) and is analogous to the dose-length product discussed earlier.²⁶

$$DLI = \int_{-\infty}^{+\infty} D(x) dx = \frac{1}{v\tau} \int_{-\infty}^{+\infty} f(x) dx = L \cdot D_{eq}(0) \quad (1-8)$$

The infinite integration limits represent the true dose-length product and include the scatter tails distributed beyond the interval $(-L/2, L/2)$.

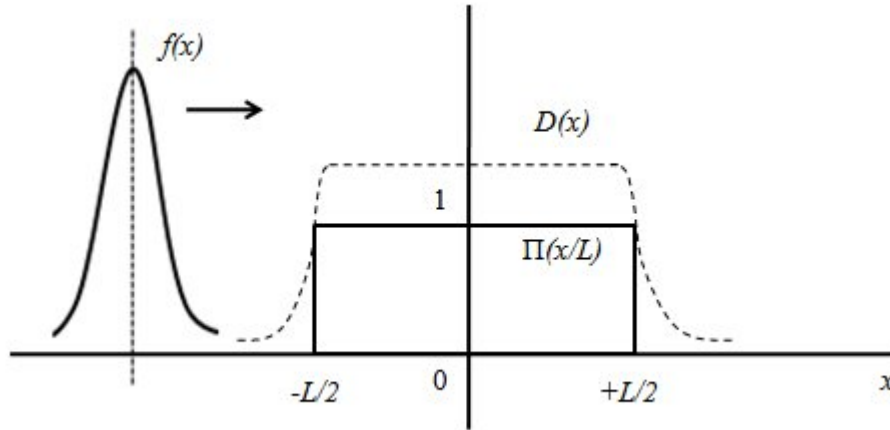


Figure 1-1. Single scan dose profile $f(x)$ convolved with rectangular function $\Pi(x/L)$ to produce the cumulative dose profile $D(x)$, where L represents the total helical scan length

The cumulative dose profile and the dose line integral are thus generated from the single slice dose profiles using a convolution across the scan length and scan lengths utilized by most clinical exams are long enough such that the dose equilibrium in the central region should be reached.²⁶ Thus, the equilibrium dose can be measured with a single dose profile if the chamber is long enough to encompass all the scatter tail radiation resulting from the scan. The use of a small volume ion chamber to directly measure the cumulative dose $D(x)$ at any point by scanning a length of phantom long enough to produce dose equilibrium in the center has the same result as making the chamber longer and is indeed more accurate for wide beam profiles. Even if the scan length L is not long enough to produce equilibrium at the center, such a small chamber will give a good measurement of the maximum dose, since the dose distribution is relatively flat in the center, and a 10 cm chamber will merely give the average dose over the central 10 cm of the scan length. The introduction of a small ion chamber to measure the flat, center of the helical dose profile allows for the determination of important dose profile characteristics and thus leads to a more accurate prediction of MSAD for cone-beam, helical computed tomography.

CHAPTER 2 FIBER OPTICS

Though they have risen into a booming industry in the field of communications technology, fiber optics evolved from devices designed to guide light for illumination. They were first used to look inside the human body, and are still used today as imaging tools in endoscopy and colonoscopy. Historically, optical fibers have also offered a unique capability of radiation monitoring. The development of a fiber-optic coupled dosimetry system will show further use of this rising technology in medical applications, specifically in the area of radiation detection and dose calculation. This point detector will provide remote, real-time dose measurements and allow for the direct recording of the radiation characteristics of modern x-ray technologies.

History of Fiber Optics

In 1880, engineer William Wheeler patented a way to pipe light through buildings. He wanted to distribute light from a light source known as an electric arc to distant rooms within a building through a set of pipes coated with a reflective layer, where diffusers at the end of each pipe would spread the light out. At the time, air was a much clearer medium than any known solid, and though logical, his idea never caught on. However, by the early 1900s, a scheme for bending light through a bent glass rod was created to illuminate the inside of the mouth for dentistry.²⁸

Through a phenomenon known as total internal reflection, light can be confined inside glass or another transparent material. The light is sent through the material in such a way that it strikes the surface exposed to air at a glancing angle. The light is then reflected back into the solid. A fine glass fiber is actually a very thin, flexible rod, so it can guide light in much the same way.

The use of fiber optics for medical imaging purposes took its first steps in the 1920s, as glass fibers were assembled into bundles. The first image-transmitting bundles were not consistently effective due to the use of bare fibers. As the fibers touched and scratched, light was able to leak at the surface when exposed to air. Total internal reflection occurs when light traveling in one medium tries to enter another medium with a lower refractive index. Air has a much lower refractive index than glass, but the difference need not be large. Coating the glass fiber with such a material can allow for total internal reflection, while still protecting the surface of the fiber from scratches, fingerprints, and light leakage into other glass fibers (Figure 2-1).²⁸

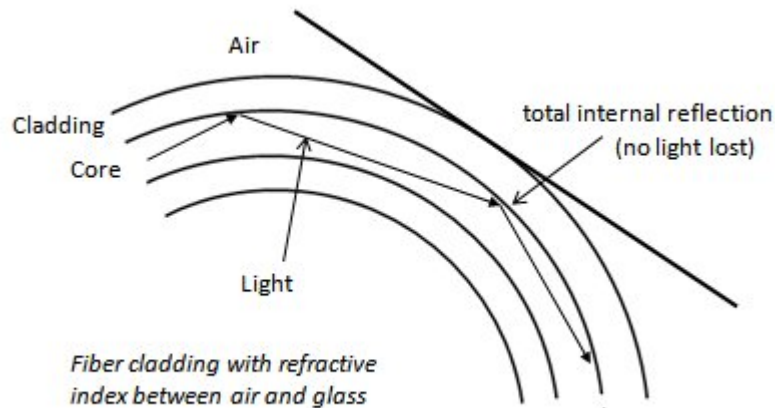


Figure 2-1. Optical fiber and cladding

In the 1950s, scientists, engineers, and students alike discovered this more practical use of fiber bundles and went as far as coating the glass rods with oils, margarine, beeswax, and finally different plastics. In December 1956, a University of Michigan undergraduate student by the name of Larry Curtiss slipped a rod of glass with a high refractive index into a lower indexed tube of glass, making the first glass-clad fiber. Technology has improved since then, but glass-clad fibers remain in common use, and fiber bundles have been used extensively in imaging and illumination.²⁸

The early use of optical fibers was limited by signal loss as the original endoscopes lost half of the light they carried after 3 meters. With the same fibers, only 0.1% of the light remained after 30 meters. While this can be acceptable for use over short distances, long distance applications such as in communications would be deemed impossible.

It was in the late 1960s that two engineers at Standard Telecommunications Laboratories in England, Charles K. Kao and George Hockham, discovered that most of the loss in fiber glass was due to impurities and the development of highly purified glass would prove them right. Today's best fibers allow for 10% remaining light after a distance of 50 kilometers.²⁸

Electromagnetic Spectrum

Understanding the fundamental properties of fiber optics requires a basic review of the principles that guide light's interaction with matter in the field of optics. Optics is the branch of physics that describes the behavior and properties of light and the interaction of light with matter. Light makes up only a small part of the spectrum of electromagnetic radiation and the wave-particle duality of modern physics allows us to consider light to be either electromagnetic waves or photons that travel at the speed of light, c (2.998×10^8 m/s). The difference between radiations in the electromagnetic spectrum can be measured in several ways: the length of the wave, the energy of a photon, or as the oscillation frequency of an electromagnetic field (Figure 2-2).

Viewed as an electromagnetic wave, light is composed of electric and magnetic fields, which are perpendicular to each other and to the direction in which the light travels as shown in Figure 2-3a. The amplitude of each field varies sinusoidally. The wavelength, λ , is defined as the distance that light travels during one complete cycle (rising from zero to a positive peak, going back through zero to a negative peak, then returning to zero) and is measured in meters, micrometers (μm or 10^{-6} m), or nanometers (nm or 10^{-9} m). The frequency, ν (measured in

hertz), is described as the number of waves or cycles per second (cps). Wavelength decreases as frequency increases, and waves can be characterized by either.

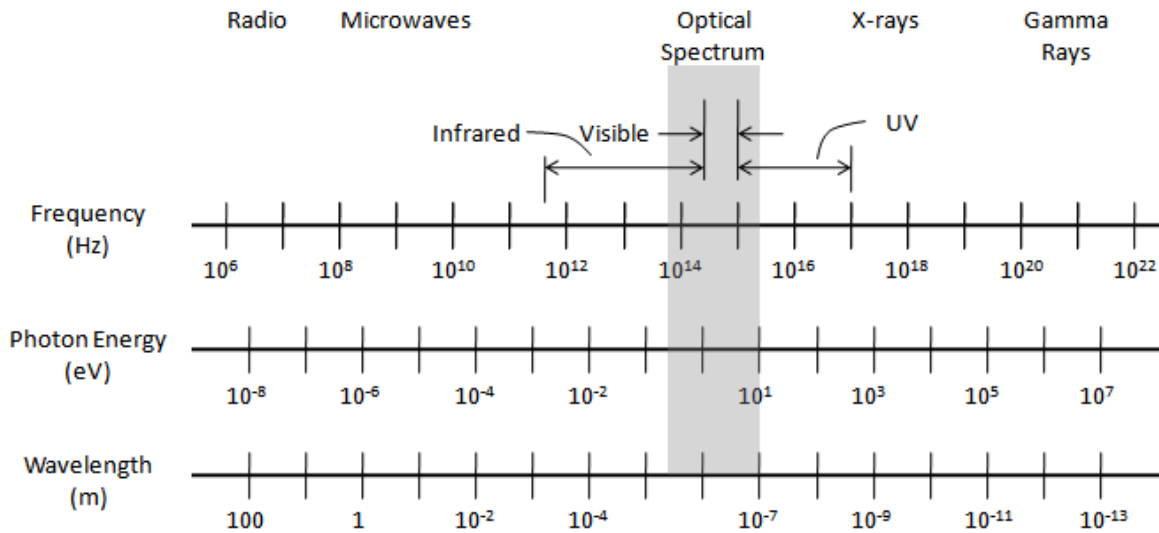


Figure 2-2. The electromagnetic spectrum.

A photon is a quantum of electromagnetic energy or wave packet, a series of waves that build quickly to a peak amplitude, and then fade back to nothing (Figure 2-3b). The pulse or wave packet has the same characteristics as the electromagnetic waves described above; however, the wavelength and frequency are not as well defined as in a continuous sine wave. The uncertainty principle tells us that the shorter the pulse, the larger the uncertainty in wavelength.

The amount of energy carried by a single photon depends on the oscillation frequency. The faster the wave oscillates, the higher the energy. Thus, each photon has a unit of energy set by the wavelength or frequency. A continuous wave is then a series of photons emitted one after the other, and the total energy is the number of photons times that photon energy. In wave terms, that is proportional to the wave amplitude squared.

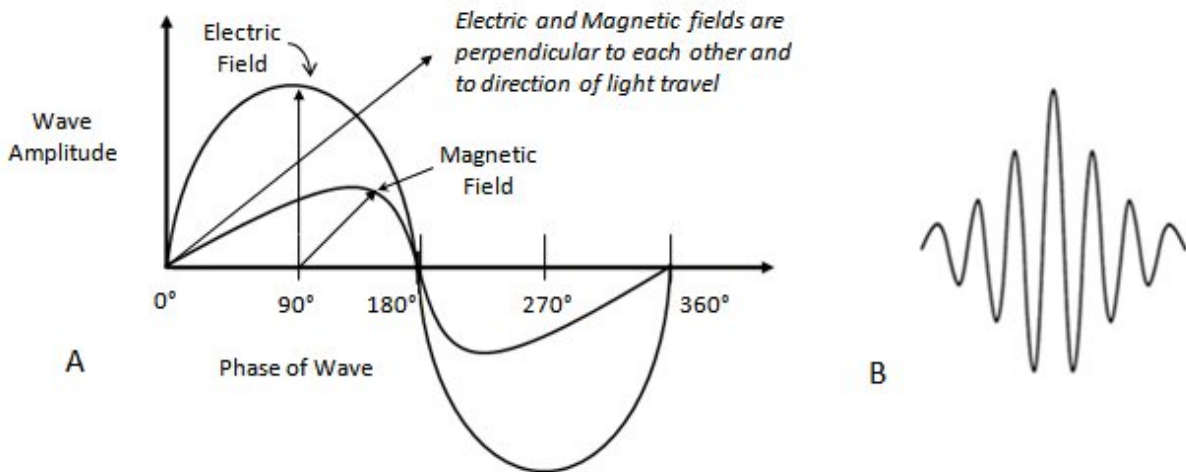


Figure 2-3. Wave-particle duality of light. A) Wave consisting of electric and magnetic fields. B) A photon, quantum of energy, or wave packet.

Referring back to Figure 2-2, all the measurement units on the spectrum chart are different ways to measure the same thing, and there are simple conversion methods between them.

Wavelength is inversely proportional to frequency,

$$\text{wavelength} = \frac{c}{\text{frequency}} \quad \text{or} \quad \lambda \text{ (m)} = \frac{c \text{ (m/s)}}{\nu \text{ (Hz)}} \quad (2-1)$$

Photon energy can be measured from Planck's law, which states

$$E \text{ (Joules)} = h\nu \quad (2-2)$$

where h is Planck's constant (6.626×10^{-34} J·s, or 4.136×10^{-15} eV·s). But since our interest lies in the part of the spectrum measured in wavelength, a more useful formula is

$$E \text{ (eV)} = \frac{1.2399}{\lambda \text{ (\mu m)}} \quad (2-3)$$

which gives energy in electron volts (the energy that an electron gains in moving through a 1 volt electric field) when wavelength is measured in micrometers (μm).

Looking again at Figure 2-2, the interest of this paper is in the region labeled "The Optical Spectrum", where optical fibers function. This region includes the light visible to the human eye

(400 to 700 nm) and nearby parts of the infrared or our interest, the ultraviolet, where fused silica fibers can transmit light over short distances.

Fiber Optic Properties

Refractive Index and Total Internal Reflection

The characterization and understanding of the path that light travels has been the precursor to the development of fiber optic applications. There is a noticeable difference of speed as light travels through varying transparent materials. The refractive index, n , is the speed of light in a vacuum, c , divided by the speed of light in a material:

$$n = \frac{c_{\text{vacuum}}}{c_{\text{material}}} \quad (2-4)$$

The change in speed of light when traveling from one material into another is an effect known as refraction. Figure 2-4 depicts what happens to the peaks of light waves as they enter glass from air. The waves in air continue at the same speed until they reach the surface of the glass, where they slow down. As the waves hit the glass at an angle, some light enters the glass while the rest remain in the air. The frequency of the wave does not change as the waves slow down in glass, but the distance traveled between peaks is shortened.²⁸

This slowing process bends the path of light. The amount of bend that the light experiences depends on the refractive indexes of the two materials and the angle of incidence at the surface. Snell's law states:

$$n_i \sin I = n_r \sin R \quad (2-5)$$

where n_i and n_r are the refractive indexes of the initial medium and the medium into which the light is refracted, while I and R are the angles of incidence and refraction of the transmitted light relative to the normal, as seen in Figure 2-4.

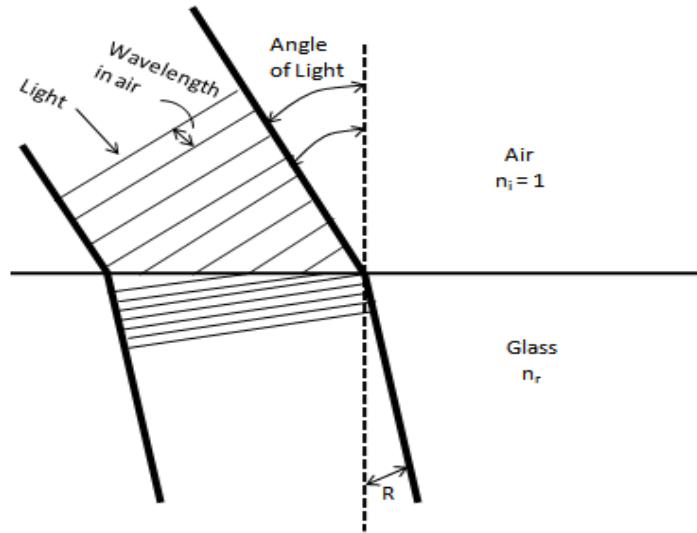


Figure 2-4. Light refraction in glass

The above description explains the standard example of light traveling from air into glass. The opposite, light emerging into air from glass, is shown in Figure 2-5. The process of refraction is reversed, and if the front and rear surfaces of a glass window are flat, the net refraction is zero. If we look at the refraction of a lens, however, light emerges at a different angle than when it entered the glass. When light in a medium with a high refractive index (glass) interfaces with a medium of low refractive index (air), the light is bent farther away from the normal; i.e. according to Snell's law, the angle of refraction is greater than the angle of incidence ($R > I$, or $\theta_2 > \theta_1$). This is not a problem for small angles of incidence, but when the angle of incidence becomes too large, refraction cannot occur.²⁸

If the angle of incidence exceeds a critical angle, where the sine of the angle of refraction would be equal to 1.0, light cannot get out of the glass. Instead total internal reflection occurs as shown in Figure 2-6. The critical angle above which total internal reflection takes place can be derived from Snell's law,

$$\theta_{\text{critical}} = \arcsin \left(\frac{n_r}{n_i} \right) \quad (2-6)$$

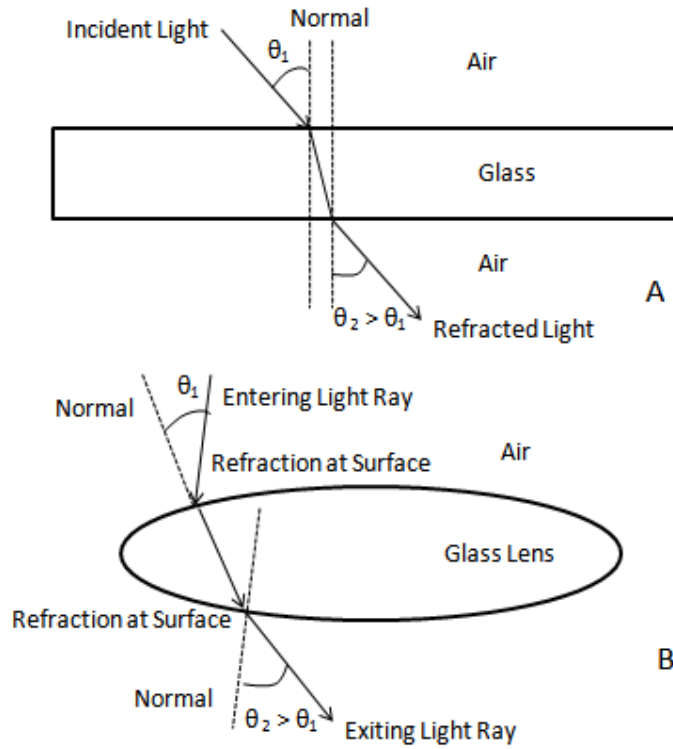


Figure 2-5. Light refraction through different media. A) Window. B) Lens.

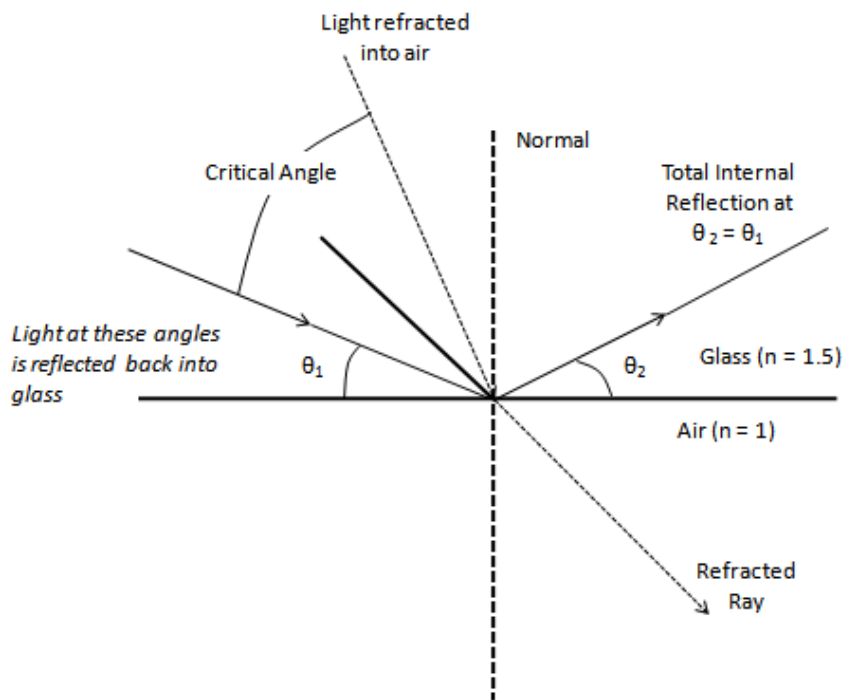


Figure 2-6. Refraction and total internal reflection

Numerical Aperture

Optical fibers are made of glass which can be inherently strong when not cracked and extremely flexible when thin. The comparison is often made to human hair, and though fibers are much stiffer, when well made, they can be much smoother than hair. A small light-guiding core, which can be as thin as a few microns, is surrounded by a glass cladding. A plastic coating covers the entire fiber, protecting its surface from scratches and microcracks that can cause signal loss or the fiber itself to break.

The refractive index of the core is higher than that of the cladding, so light striking the interface at a glancing angle is confined in the core by total internal reflection, Figure 2-6. The difference, however, need not be large. For a 1% difference (i.e. $n_r/n_i = 0.99$), the critical angle, θ_{critical} , measured from the normal is approximately 82° . Figure 2-7 shows us that any light striking the cladding at an angle of 8° or less will be confined in the core. This upper limit is called the confinement angle, $\theta_{\text{confinement}}$, of the fiber.²⁸

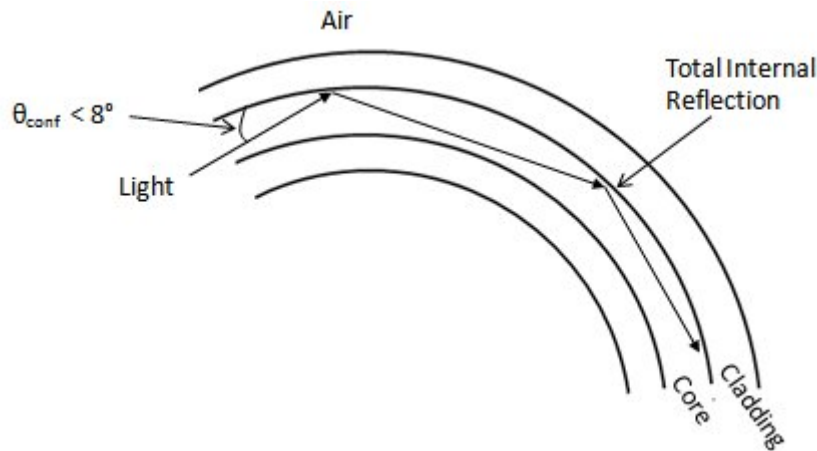


Figure 2-7. Total internal reflection

Another way to characterize the light guiding capabilities of an optic fiber is by looking at the angle over which light rays entering the fiber will be guided successfully along its core, Figure 2-8. This acceptance angle differs from the confinement angle described above because it

is instead measured in air. The acceptance angle is measured as the numerical aperture (NA), which for light entering a fiber from air is approximately

$$NA = \sqrt{(n_o^2 - n_l^2)} \quad (2-7)$$

where n_o is the refractive index of the core and n_l is the refractive index of the cladding. Again using the example of a 1% difference between core ($n_o = 1.5$) and cladding ($n_l = 1.485$), $NA = 0.21$. As seen in Figure 2.8, refraction bends a light ray entering the fiber so that it is at a smaller angle to the fiber axis than it was in the air. The sine of θ in the figure, or half the acceptance angle (12°), is larger than the confinement angle (8°), with the difference being the refractive index of the core. Thus another way to define the numerical aperture of a fiber is

$$NA = \sin \theta = n_o \sin \theta_{\text{confinement}} \quad (2-8)$$

Light Collection Efficiency and Transmission

Collecting light efficiently is an obvious desire when using optical fibers for detection purposes. Coupling light effectively into the fiber, whether from an external source or from one fiber to the another, requires both focusing external light onto the core and aligning within the fiber's acceptance angle. Other inherent factors in optical fibers that contribute to some signal loss include absorption, scattering, and leakage of light from the fiber core.

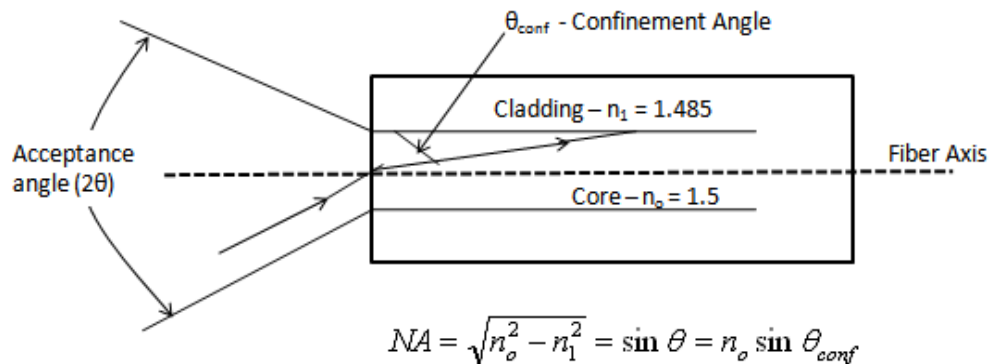


Figure 2-8. Numerical aperture

Fiber attenuation

The attenuation of an optical fiber measures the amount of light lost between input and output. Total attenuation is the sum of all losses. It is dominated by imperfect light coupling into the fiber and absorption and scattering within the fiber. Absorption and scattering are both cumulative over the length of a fiber, increasing with distance. Coupling losses, however, occur only at the ends of the fiber. For long fibers, absorption and scattering losses dominate. Conversely, they may be much smaller for shorter fibers, where coupling losses dominate.

Absorption

Although optical fibers are made of pure glass, they still absorb a tiny fraction of the light passing through them. How much depends on the wavelength of the light and any impurities in the glass. While impurities can cause strong absorption, even pure silica has some absorption while transmitting most of the light that enters it; however, absorption is uniform. The same amount of material absorbs the same amount of light at the same wavelength. Absorption is also cumulative. A material absorbs the same fraction of light for each unit length.

Scattering

Scattering reflects light in other directions, so it escapes from the fiber core and is lost from the signal. The atoms in the glass cause *Rayleigh scattering* of the light waves. Scattering depends not on the specific type of material, but on the size of the particles relative to the wavelength of light. The closer the wavelength is to the particles size, the more scattering. Like absorption, it is inherent in all fiber materials, but is generally small, increasing at shorter wavelengths. Scattering is also both uniform and cumulative as in fiber absorption.

Light leakage in the cladding

Light leakage also occurs when light escapes from the fiber core into the cladding at an angle greater than the confinement angle discussed earlier. To prevent this, fibers are coated

with a plastic that has a higher refractive index higher than that of the cladding, preventing total internal reflection.

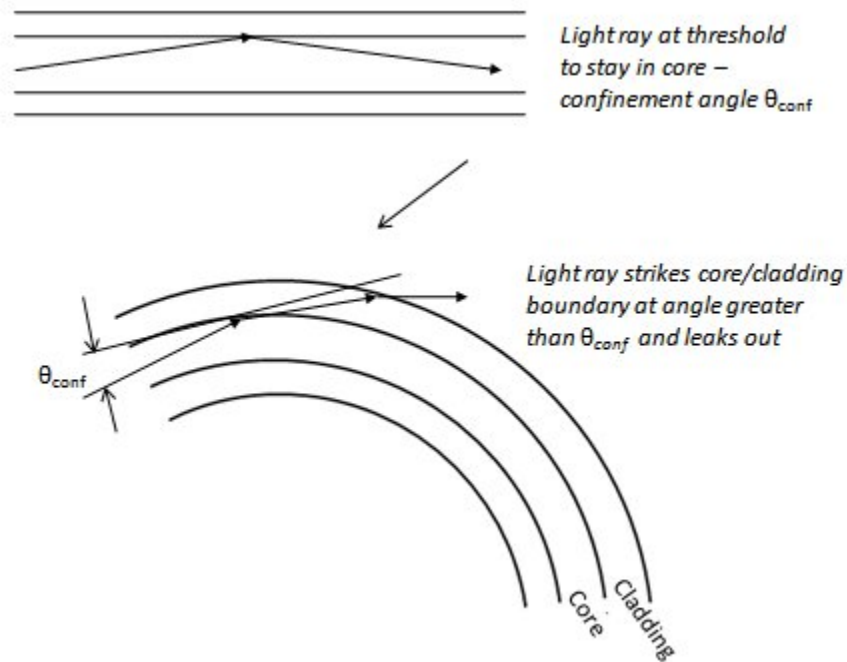


Figure 2-9. Bending losses

Bending losses

Significant losses can also arise if a fiber is bent so sharply that light strikes the cladding interface at a large enough angle that the light can leak out. When the fiber is straight, light falls within the confinement angle. Bending the fiber changes the angle at which light hits the core-cladding boundary, as seen in Figure 2-9. If the bend is sharp enough, light hits the boundary at an angle outside the confinement angle, and is refracted into the cladding where it can leak out. There are two types of bending loss. *Macrobends* are single bends, visible to the naked eye, while *microbends* are tiny kinks or ripples that can form along the length of the fiber.

CHAPTER 3 CONSTRUCTION & CHARACTERIZATION OF A FIBER-OPTIC COUPLED DOSIMETRY SYSTEM

Introduction

Optical fibers have offered the unique capability of remotely monitoring radiation in difficult to access and/or hazardous locations.²⁹ Optical measurement methods for characterizing absorbed radiation dose have included optical attenuation (density), luminescence, optically stimulated luminescence (OSL), thermoluminescence and scattering.²⁹⁻³² The following sections describe the development of a prototypical point dosimetry system that utilizes fiber-optic coupled (FOC) dosimeters to measure fundamental parameters associated with radiation dosimetry. This point detector approach provides remote, real-time dose measurements and allows direct recording of the radiation characteristics of x-ray and computed tomography (CT) imaging modalities.

System Overview

FOC dosimeters based on the sensitive elements of a coupled scintillation phosphor are characterized for their performance across the diagnostic energy range based on energy dependence, dose linearity, and angular response. This new type of dosimetry system (Figure 3-1) is based on the detection and absorption of x-rays in a scintillation phosphor material that is coupled to an optical fiber. The phosphor provides a conversion of x-ray photons to visible light, which then travels the length of the fiber to a photomultiplier tube (PMT). The PMT converts the incident light photons to an output voltage signal. The output is proportional to the number of light photons incident at the photomultiplier tube interface. This output is then relayed in terms of (photon) *counts* to a PC.

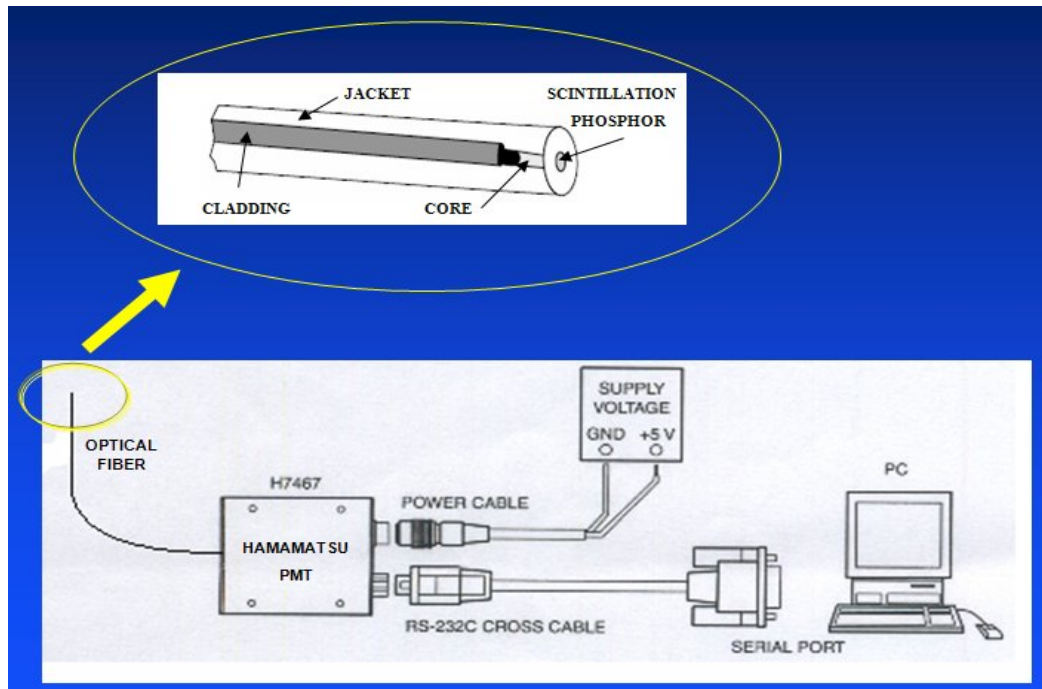


Figure 3-1. Diagram of the fiber-optic coupled dosimetry system and component (highlighted portion displays the fiber assembly)

Optical Fibers

The FOC dosimeter utilizes 400 μm diameter, pure silica core fibers³³ purchased from Ocean Optics, Inc.ⁱ Surrounding the core is a doped-fluorine silica cladding.³⁴ A diagram of the fiber assembly is provided in the zoomed in portion of Figure 3-1. A jacketing of standard black heat shrink tubing is then applied over the core and cladding to both strengthen the fiber and reduce the affect of stray light from entering or exiting the fiber assembly. The fibers are interfaced with the PMT housing by standard SMA 905 fiber optic connectors. Figure 3-2 is a digital photo of a typical dosimeter assembly used in the preceding measurements.

Scintillation Phosphor

Coupled to the end of the optical fiber is a scintillation phosphor material which provides a conversion of x-ray photons to visible light. The phosphor material absorbs (detects) incident x-

ⁱ Ocean Optics Inc., 830 Douglas Avenue, Dunedin, FL, 32698 USA.

rays. When the x-rays are absorbed in the scintillator and deposit their energy, a certain fraction of the energy is converted and visible or ultra-violet (UV) light is emitted.

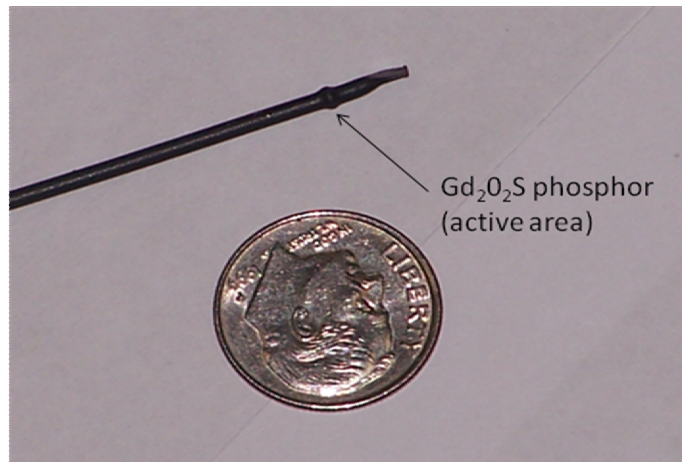


Figure 3-2. Photo of typical optical fiber dosimeter assembly

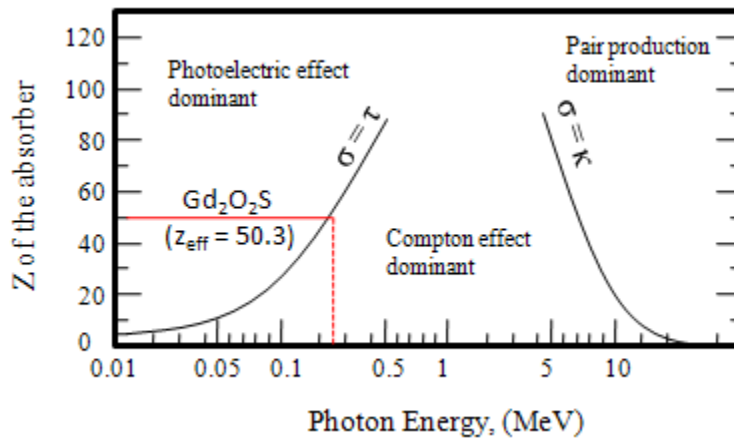


Figure 3-3. X-ray interactions probability (photon energy vs. atomic number)

Figure 3-3 shows that although the probability of photoelectric absorption decreases with increasing x-ray energy, it increases with increasing atomic number of the absorption material. The probability of photoelectric absorption per unit mass is approximately proportional to (Z^3/E^3) , where Z is the effective atomic number of the absorption material and E is the energy of the incident photon.³⁵ Thus, for high Z materials the photoelectric effect is the dominant interaction for x-rays in the diagnostic energy range (Figure 3-3). Therefore, gadolinium oxy-

sulfate ($\text{Gd}_2\text{O}_2\text{S}$) was the scintillation phosphor of choice due to its high effective atomic number ($Z_{\text{eff}} = 50.3$), its common use in diagnostic radiology film, and its excellent x-ray absorption efficiency in the diagnostic energy range (Figure 3-4).³⁶⁻³⁸

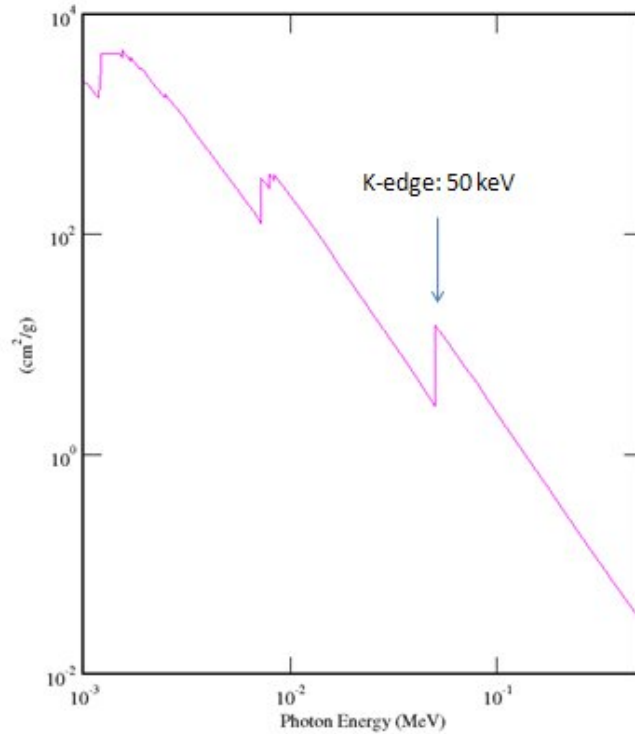


Figure 3-4 Probability of photoelectric absorption for gadolinium oxy-sulfate as a function of incident photon energy

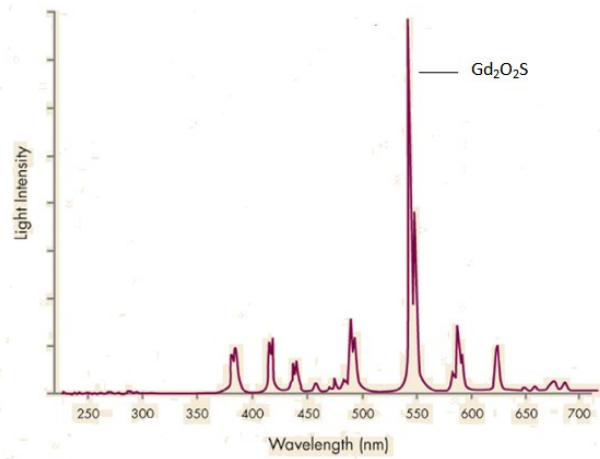


Figure 3-5. Spectral output of gadolinium oxy-sulfate light photons (peak at 550 nm) [Reprinted with permission © 2006 Carestream Health, Inc.]

Gadolinium oxy-sulfate's ability to convert a relatively small number of x-ray photons to a large number of light photons is due predominantly to x-ray absorption via the photoelectric effect in the high Z components of the phosphor dominated by gadolinium ($Z = 64$). X-ray absorption by the phosphor leads to the emission of visible light, primarily at wavelengths of 550 nm (Figure 3-5).³⁶⁻³⁷ These light photons then traverse the length of the fiber and are collected by a HAMAMATSU photon counting head.

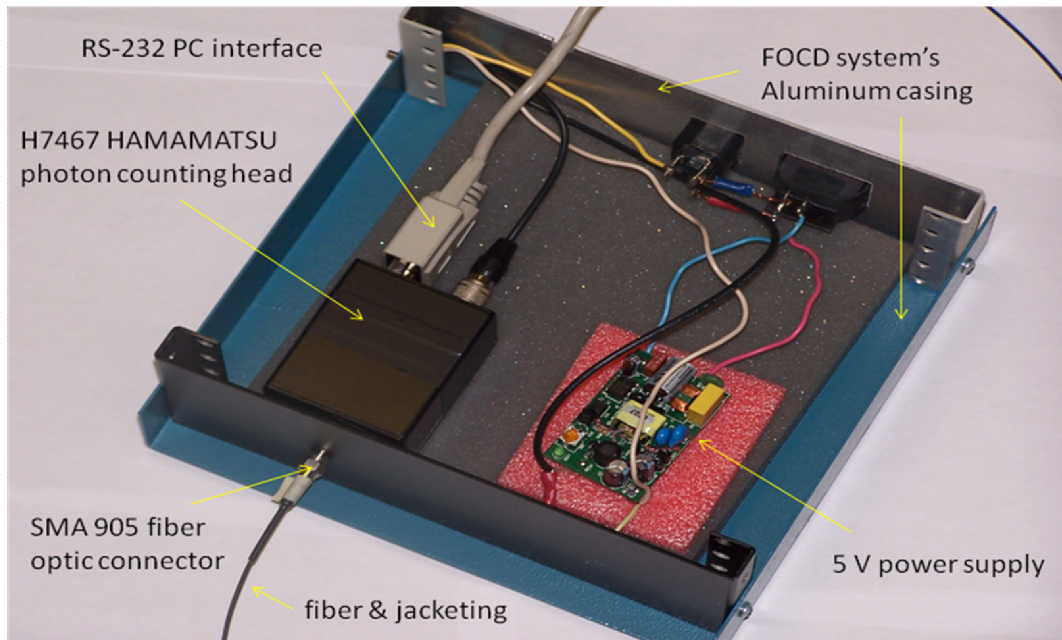


Figure 3-6. Photo of photon counting head and housing

Photon Counting Head

The H7467 series Hamamatsuⁱⁱ photon counting head contains a photomultiplier tube, high voltage power supply circuit, photon counting circuit, 20-bit counter and microprocessor all within a common metal housing.³⁹ An RS-232 interface allows data transfer and measurement integration time to be controlled through a PC and an optical fiber adapter allows connection with a fiber assembly for light input. Figure 3-6 displays the H7467 photon counting head and

ⁱⁱ Hamamatsu Photonics K. K., 325-6, Sunayama-cho, Naka-ku, Hamamatsu City, Shizuoka Pref., 430-8587, Japan.

associated components. The 5-volt power supply and photon counting head are housed in an aluminum casing for improved durability and shielding against ambient light and scatter radiation.

Photomultiplier Tube

The photomultiplier tube (PMT) allows the conversion of light photons to a corresponding electrical signal. The scintillation phosphor absorbs incident X-rays and converts them to visible light photons. These photons then traverse the length of the optical fibers as described in Chapter 2, where they enter the photomultiplier tube. Figure 3-7 is a diagram of the photomultiplier tube used in the fiber-optic coupled dosimeter.³⁹⁻⁴⁰

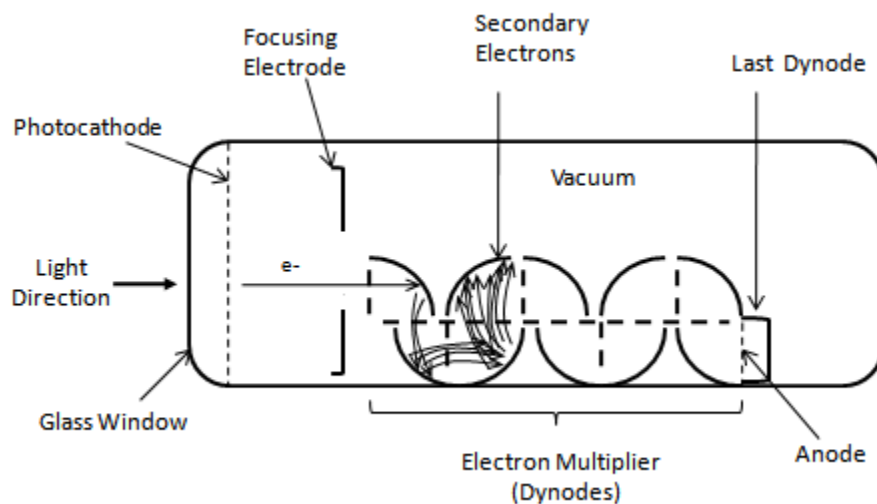


Figure 3-7. Diagram of photomultiplier tube used in the fiber-optic coupled dosimeter

Light enters the PMT through a borosilicate glass window, which allows radiation transmission from the infrared to approximately 300 nm. Deposited on the inner surface of this entrance window is a bialkali photocathode. This photosensitive area absorbs the transmitted light and emits photoelectrons into the vacuum created by the glass housing. The photoelectrons emitted by the photocathode are then focused by electrodes to the dynodes, where electron multiplication occurs. The multiplied electrons are collected by the anode where an output

signal is produced. This output signal is proportional to the amount of light incident on the photocathode. The photon counting head then relays the output (number of light photons collected) as *counts* where it is read out at a PC.

The manufacturer provided specifications for the Hamamatsu H7467 PMT shows that the bialkali photocathode has a highly sensitive spectral response in the range of 300-650 nm, i.e. the visible range of the electromagnetic spectrum (Figure 3-8).³⁹ This increased sensitivity in the visible spectrum makes Gd₂O₂S a good match for photocathode coupling due to its primary light emission at wavelengths of 550 nm (Figure 3-5).³⁶⁻³⁹

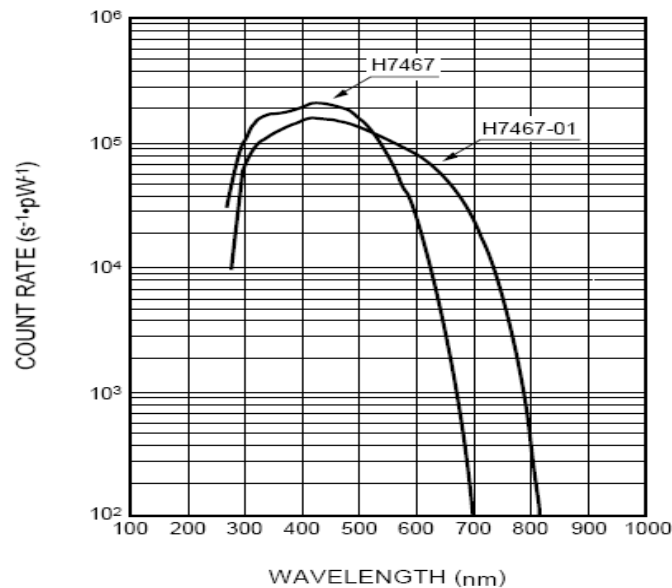


Figure 3-8. Spectral response of H7467 photon counting head and photomultiplier tube [Reprinted with permission © 1999 Hamamatsu K.K.]

Software

The fiber optic dosimeter system is run using the MS-DOS program provided by the manufacturer of the Hamamatsu H7467 Photon Counting Head, with small custom modifications. The program allows the user to choose and set an integration time for the counter and define a file path for the raw data (counts). A macro-enabled MS Excel program allows

analysis of raw data for experimental purposes. Measured counts are typically plotted versus time, and an integrated sum is provided.

System Characterization

System characterization tests across the diagnostic energy range were performed to evaluate individual fiber's energy dependence, dose linearity, and angular response. All tests were done at Shands Orthopedic Institute at the University of Florida. The clinical x-ray tube was a standard table-top x-ray unit with a half value layer (HVL) of 3.7 mm aluminum equivalent. The clinical CT unit is a Siemens Somatom Sensation 16 slice scanner.

Energy Dependence

The energy dependence of the FOC dosimeter was tested by simultaneously exposing the active area of the fiber and a 15 cc Keithley Model 96035B dual entrance window pancake ionization chamber with a Keithley Model 35050A electrometer. The tube current-time product was held constant at 100 mAs for all irradiations, while tube potential (kVp) was incremented within the range of 50 to 120 kVp. Three exposures were performed at each selected tube potential. The average of the three exposures was then calculated and plotted versus corresponding kVp values recorded from the Keithley electrometer. Variations in kVp were minimal from exposure to exposure, with standard deviations not exceeding 0.12. Figure 3-9 is a plot of the fiber optic system's energy response across the diagnostic range with vertical error bars representing plus-and-minus one standard deviation.

Dose Linearity

The dose linearity of the FOC dosimeter was tested by successively increasing the tube-current time product while maintaining a constant tube potential at 80 kVp. Again, the average of three exposures was taken for each tube current setting. FOC dosimeter response is plotted in

Figure 3-10 with error bars representing plus-and-minus one standard deviation. A linear fit shows that the fiber response is linear across the range of 20 to 200 mAs.

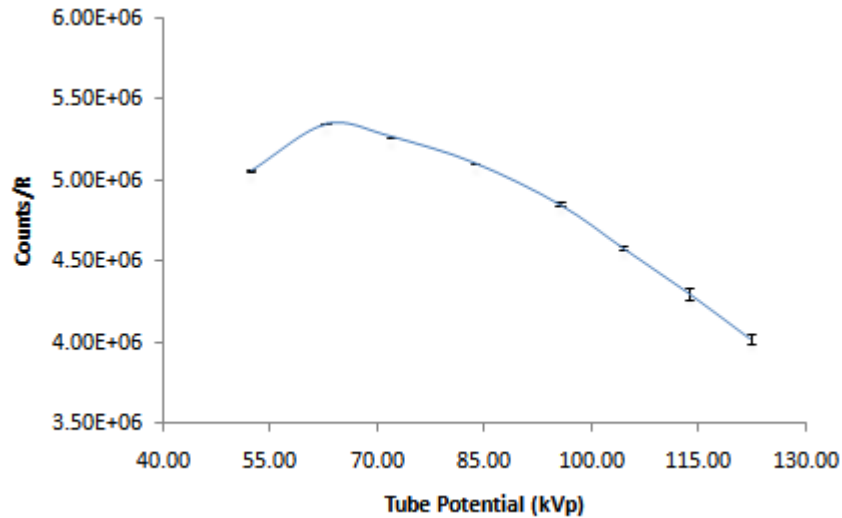


Figure 3-9. Tube potential (energy) dependence of the fiber-optic coupled dosimeter

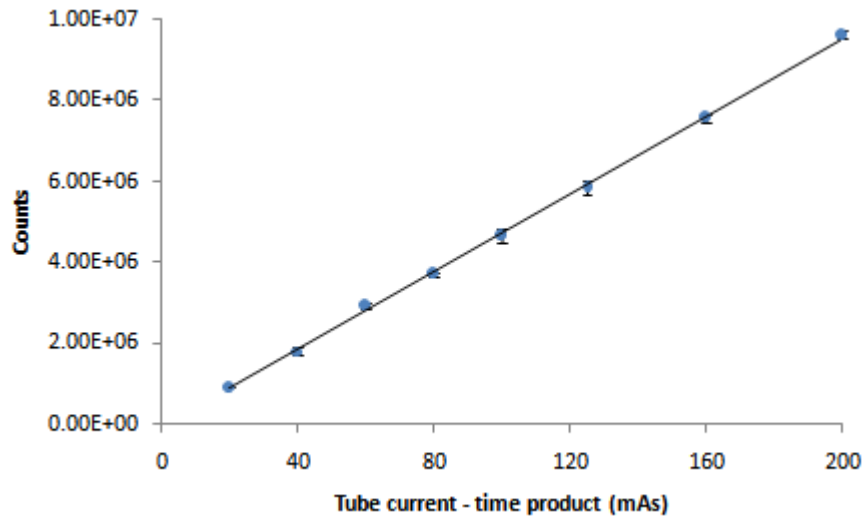


Figure 3-10. Dose linearity of the fiber-optic coupled dosimeter

Angular Dependence

Qualifying the fiber's response to the incident angle of radiation was less straightforward than the above characterization tests. The energy dependence and dose linearity evaluations were performed using a standard table-top x-ray unit. However, fiber optic dosimeter angular

dependence was assessed using the Siemens Somatom Sensation 16 slice CT scanner at all angles and involving different experimental parameters.

In order to isolate any angular dependence to the response of the fiber alone, several experimental factors had to be characterized. First the CT's beam delivery method was analyzed. A calibrated 10 cm pencil ion chamber was placed in isocenter off the edge of the CT table and exposure measurements were taken free-in-air every 10 degrees. Figure 3-11 plots the normalized exposure for the free-in-air ion chamber measurements. The data series labeled "free-in-air" shows that the intensity of the CT's x-ray delivery is constant regardless of tube angle.

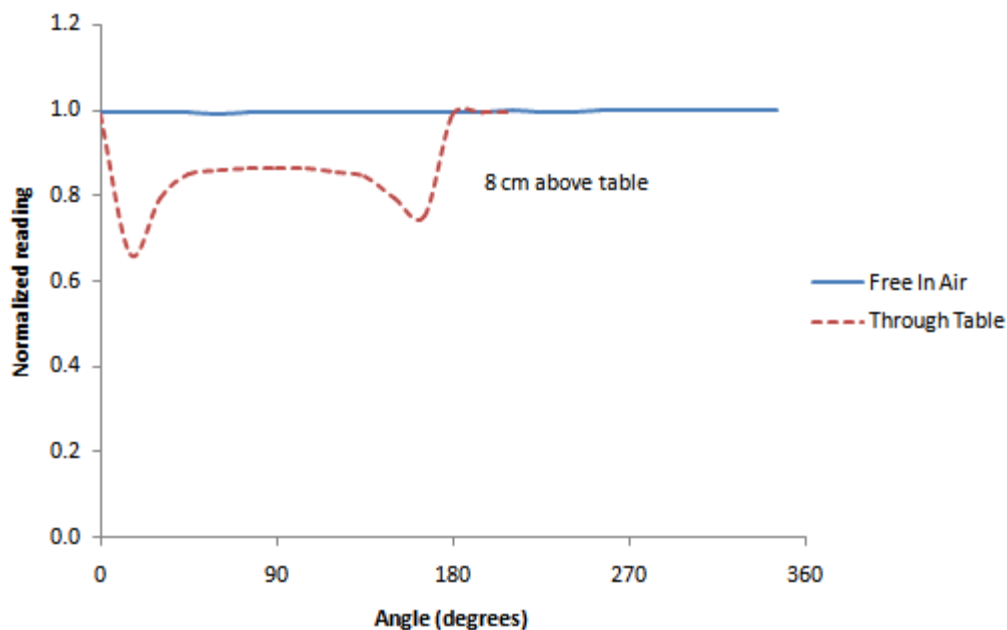


Figure 3-11. CT tube angular dependence and table attenuation. Measurements were made free-in-air with a 10 cm long pencil ion chamber placed both off and above the CT table.

Table attenuation

Figure 3-11 also shows the effect of attenuation from the CT table. A series of exposure measurements was performed and plotted for a 360° tube delivery; however, the ion chamber

was located at isocenter approximately 8 cm above the surface of the CT table (the height of the center position of a typical CTDI head phantom). The exposure measurements performed above the table were then normalized to the free-in-air results measured off the table. Figure 3-11 shows significant table attenuation of approximately 15% directly below the table and up to 33% just below the sides of the table. This increase in attenuation is due to the structure of the sides of the table. Note that in Figure 3-11, 270° corresponds to the 12 o'clock position, and thus 90° refers to when the tube position is located directly under the CT table.

Radiation incidence

The ion chamber measurements proved that the CT tube delivery is uniform about a 360° rotation and that table attenuation of the primary beam must be taken into account. Thus, further tests on the response of the fiber optic system to tube angle position would confirm an angular dependence unique to the fiber alone. As discussed in Chapter 2, incident light must fall within an acceptance angle in order to be transmitted down the length of the fiber by total internal reflection. The scintillation material coupled to the fiber's end should allow for the majority of converted light photons to fall within this acceptance window and be incident on the fiber. Therefore, the direction of the radiation incident on the cross-sectional area of the phosphor should determine the amount of light produced. In other words, the larger the area struck by incident radiation the more x-rays are absorbed. The larger the cross-section available for photoelectric absorption, the more light photons can be produced, thus strongly influencing the number of counts collected at the PMT.

In MDCT scanners, the arc of detectors and x-ray tube rotate together around the CT table. The table moves or translates along the z-axis, perpendicular to the x-y (axial) CT plane. The

fiber's angular dependence was tested free-in-air with regards to two orientations of beam incidence relative to the dosimeter: axial and perpendicular-to-axial.

In the former or head-on approach, the fiber is oriented to face the 270° tube position (12 o'clock), parallel to the axial plane. When the x-ray tube is at this orientation, radiation will be incident on the largest available area of the scintillation phosphor (i.e. parallel to the fiber). Figure 3-12 shows normalized counts versus x-ray angle of incidence. A major reduction in counts (approximately 46%) is seen when the tube is at the 90° position (i.e. directly below the table and 180° from the surface of the fiber). A less severe but still apparent degradation in counts can be seen at the 0° and 180° tube angles (perpendicular to the fiber's surface), with the maximum count intensity occurring at a head-on incidence of the fiber (i.e. the 270° tube position). Note in Figure 3-12, the initial tube position is at 0 or 360° (3 o'clock).

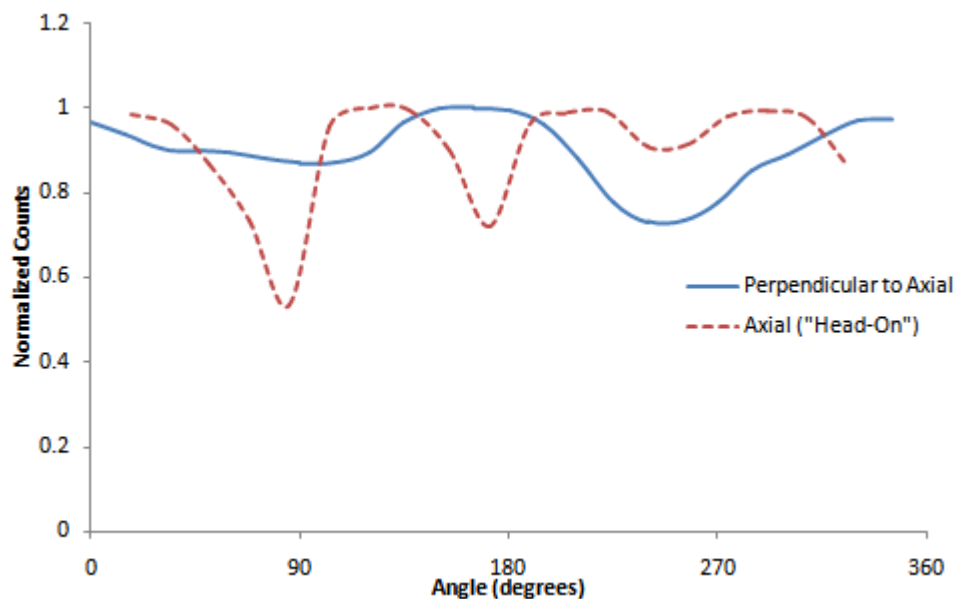


Figure 3-12. Fiber-optic coupled dosimeter's angular dependence. Measurements were made free-in-air with a FOC dosimeter oriented perpendicular and parallel to the axial (x-y) CT plane.

The remaining tests of dosimeter performance were run with the fiber positioned along the z-axis, perpendicular to the axial CT plane. As seen in Figure 3-12, the fiber has an

approximately sinusoidal response, unique when compared to the axial or “head-on” approach. In the axial orientation, the maximum count intensity occurred when the x-ray tube was positioned above the table (180-360° position) and the incident radiation was directed parallel to the fiber’s active area. The perpendicular-to-axial response in Figure 3-12, however, shows a minimal fiber response in this range. In fact, when compared with other coupled fibers that were constructed, the perpendicular-to-axial responses all show a similar sinusoidal response with minima at different phases (Figure 3-13).

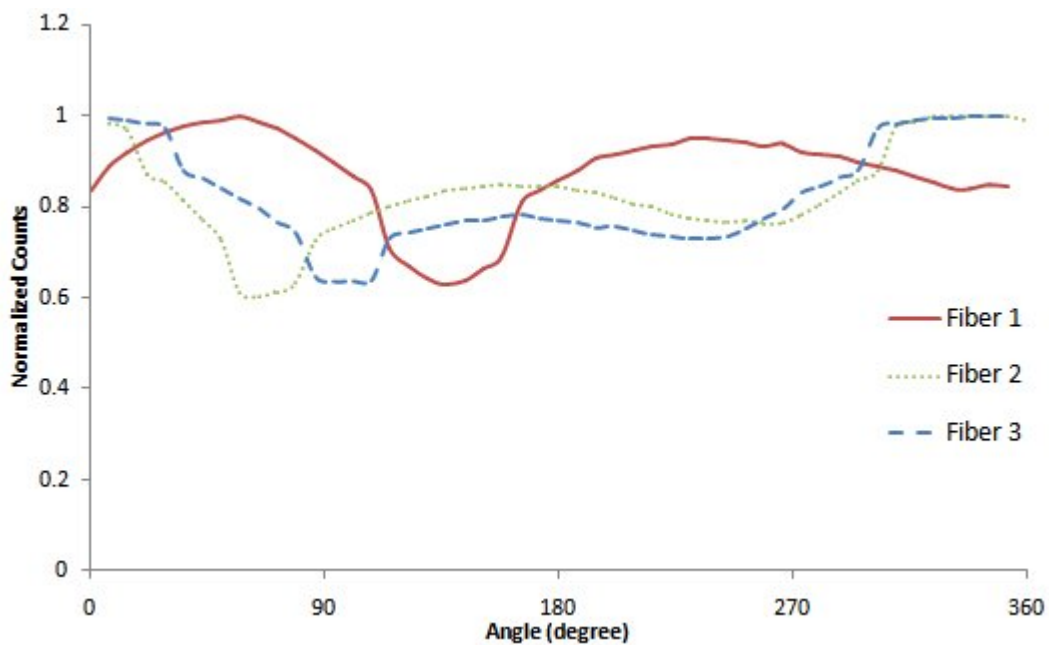


Figure 3-13. Angular dependence of several fiber optic coupled dosimeters. Measurements were made free-in-air with the dosimeters oriented perpendicular to the axial (x-y) CT plane.

This phase difference when comparing fibers is due to the coupling of the phosphor material to the silica fiber end during the construction process. The jacketing of heat-shrink tubing around the fiber core and cladding not only strengthens the fiber and protects it from stray radiation, but helps hold the coupled scintillation phosphor in place. During the jacketing

process, the coupled phosphor's orientation may be displaced. If this occurs, the dosimeter's sensitivity may change depending on the angle of incident radiation.

Angular dependence in a scattering medium

FOC dosimeters placed free-in-air show an angular dependence contingent upon the orientation of scintillation phosphor coupling to the fiber end of the dosimeter. However, dose measurements are not typically performed free-in-air, but within some type of tissue-equivalent medium. Taking this into account, the trans-axial angular dependence of the fiber was re-tested.

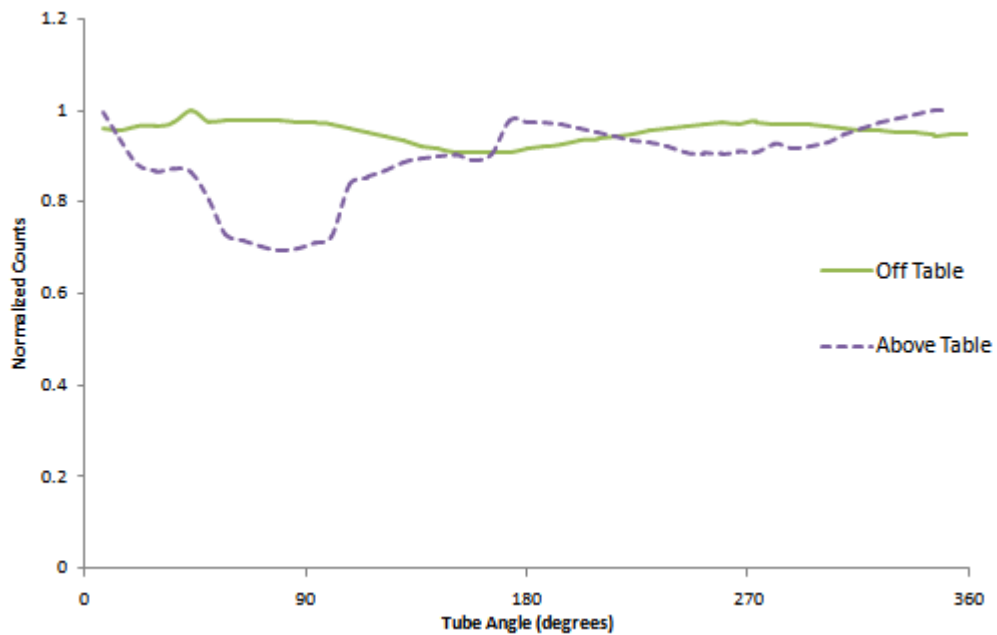


Figure 3-14. FOCD angular dependence in a scattering medium

The fiber was placed in the center of a cylinder of tissue equivalent material (radius = 2.5 cm, $\rho = 1.087 \text{ g/cm}^3$). Figure 3-14 shows the angular dependence of the fiber when placed in such a small sized scattering medium when compared to the dimensions of typical CT dosimetry phantoms. The angular variation of the fiber response is significantly reduced. When the cylinder is mounted off the table's edge, Figure 3-14 displays a full 360° characterization of fiber

angular dependence. When placed in isocenter above the table, the significance of CT table attenuation (0 – 180° on the x -axis) is again apparent (up to 30%).

Conclusions

Fiber optic dosimeters coupled with scintillation phosphor material have a strong sensitivity in the low kV energy range and show strong promise for accurate dose measurements in diagnostic radiology. Their energy dependence, specifically a sensitivity to lower energies in the diagnostic range, must be taken into account and dose measurements must be calibrated individually for the energy technique chosen. An inherent angular dependence seen in the fiber's coupled active area can be significantly reduced with perpendicular-to-axial fiber positioning and is negligible when the dose measurements are performed within a scattering medium. The fiber-optic coupled dosimeters demonstrate high sensitivity, reproducibility, excellent dose linearity, and combined with their small physical size permit accurate point-dose measurements.

CHAPTER 4 COMPUTED TOMOGRAPHY DOSE PROFILES

Introduction

Thus far, fiber-optic coupled dosimeters have been characterized for their performance across the diagnostic energy range. Their sensitivity and reproducibility suggest they may be useful in measuring fundamental parameters of radiation dosimetry, namely the direct recording of the radiation characteristics associated with diagnostic imaging modalities. The real-time response of these dosimeters further suggests their value in characterizing the dose delivery methods of multi-detector computed tomography, where ion chamber collected charge measurements fail and the use of thermo-luminescent dosimeters can be extremely time consuming. Therefore, comprehensive analyses and measurements of computed tomography dose profiles have been performed using a fiber-optic coupled dosimetry system to characterize the various operating conditions of a computed tomography scanner.

Materials and Methods

Helical CT scans were performed using a Siemens Somatom Sensation 16-slice scanner. Dose measurements were recorded using FOC dosimeters and polymethylmethacrylate (PMMA) CT dosimetry phantoms. Table 4-1 lists the combination of computed tomography operating conditions utilized, along with the types of CTDI phantoms chosen and the positions used within each phantom. For each measured dose profile, the active area of the dosimeter was placed within the center of either the head or body phantom's CTDI position and the counts were measured versus time. The helical scan dose profiles were then plotted as counts versus position within the phantom (i.e. distance along the z -axis).

Table 4-1. Helical scan dose profiles – Operating conditions. Scans were performed using the five positions for two CTDI phantoms, at three pitches and two slice thicknesses.

phantom	kVp	effective mAs	position	pitch	slice thickness ^a
Head	120	82	Top	0.5	12 mm ^b
Body	120	133	Bottom	1	24 mm ^c
			Center	1.5	
			Left		
			Right		

^aSlice thickness, $T = n \times \Delta T$, where $n = \#$ channels, and $\Delta T =$ beam width

^bAcquired using $T = 16 \times 0.75$ mm

^cAcquired using $T = 16 \times 1.5$ mm

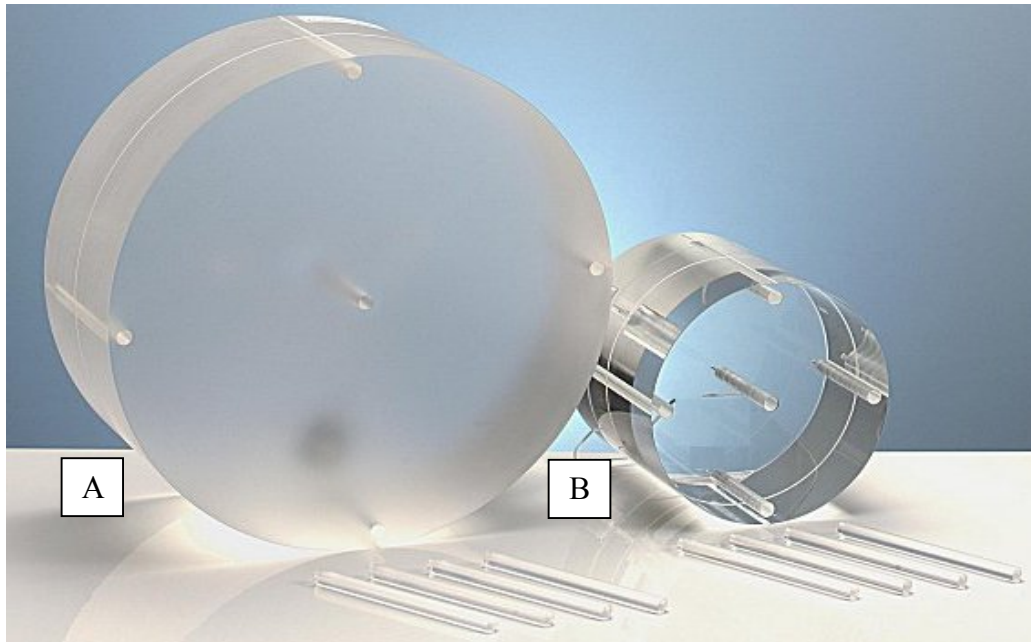


Figure 4-1. Photograph of the standard PMMA CTDI phantoms. A) Body. B) Head.

Head & Body Phantoms

Measurements were performed using two standard PMMA CTDI phantoms: the head and the body phantoms. Both phantoms are 15 cm in length. The head phantom is 16 cm in diameter and the larger body phantom has a diameter of 32 cm. In each of the CTDI phantoms there are five drilled holes (1 cm in diameter) parallel to the z -axis (couch direction) to allow the placement of dosimeters for the measurement of the central and peripheral CTDI. Holes that are not being used are filled with corresponding PMMA plugs. Figure 4-1 shows the two phantoms and the five drilled holes/positions (center, top, left, right, and bottom).

Tube Potential (kVp) & Tube Current-Time Product (mAs)

Dose profiles were measured using five different positions within both the head and body phantoms for a permutation of three pitches and two slice thicknesses (i.e. a total of 30 head phantom scans and 30 body scans). All scans were performed at a tube potential of 120 kVp. The tube current-time product (mAs) was 82 and 133 *effective* mAs for the series of head and body phantom scans, respectively (Table 4-1).

Tube current and exposure time per rotation govern the number of x-ray photons utilized, given by the tube current-time product ($\text{mA} \cdot \text{s}$), or simply mAs (milliamperes-second). Tube current-time product is indicative of the relative output (radiation exposure) of the x-ray tube of a given CT scanner, at a given kVp. It does not indicate the absolute output (dose), as the exposure per mAs varies significantly between CT scanner manufacturers, models, and tube potential settings.¹

Siemens reports the average mAs along the z -axis, called the effective mAs, defined as the true mAs divided by the pitch. In MDCT, noise is dependent on pitch, thus as pitch is increased, scanner software may automatically increase the mA such that image noise (and possibly the

patient dose) remains relatively constant with changing pitch values.^{5,41} Thus, the user may be unaware that the actual mA was increased.

Pitch

For the Siemens Somatom Sensation 16-slice scanner, pitch is defined as the table increment per rotation of the gantry divided by the detector acquisition width.⁴² It is an important aspect of the scan protocol, influencing the dose to the patient, scan time, and image quality. Measurements in this study were performed using three different selections of pitch: 0.5, 1.0, and 1.5.

A pitch of 1.0 is physically similar to performing a conventional axial scan with contiguous slices.¹² Scanning with a pitch of less than 1.0 results in overscanning, or an overlapping of single scan dose profiles. Its advantage is an improvement in image quality, but it comes at the cost of higher dose to the patient. On the other hand, increasing the pitch beyond 1.0, leads to a partial scanning of the patient and a potential reduction in image quality. The advantage of increasing pitch for a given CT protocol is both a reduction in scan time as well as a reduction of dose to the patient if all other parameters are held constant.

Slice Thickness

The slice thickness T for multi-detector CT scanners is determined by the number of channels N acquired along the z -axis and the width of the detector ΔT .

$$T = n \times \Delta T \quad (4-1)$$

For example, the 12 mm slice thickness (nominal beam width) used in measuring the helical dose profiles below is acquired using $T = 16 \times 0.75$ mm. The detector configuration not only determines the desired slice thickness, but also affects the retrospective reconstruction options (thinner or thicker images) and the radiation efficiency of the system (i.e. patient dose).¹

Measurements in this study were performed at two different nominal slice thicknesses: (1) 12 mm (acquired at $T = 16 \times 0.75$ mm) and (2) 24 mm (acquired at $T = 16 \times 1.5$ mm). The wide beam collimation allows for much faster z -coverage (i.e. faster scan times). The narrower collimation allows for retrospective reconstruction of narrower slices. Thinner slices have the benefit of improved spatial resolution with a trade-off of increased dose to the patient.

Helical scan dose profiles were performed using various slice thicknesses and pitches for both the head and body phantoms at the centers and peripheries of each phantom. The active area (phosphor) of the fiber-optic coupled dosimeter was placed in the center of the selected phantom position and scans were performed for the various clinical protocols listed in Table 4-1. The fiber response (counts) was measured in real time and plotted as counts versus phantom position. The characteristics of the dose profiles were then analyzed in terms of changes in CTDI phantom position, pitch, and slice thickness.

Results and Discussion

Head Phantom

Figure 4-2 shows a comparison of measured helical scan dose profiles performed in the five positions of the CTDI head phantom. Each profile shown was performed at 120 kVp and 82 effective mAs for a pitch of 0.5 and a slice thickness of 12 mm. The accuracy of the dosimeters real-time acquisition response was verified by comparing the photon counting head's time readout versus the total scan time displayed on the Siemens CT console. Figure 4-2 displays the intensity response of the fiber plotted versus position in the PMMA phantom. Fiber response (counts) is normalized to the maximum dose $D(0)$ which occurs at the center of the scan length.

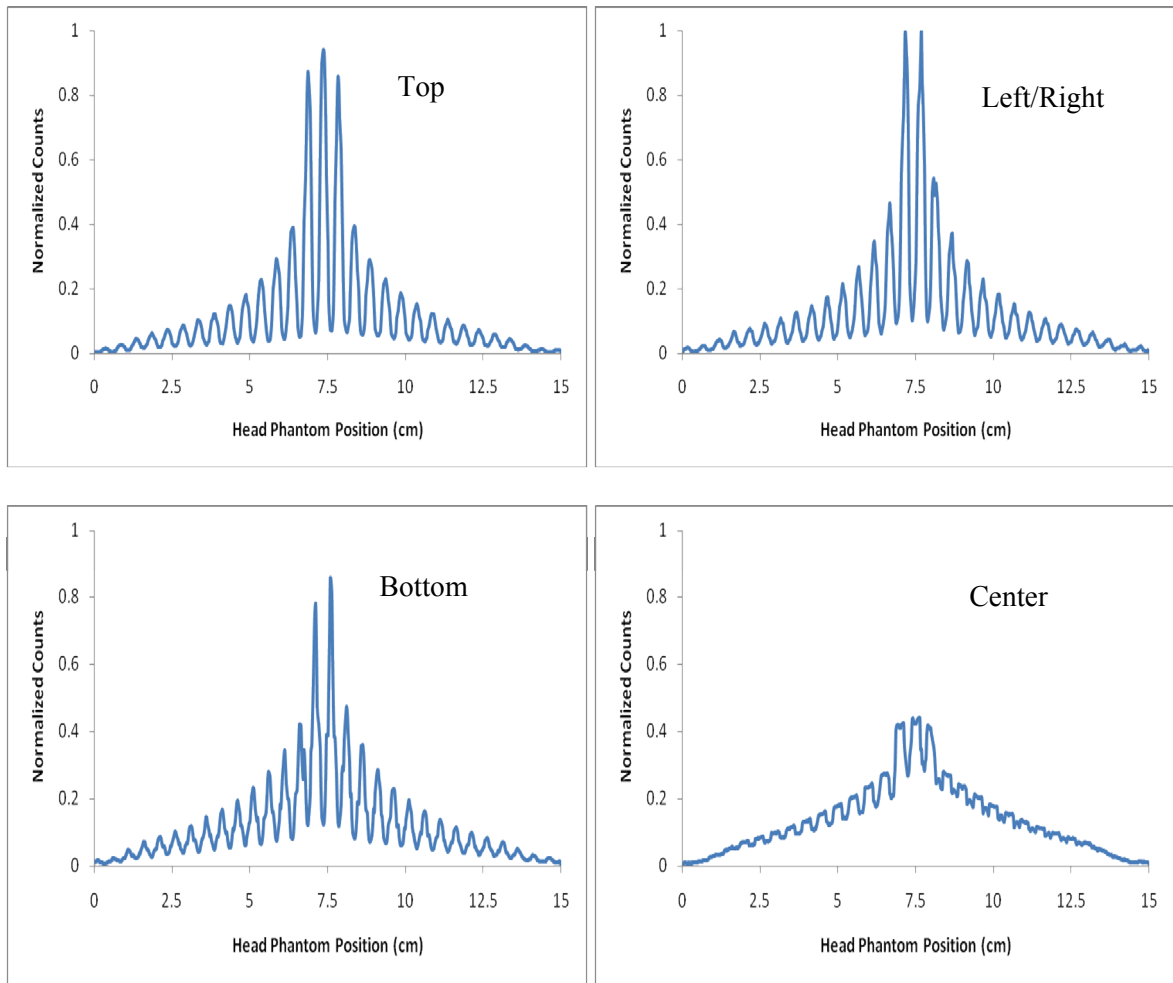


Figure 4-2. Comparison of measured data in the five positions of the CTDI head phantom. Center and four peripheral (left and right responses are identical) measurement locations indicated. Profiles were measured from CT scans performed at 120 kVp and 82 effective mAs for selected pitch of 0.5 and a slice thickness of 12 mm.

The first characteristic one notices is the oscillating nature of the helical dose profiles.

Figure 4-3 provides an expanded view of the dose profile seen in the top left of Figure 4-2 (note the abscissa change to units of CT scan time). The tube rotation time of 0.5 seconds can be seen from the measured distance between adjacent peaks in the dose profile. Also shown are the attenuation effects of the CTDI phantom material as the tube rotates around the phantom-dosimeter setup. In Figure 4-3, the FOC dosimeter is placed in the center of the top position of the CTDI phantom. Peaks in the dose profile correspond to an x-ray tube position of 12 o'clock

(i.e. shortest possible source-to-detector distance, minimal x-ray attenuation). Minima in the profile are due to the location of the tube at 6 o'clock (the longest source-to-detector distance). The combined effects of the CT table and 16 cm diameter head phantom result in an attenuation of 99.3% of the dose when the x-ray tube is at a maximum distance from the dosimeter.

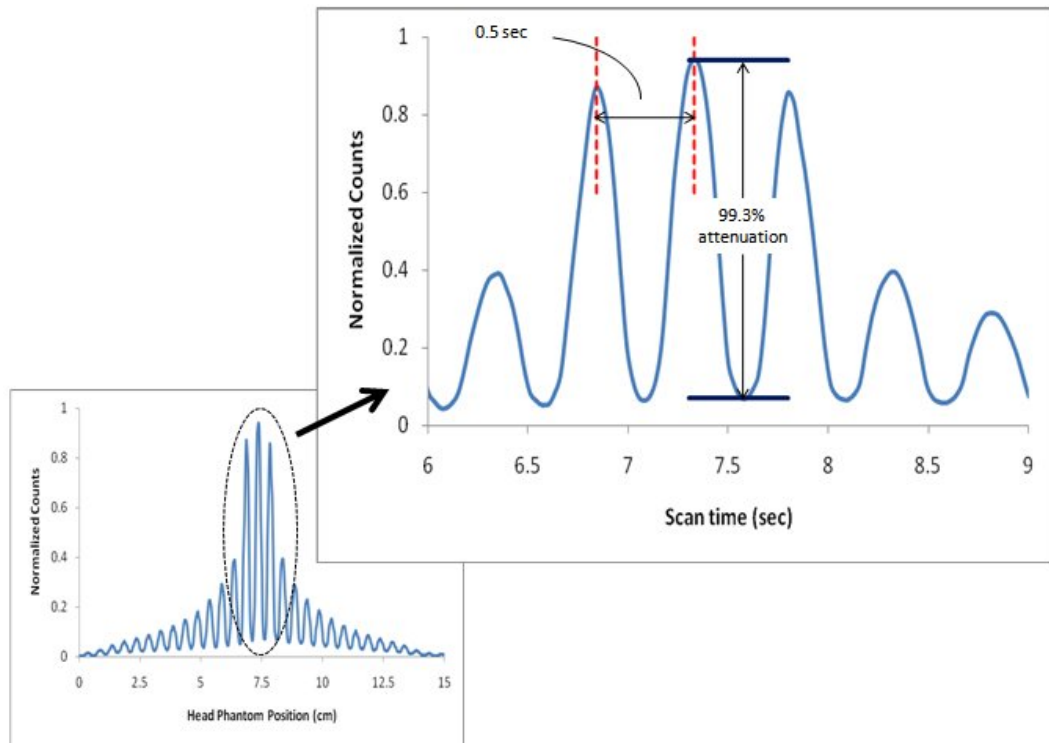


Figure 4-3. Expanded view of the helical dose profile measured in the 12 o'clock (top) position of the CTDI head phantom. The CT scan was performed at 120 kVp and 82 effective mAs for selected pitch of 0.5 and a slice thickness of 12 mm.

The attenuation effects of both the PMMA phantom material and the CT table are also visible in the other dose profiles of Figure 4-2. The head phantom's bottom position dose profile has a lower intensity (85%) at the center of the scan length when normalized to the other peripheral dose profiles (top, left, and right) due to the increased x-ray attenuation from the CT table. The peaks in the bottom position profile occur when the x-ray tube is at 6 o'clock. Here the source-to-detector distance is minimized, but reduced intensity in the center dose is caused by the attenuation of the table. Correspondingly, the attenuation effects at the maximum source-

to-detector distance for the bottom phantom position are not as significant. When the tube is located at 12 o'clock, the phantom material alone contributes to the attenuation of the dose measured by the dosimeter. Without the addition of the CT table, 86.3% of the central dose is attenuated when the x-ray tube is at a maximum distance from the dosimeter.

When the dosimeter is placed in the center position of the head phantom for the measuring of helical dose profiles, the attenuation effects of the PMMA phantom are constant during the rotation of the x-ray tube. As a result, there is a lowering of the dose distribution at the central slice of the center position profile (bottom right of Figure 4-2). Figure 4-4 is an expanded view of this profile with the abscissa changed to reflect the helical scan time. The tube rotation time of 0.5 seconds can be seen in the measured distance between consecutive minima in the dose profile, which correspond to an x-ray tube position of 6 o'clock.

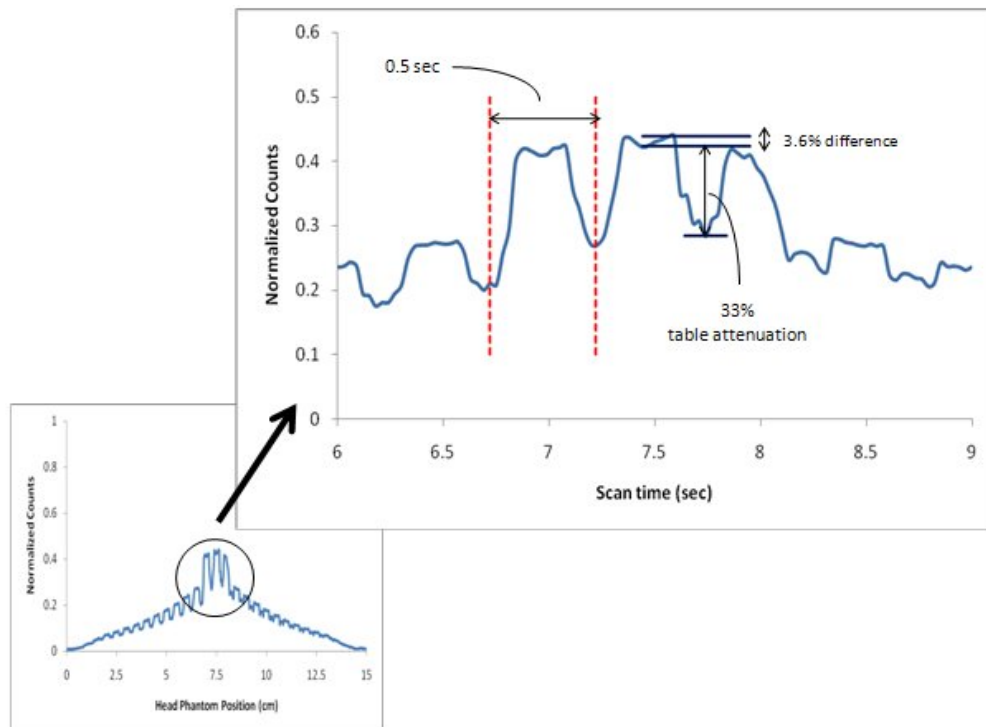


Figure 4-4. Expanded view of the helical dose profile measured in the center position of the CTDI head phantom. The CT scan was performed at 120 kVp and 82 effective mAs for selected pitch of 0.5 and a slice thickness of 12 mm.

A close look at the peak dose at the center of the scan length shows a flattening of the peak dose when the tube is above the table. This flattening of the peak is due to the symmetry of x-ray attenuation from the cylindrical phantom. Also seen in the zoomed view of Figure 4-4 is a small dip in the central dose peak measured to be 0.25 seconds from adjacent minima, thus corresponding to a tube position of 12 o'clock. The difference in intensity between peak and valley, therefore, is due solely to the CT table which attenuates 33% of the dose at isocenter. Figure 4-4 illustrates the significance of table attenuation in the dose profile not seen in other models that take into account only phantom attenuation in the axial plane.

Body Phantom

Measured helical scan dose profiles were also performed for the five positions of the CTDI *body* phantom for three pitches and two slice thicknesses. Figure 4-5 displays the normalized intensity response of the fiber plotted versus position in the 32 cm diameter PMMA body phantom. The profiles were measured from CT scans performed at 120 kVp and 133 effective mAs for a 12 mm slice thickness and pitch of 0.5.

The most obvious characteristic of the body phantom dose profiles is the attenuation effects of the larger diameter phantom (compared to the smaller 16 cm diameter head phantom). Note the intensity difference between the peaks and valleys for each peripheral dose profile. The 32 cm diameter body phantom attenuates nearly 100% of incident x-rays when the tube is directed from the opposite side of the dosimeter (maximum source-to-detector distance).

Thus, x-ray attenuation in the body phantom is dominated by the large diameter phantom and not the CT table. The *head* phantom's bottom position dose profile has a lower intensity (86%) at the center of the scan length when normalized to the other peripheral dose profiles (top, left, and right) due to the increased x-ray attenuation from the CT table. The effect of table attenuation on the central peak of the *body* phantom's bottom position profile is not as significant

as in the head phantom, though the intensity of the dose at the center of the scan length is still lower when compared to the other peripheries (91%).

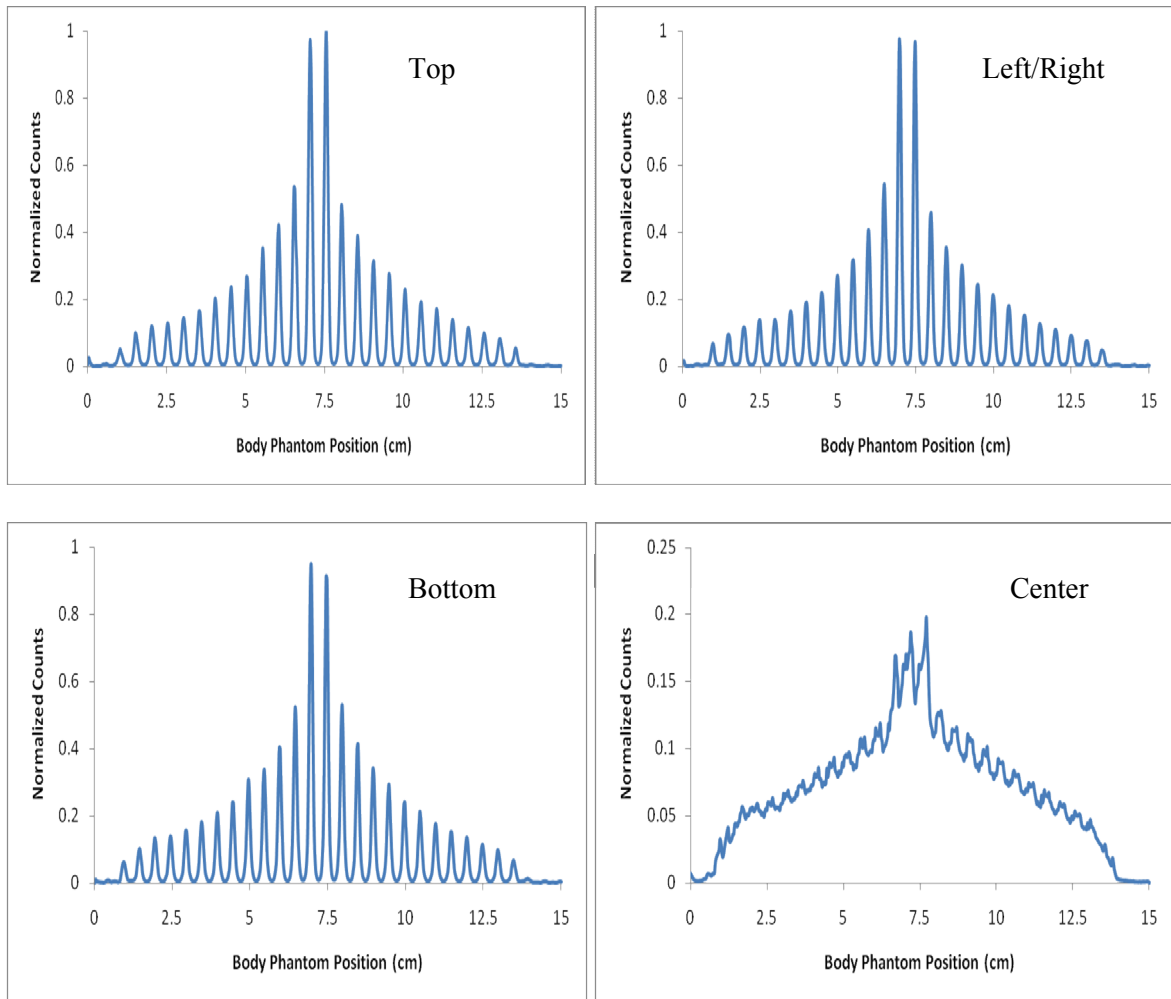


Figure 4-5. Comparison of measured data in the five modules of the CTDI body phantom: center and four peripheries. Profiles were measured from CT scans performed at 120 kVp and 133 effective mAs for a pitch of 0.5 and 12 mm slice thickness.

The lowering of the central peak dose in the center position of the body phantom dose profile is also enhanced due to the increased x-ray attenuation of the larger diameter body phantom. The broadening of the scatter tails in the center position dose profile can be seen in the lower right graph of Figure 4-5, and is also due to the larger diameter body phantom, as the scatter-to-primary ratio increases with increasing phantom diameter thickness. The broad scatter tails for the body phantom's center position fall off sharply to zero at the end of the phantom

length, indicating that standard PPMA phantom lengths (150 mm) are too short to sufficiently measure the scatter radiation associated with helical computed tomography.

Pitch

Head phantom

Helical CT scans were also analyzed to illustrate the effect of pitch selection on the measured dose profile. Again, the active area of the dosimeter was placed in the center of the selected CTDI phantom position and helical scans were produced. Dose profiles in Figure 4-6 were measured at 120 kVp, 82 effective mAs, and a slice thickness of 24 mm in the top and center positions of a CTDI *head* phantom. The pitch associated with each scan is indicated within the figure along with the phantom position and scan time.

Figure 4-6 shows the change in the dose profile as pitch is increased and slice thickness is held the same. The reduction of scan time was indicated on the CT console and confirmed by the dosimetry system. The integrated counts (dose) were also reduced as pitch increases for the five positions of the head phantom (Table 4-2). Compared to the measured data for a pitch of 1.0, the total counts (integrated across the entire scan length) for all head phantom position dose profiles show a 15 and 20% *increase* in dose for the 12 and 24 mm slice acquisition, respectively, when the pitch was reduced to 0.5. Likewise, an increase in pitch from 1.0 to 1.5, leads to an average dose *reduction* of 9 and 13% for the two slice thicknesses in the five CTDI position dose profiles. The weighted average given in Table 4-2 takes into account the fact that dose distribution varies in the axial (*x-y*) plane given by $CTDI_w$ (Eq. 1-2).

$$CTDI_{(w)} = \frac{1}{3}CTDI_{(c)} + \frac{2}{3}CTDI_{(p)} \quad (4-1)$$

where $CTDI_{(p)}$ is the average of the four peripheries.

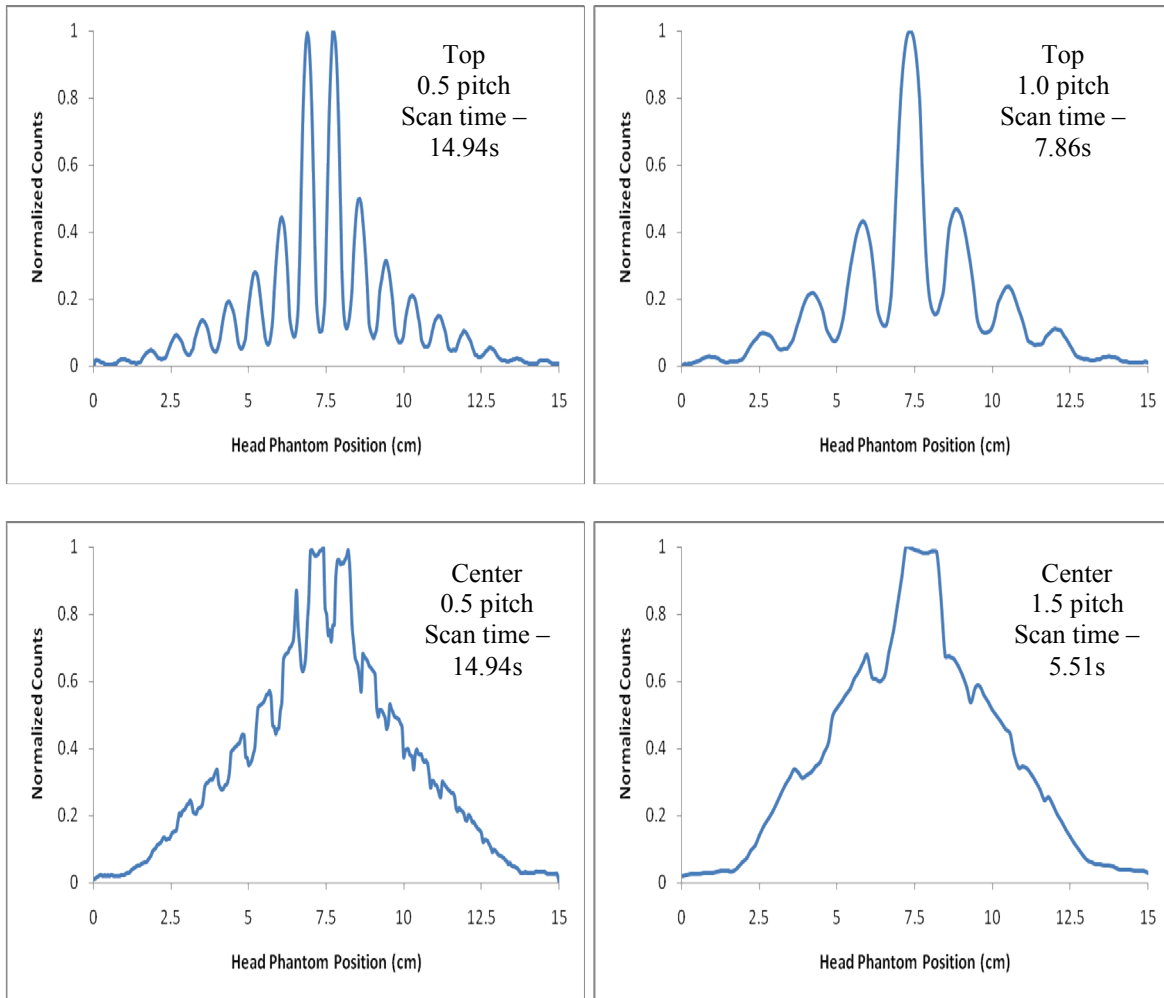


Figure 4-6. Effect of pitch on measured helical dose profiles in the CTDI head phantom. Profiles were measured from CT scans performed at 120 kVp, 82 effective mAs, and 12 mm slice thickness. Phantom position, pitch, and scan time are indicated.

The *effective* mAs in Siemens MDCT, defined as the true mAs divided by the pitch, is used so that scanner software will automatically increase the mA such that image noise (and possibly the patient dose) remains relatively constant with changing pitch values. However, dose is still seen to increase with decreases in pitch, and vice versa (Tables 4-2 and 4-3). An evaluation of the efficiency of the CTDI metric (Chapter 5) shows that the primary (central peak dose) dose delivered to a cylindrical PMMA phantom (regardless of position) does not change significantly when pitch is changed. Therefore, the difference in dose ratios is due primarily to

scatter radiation outside the center slice. When pitch is reduced, overscanning of the phantom allows for the measurement of the scatter tails at the edges of the phantom length.

Table 4-2. Head phantom - Ratios of integrated counts (dose) show the effect of pitch on the helical scan dose profile. FOC dosimeters measured the integrated counts from helical dose profiles acquired at 120 kVp and 82 effective mAs in five positions of a CTDI head phantom for two slice thicknesses and three pitches (0.5, 1.0, 1.5).

slice thickness	12 mm		24 mm	
	Pitch Ratio			
module	0.5 / 1.0	1.5 / 1.0	0.5 / 1.0	1.5 / 1.0
top	1.17	NA	1.22	0.87
left	1.16	0.89	1.23	0.87
right	1.15	0.91	1.20	0.86
bottom	1.13	0.92	1.17	0.87
center	1.13	0.91	1.18	0.89
average _(w)	1.14	0.91	1.20	0.88

Body phantom

Figure 4-7 shows the change in the body phantom helical scan dose profiles as pitch is increased. The scan time is indicated next to each dose profile and shows a reduction in total scan time as pitch is increased. The selected pitch, phantom position, and slice thickness are also shown within the figure.

Table 4-3 lists the ratio of integrated counts (dose) as pitch is changed and slice thickness is held the same for all five positions of the CTDI body phantom. The periphery ratios are similar to calculated head phantom data, with the exception of the body phantom's center position. Nevertheless, the weighted average remains close to that calculated in the head phantom due to the heavy weighting given to the peripheral points in the axial slice plane, where primary-to-scatter ratios are higher than in the center position.

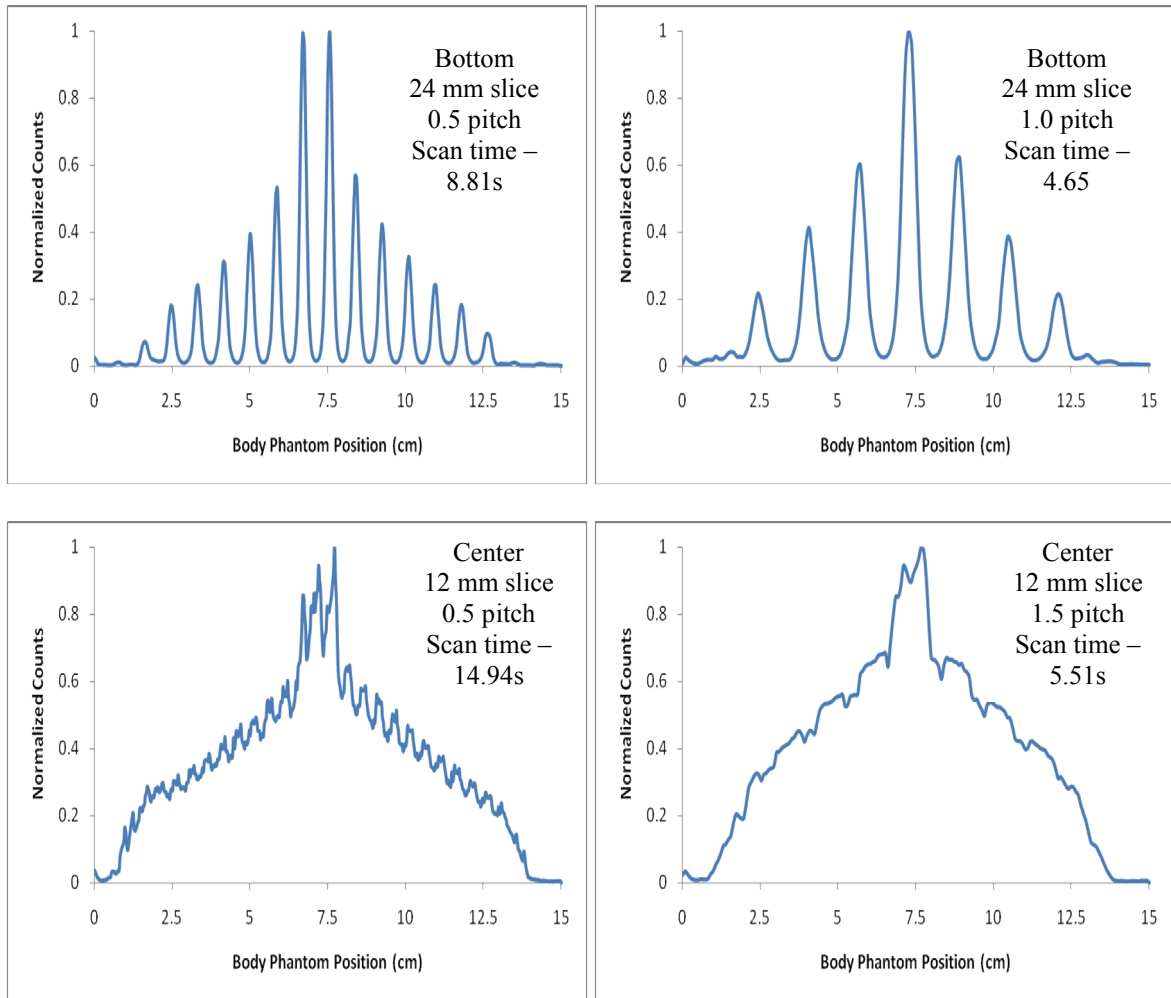


Figure 4-7. Effect of pitch on measured helical dose profiles in the CTDI body phantom. Profiles were measured from CT scans performed at 120 kVp and 133 effective mAs. Phantom position, pitch, slice thickness, and scan time are indicated.

The total counts integrated across the entire scan length (i.e. dose) are reduced as pitch is increased for the four peripheries, yet the dose in the center position of the body phantom shows little change as pitch is increased or decreased (Table 4-3). This is due to the increased scatter-to-primary ratio of incident radiation at the center position of the larger diameter phantom and the finite size of the phantom length.

The lowering of the central peak dose in the center position of the body phantom profile is due to the increased x-ray attenuation of the larger diameter body phantom. The broadening of the scatter tails in the center position dose (bottom graphs of Figure 4-7) is also due to the larger

diameter body phantom, as the scatter-to-primary ratio increases with increasing phantom diameter thickness. As pitch is changed, the primary (central peak dose) dose delivered to the body phantom does not change significantly. Therefore, the difference in dose with change in pitch is due primarily to scatter radiation outside the center slice. The broad scatter tails for the body phantom's center position fall off sharply to zero (regardless of pitch selection, Figure 4-7) at the end of the phantom length, indicating that standard PPMA phantom lengths (150 mm) are too short to sufficiently measure the scatter radiation associated with helical CT.

Table 4-3. Body phantom - Ratios of integrated counts (dose) show the effect of pitch on the helical scan dose profile. FOC dosimeters measured the integrated counts from helical dose profiles acquired at 120 kVp and 133 effective mAs in five positions of a CTDI body phantom for two slice thicknesses and three pitches.

slice thickness	12 mm		24 mm	
	Pitch Ratio			
module	0.5 / 1.0	1.5 / 1.0	0.5 / 1.0	1.5 / 1.0
top	1.18	0.88	1.28	0.86
left	1.17	0.90	1.22	0.88
right	1.16	0.92	1.26	0.87
bottom	1.15	0.91	1.17	0.87
center	1.03	0.97	1.10	0.94
average _(w)	1.12	0.92	1.19	0.89

Slice Thickness

Head phantom

Figure 4-8 shows the change in helical dose profiles as the detector configuration (slice thickness) is changed and pitch is kept the same. As expected, the scan time is greatly decreased when a wider detector configuration is chosen and all other parameters remain unchanged. The dose integrated across the scan length is reduced as well. Table 4-4 displays the ratio of

integrated counts measured with fiber-optic coupled dosimeters as the slice thickness is reduced from 24 to 12 mm.

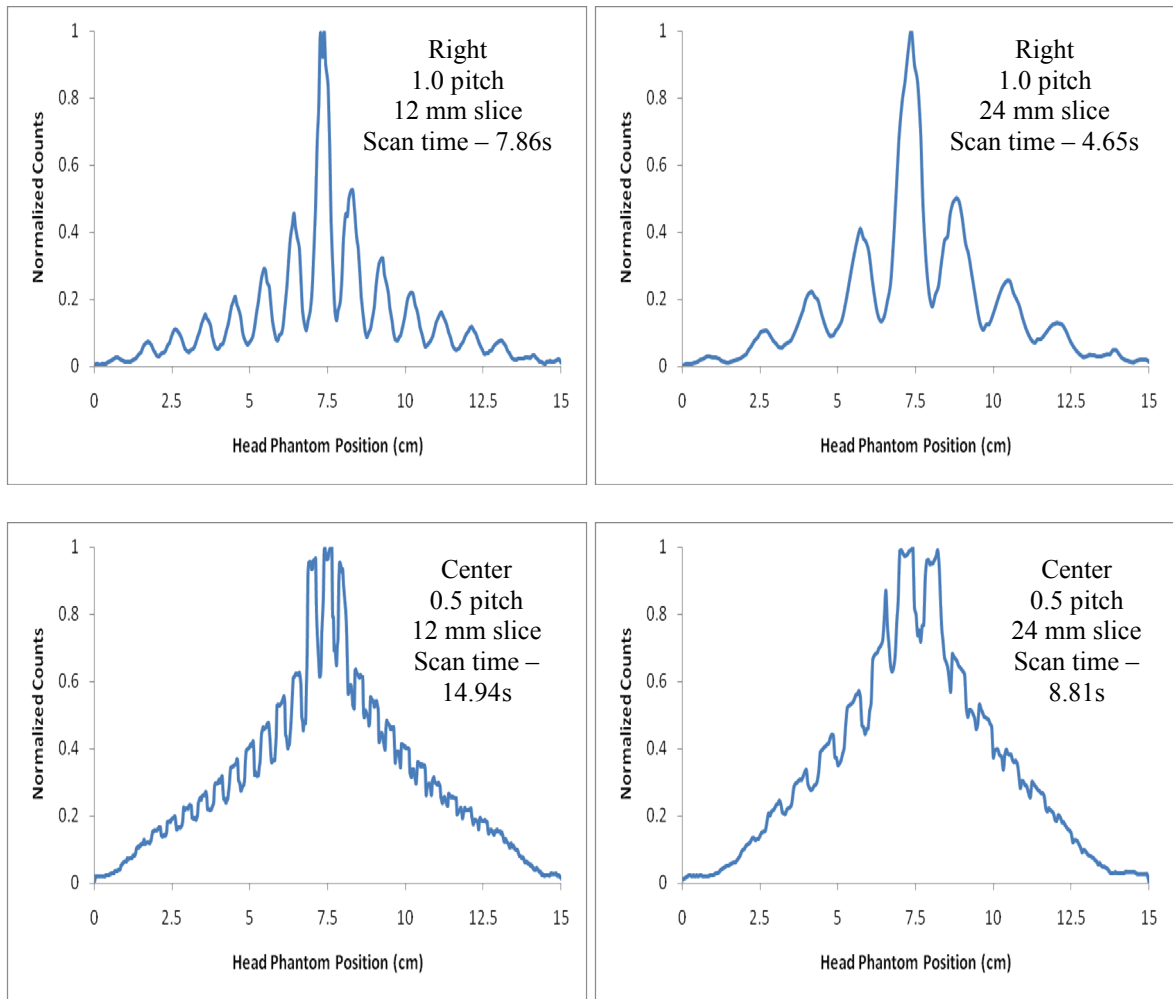


Figure 4-8. Effect of slice thickness on measured helical dose profiles in the CTDI head phantom. Scans were performed at 120 kVp and 82 effective mAs. Phantom position, pitch, slice thickness, and scan time are indicated

Integrated counts were measured from helical dose profiles acquired at 120 kVp and 82 effective mAs in a CTDI head phantom for two slice thicknesses. The integrated count ratio of narrow versus wide slice thickness was then calculated for the five CTDI positions and three pitches.

As stated earlier, narrower collimation allows for retrospective reconstruction of narrower slices, which have the benefit of improved spatial resolution with a trade-off of increased dose to

the patient. The dose profiles for each phantom position show this increase in dose as the slice thickness is narrowed. At a pitch of 0.5, the measured counts increase by an average of 20% as slice thickness is reduced from 24 to 12mm. The increase in counts average 25% for a pitch of 1.0 and was 30% for a pitch of 1.5.

Table 4-4. Head Phantom - Ratios of integrated counts (dose) show the effect of slice thickness on the helical scan dose profile. FOC dosimeters measured the integrated counts from helical dose profiles acquired at 120 kVp and 82 effective mAs in the five positions of a CTDI head phantom for two slice thicknesses and three pitches.

module	12 mm slice / 24 mm slice		
	pitch		
	0.5	1	1.5
top	1.22	1.27	NA
left	1.18	1.25	1.27
right	1.20	1.25	1.32
bottom	1.19	1.24	1.31
center	1.19	1.25	1.28
average _(w)	1.20	1.25	1.30

Body phantom

Figure 4-9 shows the change in helical dose profiles as the slice thickness is changed. Again, the scan time and integrated counts are decreased when a wider detector configuration is chosen and all other parameters remain unchanged. Integrated counts were measured from helical dose profiles acquired at 120 kVp and 133 effective mAs in the CTDI body phantom. The ratio of integrated counts (dose) of narrow versus wide detector configurations was then calculated for the five CTDI modules at three pitches.

Table 4-5 shows the ratio of integrated dose as the nominal slice thickness is changed from 12 to 24 mm. As expected, the top, left, and right phantom position dose ratios for the body phantom show a steady increase in dose of 27, 36, and 40%, for pitches of 0.5, 1.0, and 1.5,

respectively, when slice thickness is reduced from 24 to 12 mm. A closer look at Tables 4-4 and 4-5 shows that body phantom ratios (at the top, left, and right) are slightly higher than corresponding dose ratios in the head phantom.

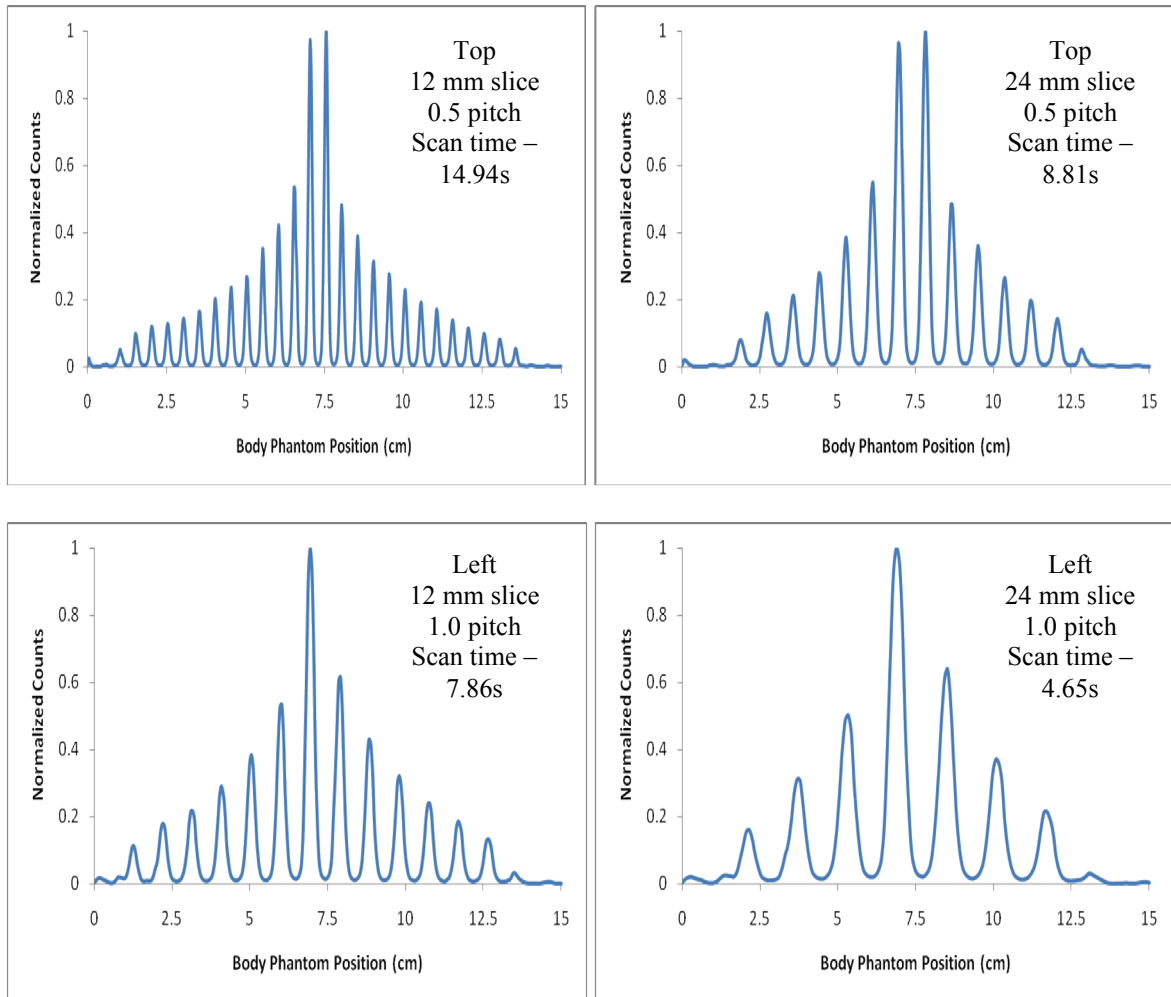


Figure 4-9. Effect of slice thickness on measured helical dose profiles in the CTDI body phantom. Scans were performed at 120 kVp and 133 effective mAs. Phantom position, pitch, slice thickness, and scan time are indicated.

This is due to primarily to the detector's proximity to the radiation source and the added attenuation of the larger diameter phantom. For peripheral phantom positions (excluding the bottom), the larger diameter body phantom places the dosimeter 8 cm closer to the x-ray tube when the source-to-detector distance is minimized. As seen in Figure 4-5, the 32 cm diameter body phantom attenuates nearly 100% of incident x-rays when the tube is directed from the

opposite side of the dosimeter (maximum source-to-detector distance). Therefore, dose ratios in the body phantom with regard to change in slice thickness are predominately dependent on the primary radiation when the source-to-detector distance is minimized.

Table 4-5. Body Phantom - Ratios of integrated counts (dose) show the effect of slice thickness on the helical scan dose profile. FOC dosimeters measured the integrated counts from helical dose profiles acquired at 120 kVp and 133 effective mAs in the five positions of a CTDI body phantom for two slice thicknesses and three pitches.

module	12 mm slice / 24 mm slice		
	pitch		
	0.5	1	1.5
top	1.26	1.38	1.40
left	1.29	1.34	1.37
right	1.25	1.35	1.42
bottom	1.23	1.26	1.31
center	1.18	1.27	1.31
average _(w)	1.23	1.31	1.35

The body phantom’s center and bottom ratios show an increase in dose (21, 27, and 31% for pitches of 0.5, 1.0, and 1.5, respectively) with decreasing slice thickness, but at a lesser rate than the other peripheries. This is due to the increased scatter-to-primary ratio (SPR) at these two phantom positions. For the center phantom position, the SPR is high relative to the peripheries due to the increase in phantom attenuation. At the bottom position, scatter contributions are increased and the primary beam is attenuated by the CT table. In comparing head and body phantom data, the ratios are similar since the minimal source-to-detector distance is the same for both bottom positions and the only difference is the limited dose attributed to scatter when the source-to-detector distance is at a maximum (nearly negligible for both).

Conclusions

Fiber-optic coupled dosimeters, based on the sensitive elements of coupled scintillation phosphors have been implemented in measuring the dose delivery methods of multi-detector computed tomography. Comprehensive analyses of computed tomography dose profiles have been performed using a fiber-optic coupled dosimetry system and standard PMMA dosimetry phantoms for various operating conditions of a Siemens Somatom Sensation 16-slice scanner. FOC dosimeters' sensitivity and reproducibility in the diagnostic energy range, along with their ability to directly measure the primary and scatter radiation associated with helical MDCT scanning, provide alternative methods for determining CT dose profiles and allow for the evaluation of CT dose characteristics not commonly observed by standard dosimeters.

CTDI Phantom Position

The effect of phantom position choice on the intensity of the measured dose profile fits well with measured single scan dose profile results performed by *Tsai et al.* using LiF TLDs and a GE ProSpeed CT scanner.²² However, helical scan dose profiles measured with fiber-optic coupled dosimeters provide information of CT delivery characteristics that more conventional computed tomography dosimetry metrics lack.

The small size of the fiber's active area allows for accurate point dose measurements. The fiber-optic dosimetry system allows for remote, real-time dose measurements. The direct recording of the helical scan profiles that characterize multi-detector CT can tell us more about the dose delivery of a given CT system than could a collected charge measurement from a standard pencil ion chamber. The fiber's real-time response also saves valuable time during measurements without the annealing of thermoluminescent dosimeters.

Helical dose profiles measured with FOC dosimeters and plotted versus time and/or phantom position portray the periodic motion of helical scanning from above to below the table

top, clearly seen in the peaks and valleys of the measured dose profiles as the scanner cycles around the dosimeter. Peaks in the dose profile correspond to an x-ray tube position closest to the detector and corresponding minima occur when the source-to-detector distance (and associated phantom and/or table attenuation) is at a maximum. Dose profiles acquired in the center position of CTDI phantoms show both a lowering and flattening out of the central dose peak due to the symmetry of x-ray attenuation from the cylindrical phantom and the constant source-to-detector distance. The scatter tails not measured by conventional CTDI₁₀₀ are also seen in helical dose profiles that scan the entire length of the phantom (Chapter 5).

Head vs. Body Phantom

Helical scan dose profiles display the attenuation effects of PMMA material and the CT table itself when fiber-optic dosimeters are placed in the various positions of the CTDI phantom. The top, left, and right periphery fiber responses are similar for profiles measured in the head phantom, while reduced intensities of the measured dose profiles' central dose are apparent for the bottom peripheries due to x-ray attenuation from the CT table. The center position dose profiles show a further increase in attenuation of x-rays due to the phantom material of the 16 cm diameter head phantom.

Body phantom data shows an even more significant reduction of dose at the center of the scan length in the measured profile as a result of the increased amount of phantom material when a larger diameter phantom is chosen. The lowering and flattening of the central dose and the broadening of the scatter tails in the central position dose profile is also enhanced due to the increased x-ray attenuation and the higher scatter-to-primary ratio of the larger diameter body phantom.

The top, left, and right periphery profiles show similar responses with respect to the peak dose at the center of the scan length and the intensity differences between the peaks and valleys.

The 32 cm diameter body phantom attenuates approximately 100% of incident x-rays when the tube is at a maximum distance from the dosimeter. The effect of table attenuation on the dose profile of the bottom phantom position is not as significant as in the head phantom (86%), though the intensity of the dose at the center of the scan length is still lower when compared to the other peripheries (91%).

Pitch

The measurement of single scan dose profiles only provides information regarding a single axial slice. Thus, the effect on changes in dose delivered due to a change in pitch in contiguous scanning cannot be determined from conventional SSDPs. However, helical scan dose profiles measured with fiber-optic coupled dosimeters can provide information regarding the characteristic effect of pitch on a CT system's dose delivery.

Measured data shows the increased dose typical of overscanning when scanner pitch is less than 1.0, despite the scanner's use of *effective* mAs to maintain dose with changes in pitch. Scan time of measured dose profiles increased at lower pitches and integrated dose increased accordingly with an average of 15-20% and 17-25% for the head and body phantoms, respectively. As pitch was increased from 1.0 to 1.5, measured dose profiles for the five CTDI positions showed an average *decrease* in dose of 9-13% for both the head and body phantoms.

The following chapter will show that the primary (central peak dose) dose delivered to a cylindrical PMMA phantom does not change significantly when pitch is changed. Therefore, the difference in dose ratios is due primarily to scatter radiation outside the center slice. When pitch is reduced, overscanning of the phantom allows for the measurement of the scatter tails at the edges of the phantom length and thus leads to an increase in dose.

Slice Thickness

As expected, the top, left, and right position dose ratios for the body phantom show a steady increase in dose of 27, 36, and 40%, for pitches of 0.5, 1.0, and 1.5, respectively, when slice thickness is reduced from 24 to 12 mm. These values are slightly higher than corresponding dose ratios in the head phantom due primarily to the detector's proximity to the radiation source and the added attenuation of the larger diameter phantom.

The body phantom's center and bottom ratios show an increase in dose with decreasing slice thickness, but at a lesser rate than the other peripheries. For the center phantom position, the scatter-to-primary ratio (SPR) is high relative to the peripheries due to the increase in phantom attenuation of the large diameter body phantom. At the bottom position, scatter contributions are increased and primary radiation is attenuated by the CT table. In comparing head and body phantom data, the ratios are similar since the minimal source-to-detector distance is the same for both bottom positions and the only difference is the limited dose attributed to scatter when the source-to-detector distance is at a maximum (nearly negligible for both).

CHAPTER 5 COMPUTED TOMOGRAPHY DOSE INDEX

Introduction

Analyses of single scan dose profiles measured with standard pencil ion chambers illustrate the shortfall of traditional CTDI to accurately predict the dose delivered from helical image acquisitions, by failing to sufficiently measure the scatter tail radiation characteristic of multi-detector computed tomography. The use of polymethylmethacrylate CTDI phantoms along with fiber-optic coupled dosimeters have shown potential in the direct measurement of the primary and scatter radiation associated with multi-detector, helical CT scanning. Fiber-optic dosimeters' ability to both discriminate the scatter tails associated with helical CT and measure the dose associated with scan lengths longer than the 100 mm of pencil ion chambers provide alternative methods for determining CT dose profiles.

CTDI₁₀₀

The computed tomography dose index (CTDI) was originally defined in order to characterize the radiation dose properties of single slice CT scanners. It is traditionally measured using a 100 mm long pencil ion chamber with 150 mm long, cylindrical polymethylmethacrylate (PMMA) dosimetry phantoms. Despite advancements in CT technology, CTDI remains a widely used metric for the dose performance of multi-detector CT (MDCT) and cone-beam CT (CBCT) scanners.⁴³⁻⁴⁴ Recently, however, the accuracy of the CTDI metric for patient dosimetry with modern multi-detector CT scanners has come into question.^{25-26,45-47}

Pencil Ion Chamber

The limitations of the computed tomography dose index-100 can be seen in its definition

$$\text{CTDI}_{100} = \frac{1}{T} \int_{-50\text{mm}}^{+50\text{mm}} f(z) dz \quad (5-1)$$

where $f(z)$ is the single, axial scan dose profile along a line parallel to the z -axis of the scanner

for nominal slick thickness T . If the scan length $L = 100$ mm, the 10 cm long pencil ion chamber will predict the maximum dose $D(0)$ at the center ($z = 0$) of the single scan profile as defined in Chapter 1. For shorter or longer scan lengths this is not necessarily true.²⁶

As the cumulative dose profile $D(z)$ (Eq. 1-6) builds up from the integration of single scan profiles $f(z)$, the dose in the central region flattens out and reaches an equilibrium value $D_{eq}(0)$ (Eq. 1-7) when L is large enough to encompass the scatter tails of $f(z)$.²⁶⁻²⁷ If the center dose reaches equilibrium for $L \leq 100$ mm, then the 10 cm long chamber will predict both $D_{eq}(0)$ and DLI (Eq. 1-8). If equilibrium is not reached, however, these quantities will be underestimated.²⁶

Small Volume Ion Chamber

Scan lengths utilized by most clinical exams are long enough such that the dose equilibrium should be reached in the center of the scan. Thus, the equilibrium dose can be measured if the chamber is long enough to encompass all the scatter tail radiation resulting from the single scan dose profile. Instead of making the ion chamber longer, *Dixon et al.* proposed an alternative to the CTDI method, suggesting the use of a small volume ion chamber to scan a length of phantom long enough to establish dose equilibrium at the location of the chamber.^{26,48}

The use of a small volume ion chamber to directly measure the cumulative dose $D(x)$ at any point by scanning a length of phantom long enough to produce dose equilibrium at the center of the scan length has the same result as making the chamber longer and is shown to be more accurate for wide beam profiles and scan lengths greater than 100 mm. Even if the scan length L is not long enough to produce equilibrium at the center, such a small chamber will give a good measurement of the maximum dose at the center, while a 10 cm chamber will merely give the average dose over the central 10 cm of the scan length.

Dixon and Ballard experimentally implemented the small ion chamber method by measuring the accumulated dose in a 400 mm long, 32 cm diameter PMMA body phantom for various scan lengths L including the equilibrium dose D_{eq} (or $CTDI_{\infty}$).⁴⁹ Their results showed good agreement in accumulated dose values ($\pm 2\%$) between small ion chamber and pencil ion chamber measurements when the scan length equaled the length of the pencil ion chamber, but failed to show similar correlation at more clinically relevant scan lengths. The measured equilibrium doses obtained by *Dixon and Ballard* at a scan length of 400 mm for GE MDCT scanners at 120 kVp were $CTDI_{\infty} = 1.75 CTDI_{100}$ on the central axis and $1.22 CTDI_{100}$ at the peripheries.⁴⁹

Nakonechny et al. showed that for nominal beam widths ranging from 3-20 mm and for scan lengths of 250 mm accumulated dose values at the center phantom position were approximately 25-30% higher than the measured $CTDI_{100}$. Peripheral point measurements were less severe, but differences were as much as 22%.⁴⁷ The authors measured SSDPs with PTW diamond detectors, lithium fluoride TLDs, and a small volume ion chamber. The profiles were acquired in elliptical water-equivalent phantoms (major and minor axes of 30 and 20 cm, respectively, and 30 cm in length) and the relative accumulated dose was measured at the center for various scan lengths L . The accumulated dose reached equilibrium for $L > 300$ mm (in agreement with *Dixon et al.*), suggesting the need for phantoms longer than standard CTDI phantoms.^{47,49} $CTDI_{100}$ measurements were also made using the small ion chamber and were within 4% of a 102 mm length pencil ion chamber for a scan length of $L = 100$ mm, further suggesting that dosimeters other than the standard 10 cm pencil ion chamber can be successful in clinical CT dosimetry.⁴⁷

Material and Methods

Fiber-Optic Coupled Dosimeters

Helical scan dose profiles measured with fiber-optic coupled dosimeters have shown potential in the characterization of multi-detector computer tomography dose delivery. Their ability to collect the scatter tails associated with helical CT suggests promise in measuring the accumulated dose of clinically relevant CT scan lengths where the use of standard pencil ion chambers fail. Chapter 4 described the use of PMMA phantoms and FOC dosimeters to measure helical scan dose profiles. The following sections analyze these dose profiles and illustrate the shortfall of $CTDI_{100}$ in accurately predicting the dose delivered from helical image acquisitions.

CTDI Efficiency

As previously discussed, recent studies have called into question the accuracy of the computed tomography dose index for patient dosimetry. *John Boone*²⁵ proposed an evaluation of the efficiency of the $CTDI_{100}$ metric using Monte Carlo simulation techniques. The CTDI efficiency ϵ was defined as the ratio of the average dose (accrued at $z = 0$) for multiple contiguous slices over a scan length of 100 mm, to the equilibrium dose accrued at $z = 0$, which is approached asymptotically as the scan length L becomes wider than the single scan dose profile, $D(z)$, to include the scatter tails (as $L \rightarrow \infty$).²⁵

$$\epsilon_{\infty} \equiv \frac{\frac{1}{nT} \int_{-50mm}^{z=50mm} D(z) dz}{\frac{1}{nT} \int_{-\infty}^{z=\infty} D(z) dz} = \frac{CTDI_{100}}{CTDI_{\infty}} \quad (5-1)$$

where $D(z)$ is the dose deposited for the single scan profile along the z -axis.

The Monte Carlo simulations utilized the geometry of a commercially available CT scanner with a modeled polyenergetic x-ray spectra. Infinitely long head (16 cm diameter) and body (32 cm) PMMA phantoms were modeled and dose spread functions (DSFs) were computed

along the length of 12.4 mm diameter PMMA rods placed at radii reflecting the five positions of standard CTDI phantoms. The $CTDI_{100}$ efficiency was then calculated as the fraction of the dose along a PMMA rod collected in a 100 mm length scan centered on the CT slice position, divided by the total dose deposited along an infinitely long PMMA rod.²⁵

This method was adopted to calculate the efficiency of $CTDI_{100}$ with respect to the helical scan dose profiles (Chapter 4) measured with fiber-optic coupled dosimeters at the five positions of standard PMMA head and body phantoms under various operating conditions. The $CTDI_{100}$ efficiency was determined as the ratio of the accumulated dose integral measured in the center 100 mm of the phantom divided by the total 150 mm scan length of the PMMA phantom that includes the scatter edges.

$$\epsilon_{150} \equiv \frac{CTDI_{100mm}}{CTDI_{150mm}} \quad (5-2)$$

Need for Longer Phantoms

Helical dose profiles have been measured at the center and peripheral locations of CTDI phantoms since computed tomography dose varies across the field of view. The weighted CTDI (discussed in Chapter 1) takes into account the fact that dose is distributed unevenly in the axial (x - y) plane. This is especially true for the center position of the larger diameter body phantom, as the scatter-to-primary ratio increases with increasing phantom diameter thickness⁵⁰ (see Figure 4-5 and Tables 4-3, 4-5). Where $CTDI_w$ represents the average absorbed dose in the x - y plane, the volume computed tomography dose index ($CTDI_{vol}$) estimates the average radiation dose within the irradiated volume of the CTDI phantom. It does not, however, represent the average dose for objects of substantially different size, shape, attenuation or when the 100 mm integration limits omit a considerable fraction of the scatter tails.²⁵

Recent studies implementing the use of a small ion chamber to measure the accumulated dose, including the equilibrium dose $D_{eq}(0)$, at the center of various scan lengths have suggested the need for longer phantoms, stating that the equilibrium dose ($CTDI_{\infty}$) is reached for scan lengths $L > 300$ mm.^{47,49} *Dixon and Ballard* suggested that the commonly used phantom length of 150 mm is too short even for the measurement of $CTDI_{100}$, producing an underestimate of 7.3% on the central axis and 1.3% on the peripheral when compared to $CTDI_{100}$ measurements in a 400 mm long PMMA phantom.⁴⁹

Novel method for predicting helical scan dose profiles

To evaluate the need for longer phantoms to measure the scatter tails associated with clinically relevant scan lengths, helical dose profiles were acquired using fiber-optic coupled dosimeters and extended length (300 mm) PMMA head (16 cm diameter) and body (32 cm) phantoms. Scans were for performed for the combination of scan parameters listed in Table 5-1, using the same tube potential and effective mAs settings as the profiles measured in Chapter 4, differing only in the scan time needed (and a result, the dose accumulated) due to the extended length of the double phantoms.

Table 5-1. Helical scan dose profiles – Operating conditions. Scans were performed using double length ($L = 300$ mm) head and body CTDI phantoms, at three pitches and two slice thicknesses for the five positions of each phantom.

Phantom ^a	kVp	effective mAs	position	pitch	slice thickness
Head	120	82	Top	0.5	12 mm
Body	120	133	Bottom	1	24 mm
			Center	1.5	
			Left		
			Right		

^aDouble phantom length ($L = 300$ mm)

To measure helical scan dose profiles in extended length phantoms, two standard CTDI head phantoms (15 cm length, 16 cm diameter) were stacked end to end to achieve a 300 mm phantom length. The same method was repeated for the body phantom. The active area of the fiber-optic dosimeter was placed in the center ($z = 7.5$ cm) of the first (15 cm length) phantom for each position of the head and body phantoms, respectively, and CT acquisitions were performed for the entire length of the double phantom ($L = 300$ mm). When the dose profile is plotted versus phantom position, the dose peak occurs at $z = 7.5$ cm (Figure 5-1).

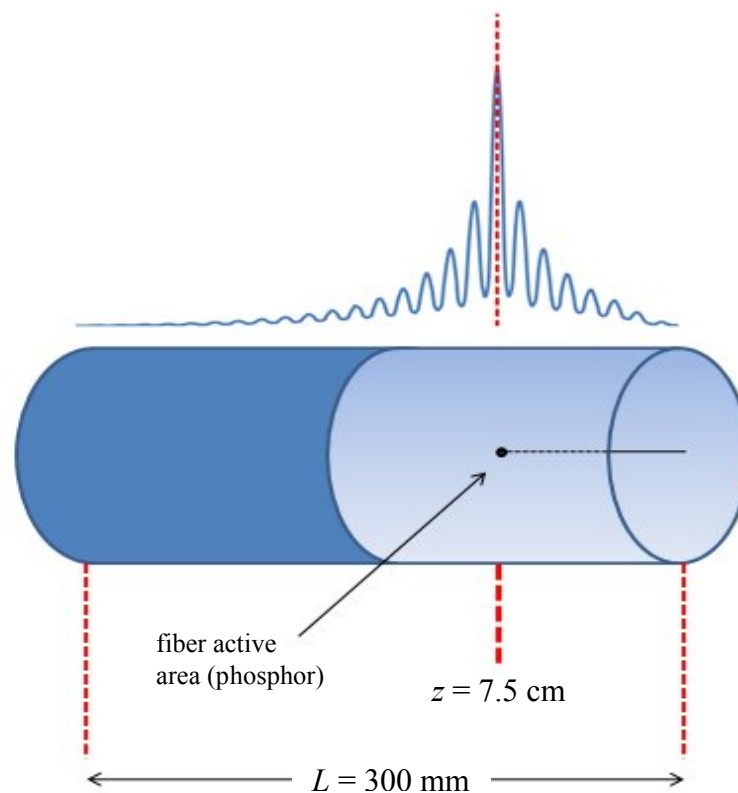


Figure 5-1. Diagram of the 300 mm length phantom setup. Two 150 mm length phantoms were stacked end to end with the active area of the fiber-optic dosimeter positioned in the center ($z = 7.5$ cm) of the first phantom.

Positioning the FOC dosimeter at $z = 7.5$ cm in the 300 mm length phantoms provides a method for predicting the helical dose profiles for both a 150 mm and 450 mm length phantom.

The methodology that follows explains a setup to predict two separate phantom length dose

profiles in a single measurement. In the case of the 450 mm length scan, only two 15 cm length phantoms are needed instead of three, which is beneficial when using cumbersome 32 cm diameter body phantoms.

The first 7.5 cm of the 300 mm phantom profile mirrors the first half of the single phantom profiles measured in Chapter 4 (for equal phantom diameter, location, and scan parameters).

Figure 5-2 illustrates dose profiles measured in the center position of the CTDI head phantom for a 24 mm slice thickness and pitch of 0.5. The first 7.5 cm of the 300mm phantom dose profile ($z = 0$ to 7.5 cm) is reflected across the center dose peak and superimposed on the single phantom dose profile. The two dose profiles show good correlation and are within 1.88% in accumulated dose across a 15 cm scan length.

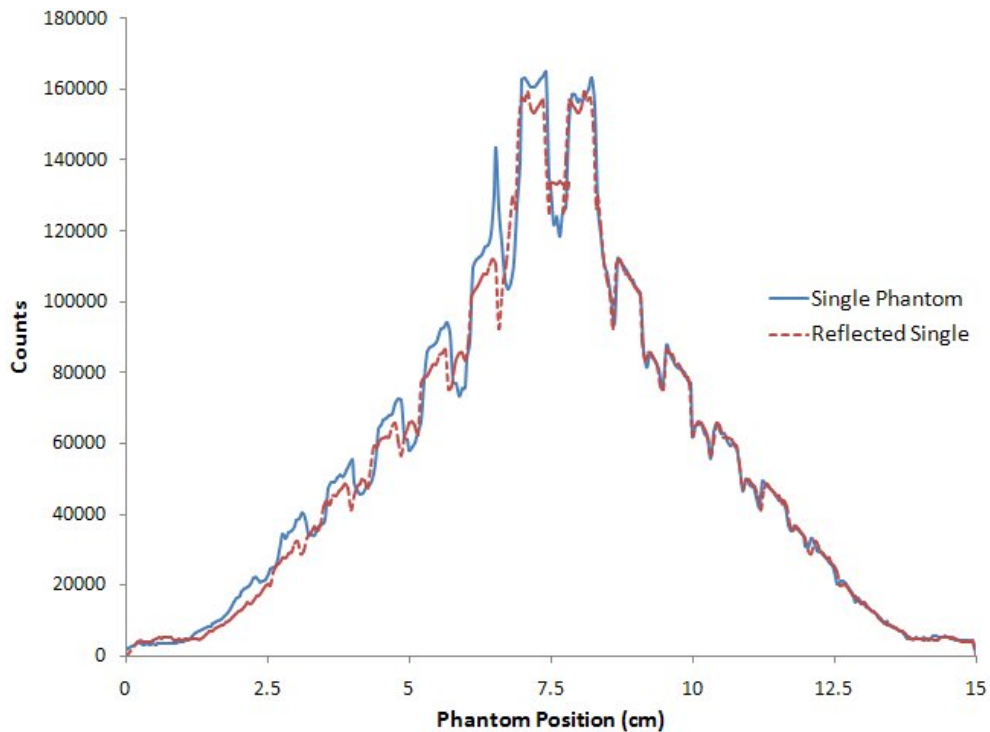


Figure 5-2. Helical scan dose profiles in the center position of CTDI head phantoms measured with fiber-optic coupled dosimeters. CT scans were performed at 120 kVp and 82 effective mAs for a selected pitch of 0.5 and a slice thickness of 24 mm. Plotted are the dose profiles measured in (1) a single (15 cm length) head phantom and (2) the reflected first 7.5 cm of a dose profile measured in a 300 mm length phantom with FOC dosimeter placed at $z = 7.5$ cm.

Figure 5-3 gives another example of the similarities between helical scan dose profiles measured across the length of the single phantom (15 cm) and the reflected first 7.5 cm of the dose profile measured in the 300 mm phantom with FOC dosimeter placed at $z = 7.5$ cm. Plotted are the dose profiles measured from CT scans performed at 120 kVp and 82 effective mAs for a selected pitch of 1.0 and a slice thickness of 24 mm in the top (12 o'clock) position of the CTDI head phantom. Again, the accumulated dose for the two profiles showed good agreement (within 5.62%). Table 5-2 lists the percent difference in accumulated dose for the two single phantom profiles (measured/reflected) acquired at all slice thickness and pitch combinations for the center and peripheries of the CTDI head phantom.

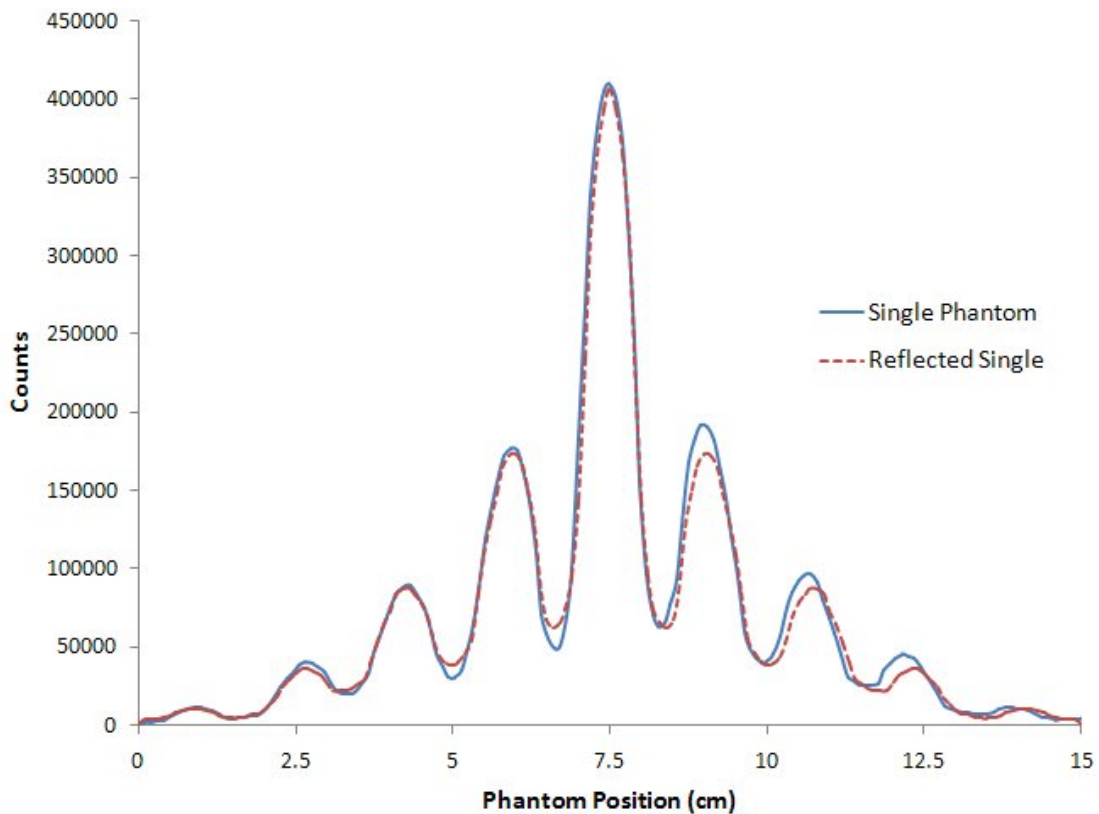


Figure 5-3. Helical scan dose profiles in the 12 o'clock position of CTDI head phantoms measured with fiber-optic coupled dosimeters. CT scans were performed at 120 kVp and 82 effective mAs for a selected pitch of 1.0 and a slice thickness of 24 mm. Plotted are the dose profiles measured in a single (15 cm length) head phantom and the reflected first 7.5 cm of a dose profile measured in a 300 mm length phantom with FOC dosimeter placed at $z = 7.5$ cm.

Table 5-2. Calculated percent difference in accumulated dose across a 15 cm scan length for the measured single head phantom profile and the reflected first 7.5 cm of the 300 mm length phantom profile

slice thickness	12 mm			24 mm		
pitch	0.5	1	1.5	0.5	1	1.5
module	Percent Difference in Accumulated Dose Profiles Single Phantom / Reflected (z = 0 to 7.5 cm) Double Phantom					
Center	1.13%	2.71%	2.22%	1.88%	2.25%	2.40%
Top	4.24%	4.19%	NA	3.07%	5.62%	0.68%
Bottom	4.43%	3.88%	9.45%	3.16%	2.95%	3.61%
Left	5.37%	7.82%	8.24%	3.20%	3.49%	3.93%

CTDI_{L(mm)}

Reflecting the first 7.5 cm of a dose profile measured in an $L = 300$ mm length PMMA phantom with a FOC dosimeter placed at $z = 7.5$ cm successfully predicts the dose delivered to a full 15 cm length phantom of the same diameter. Using that methodology, the remaining length of the dose profiles ($z = 7.5$ to 30 cm) measured in the 300 mm length phantom study were reflected about the dose peak ($z = 22.5$ cm) to predict the helical scan dose profile in a 450 mm length PMMA phantom. Implementation of such a protocol reduced the amount of equipment (two phantoms instead of three in this case) needed to measure the dose in longer length phantoms.

The accumulated dose measured from 450 mm length helical dose profiles (reflected 22.5 cm of the double phantom study) was then compared to the integrated dose across the dose profiles acquired in a single (150 mm length) phantom. Comparisons were made for both the head and body phantom, respectively, for the various scan parameters listed in Table 5-1. Also analyzed was *Dixon and Ballard's*⁴⁹ suggestion that the commonly used phantom length of 150 mm is too short even for the measurement of CTDI₁₀₀. The CTDI₁₀₀ efficiency in the 150 mm

length was thus reevaluated in comparison with similar CTDI₁₀₀ efficiency calculations using the 450 mm length helical scan dose profiles.

Results and Discussion

CTDI₁₀₀ Efficiency

Table 5-3 lists the calculated CTDI₁₀₀ efficiency for helical scan dose profiles measured with FOC dosimeters in the five positions of standard length (15 cm) PMMA head (16 cm diameter) and body (32 cm) phantoms for two slice thicknesses (12, 24 mm) and three pitches (Table 4-1). The ϵ_{150} was determined as the ratio of the accumulated dose integral measured in the center 100 mm of each respective phantom divided by the total 150 mm scan length of the PMMA phantom that includes the scatter edges. The ϵ_{150} efficiency at the four peripheries (top, left, right, bottom) has been averaged and compared with corresponding values at the center position of the two phantoms.

Table 5-3 also compares the ϵ_{150} with respect to changes in slice thickness. Profiles measured at varying pitches (0.5, 1.0, 1.5) for a given slice thickness showed little change as seen in the measured variance for CTDI efficiencies in Table 5-4. As a result, the ϵ_{150} efficiencies listed were calculated as the average of measured values at three pitches for each given slice thickness and phantom position permutation.

The efficiencies measured show good agreement with *Boone's* data at all slice thicknesses for peripheries of the head and body phantom. Such agreement is not seen, however, at the center of the two phantoms. Neither is there a decrease in efficiency at larger beam widths for the measured CTDI₁₀₀ as predicted from the simulations performed by *Boone*. This is due to the finite size of the phantom resulting in the inability to record the scatter of larger beam widths that extend beyond the limits of the phantom.

Table 5-3. CTDI₁₀₀ efficiency (ϵ_{150}) calculated as the ratio of the accumulated dose measured in the center 100 mm of a standard PMMA phantom divided by the total 150 mm scan length of the phantom. Efficiencies were determined from helical scan dose profiles acquired at the five locations of standard head and body phantoms for slice thicknesses of 12 and 24 mm. Three scans (for three pitches) were acquired at each combination of location and slice thickness and then averaged. Also listed are Monte Carlo simulations performed by *Boone*²⁵ for calculating CTDI₁₀₀ efficiency (ϵ_{∞}) as the ratio of the accumulated dose measured in the center 100 mm of an infinitely long PMMA phantom divided by the total dose in the infinite phantom.

slice thickness	Center			
	Head Phantom		Body Phantom	
	12 mm	24 mm	12 mm	24 mm
ϵ_{150}	0.92	0.95	0.90	0.95
ϵ_{∞}	0.82 ^a	0.81 ^b	0.63 ^a	0.62 ^b
slice thickness	Peripheries _{avg}			
	Head Phantom		Body Phantom	
	12 mm	24 mm	12 mm	24 mm
ϵ_{150}	0.92	0.95	0.92	0.95
ϵ_{∞}	0.90 ^a	0.89 ^b	0.88 ^a	0.87 ^b

^aCalculated with profiles acquired at slice thickness of 10 mm

^bSlice thickness of 20 mm

It should be noted that these comparisons are made between the physical measurements performed in this study and idealized Monte Carlo simulations. For the Monte Carlo simulations, the x-ray source was simulated as a point source. Therefore, there is no blurring of the dose distributions due to x-ray beam penumbra. X-ray spectra and bow-tie filters were modeled after GE scanner and the effect of table attenuation on the integral dose profile is neglected.

CTDI_{L(mm)}

As previously discussed, reflecting the first 7.5 cm of the dose profiles measured in the 300 mm length phantom setup with a FOC dosimeter placed at $z = 7.5$ cm successfully predicts the

dose delivered to the full 150 mm length phantom of the same diameter. The remaining 22.5 cm of the 300 mm phantom profiles ($z = 7.5$ to 30 cm) were reflected about the dose peak ($z = 22.5$ cm) to predict the helical scan dose profile in a 450 mm (triple length) PMMA phantom. The accumulated dose measured along the triple phantom helical dose profiles was then compared to the integrated dose across the dose profiles acquired in the single phantom.

Table 5-4. Variance of ϵ_{150} efficiencies calculated from helical scan dose profiles acquired at three pitches for each combination of slice thickness and phantom position utilized. Scans were acquired at the five positions of both the head and body PMMA phantoms for two slice thicknesses at each position.

slice thickness	Head Phantom		Body Phantom	
	12 mm	24 mm	12 mm	24 mm
	Variance			
Center	1.07%	0.48%	2.05%	1.23%
Peripheries _{avg}	1.03%	0.90%	1.16%	1.09%

Table 5-5 lists the accumulated dose ratios of the 450 and 150 mm length dose profiles ($CTDI_{450} / CTDI_{150}$) for the head (16 cm diameter) phantom. As shown in Table 5-2, accumulated dose values for the single head phantom dose profiles were slightly larger than the corresponding reflected ($z = 0$ to 7.5 cm) 150 mm profiles. For comparison, Table 5-6 gives the dose ratios ($CTDI_{450} / CTDI_{150}$) for the reflected triple (450 mm length) phantom dose profiles versus the reflected single phantom helical scan dose profiles.

The accumulated dose ratios given in Tables 5-5 and 5-6 verify the failure of CTDI measurements, performed in a standard 150 mm length phantom, to sufficiently measure the scatter radiation of clinically relevant scan lengths. Accumulated dose values for the measured single head phantom dose profiles (Table 5-5) were slightly larger than the corresponding reflected ($z = 0$ to 7.5 cm) 150 mm profiles (Table 5-6). Even taking the conservative approach,

accumulated dose measured in the 150 mm length phantom underestimates the scatter radiation of the helical dose profile by an average of 24, 19, 14, and 22% for the center, top, left, and bottom phantom positions, respectively, when compared to the accumulated dose in the 450 mm length profile.

Table 5-5. Accumulated dose ratios measured from helical dose profiles of 450 mm and 150 length PMMA *head* phantoms. Calculated ratios reflect the increased dose due to the accumulation of extended scatter tails associated with longer phantoms. Single phantom doses were calculated from helical dose profiles measured in Chapter 4 while $z = 7.5$ to 30 cm of the double phantom study were reflected about the peak dose ($z = 7.5$ cm) to predict the helical dose profiles for a 45 cm length phantom.

slice thickness	12 mm			24 mm		
pitch	0.5	1	1.5	0.5	1	1.5
module	CTDI ₄₅₀ / CTDI ₁₅₀ *					
Center	1.20	1.24	1.25	1.22	1.24	1.27
Top	1.13	1.16	NA	1.18	1.22	1.28
Left	1.10	1.16	1.22	1.04	1.12	1.18
Bottom	1.21	1.21	1.26	1.20	1.23	1.24

*Calculated from single phantom dose profiles measured in Chapter 4.

Table 5-6. Accumulated dose ratios measured from reflected helical dose profiles of 450 mm and 150 length PMMA *head* phantoms. Calculated ratios show the increased dose due to the accumulation of extended scatter tails associated with longer phantoms. Single phantom (150 mm length) dose profiles were predicted from the reflected first 7.5 cm of the double phantom study, while $z = 7.5$ to 30 cm was reflected about the peak dose ($z = 7.5$ cm) to predict the dose profiles for a 450 mm length phantom.

slice thickness	12 mm			24 mm		
pitch	0.5	1	1.5	0.5	1	1.5
module	CTDI ₄₅₀ / CTDI ₁₅₀ **					
Center	1.22	1.27	1.28	1.24	1.27	1.30
Top	1.18	1.21	1.23	1.21	1.29	1.29
Left	1.16	1.26	1.33	1.07	1.16	1.23
Bottom	1.26	1.26	1.39	1.24	1.27	1.28

**Calculated from reflected $z = 0$ to 7.5 cm for the double phantom dose profile

The higher dose ratios ($CTDI_{450} / CTDI_{150}$) for the bottom and center positions are due to the higher scatter-to-primary ratios since the central dose peak does not change when comparing the 150 mm and 450 mm length scans. Figure 5-4 simultaneously displays the helical scan dose profiles (center position, head phantom, 0.5 pitch, 24 mm slice thickness) of the measured single phantom and the reflected 150 and 450 mm length phantoms. Figure 5-5 similarly displays the three helical scan dose profiles measured in the top position of the PMMA head phantom for a pitch of 1.0 and 24 mm slice thickness. The figures provides strong visual evidence to the fact that the 150 mm length dose profile significantly fails to measure the scatter tails associated with longer scan lengths. Also evident is the fact that the center peak does not change as the phantom size is lengthened (i.e. accumulated dose differences in the corresponding profiles are attributed solely to scatter radiation).

The simultaneous prediction of the helical dose profiles for both a 150 and 450 mm length phantom in a single measurement is especially helpful when working with heavy 32 cm diameter body phantoms. As explained for the head phantom, the FOC dosimeter was placed at $z = 7.5$ cm in the 300 mm length body phantom and the measured profile was reflected about the peak dose ($z = 7.5$ cm) to predict the helical scan dose profiles for both the 150 and 450 mm phantom lengths.

Accumulated dose ratios for the two predicted dose profiles in the 32 cm diameter body phantom are listed in Table 5-7. The higher dose ratios ($CTDI_{450} / CTDI_{150}$) for the bottom and center positions (compared to the other peripheries) are due to the higher scatter-to-primary ratios (SPRs) at these positions since the central dose peak does not change when comparing the 150 mm and 450 mm length scans. The bottom and center ratios are also higher when compared

to head phantom data (Table 5-5) since the SPRs increase with increasing phantom diameter thickness.

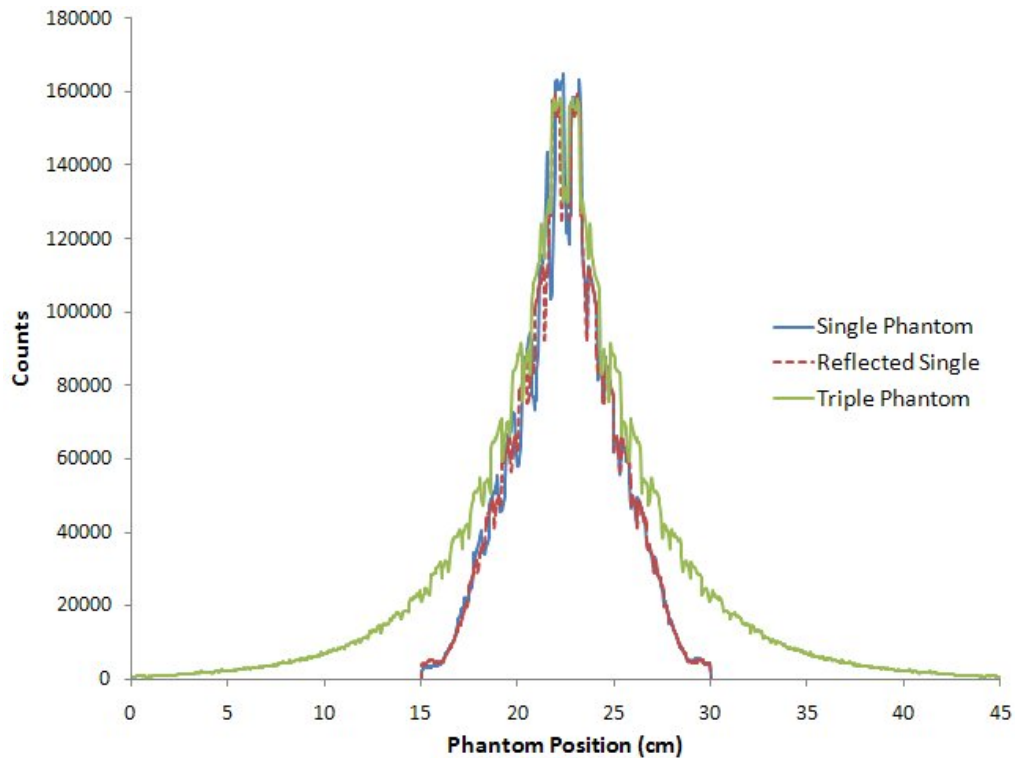


Figure 5-4. Helical scan dose profiles in the center position of CTDI head phantoms measured with fiber-optic coupled dosimeters. CT scans were performed at 120 kVp and 82 effective mAs for a selected pitch of 0.5 and a slice thickness of 24 mm. Plotted are the dose profiles measured in a single (15 cm length) head phantom, the reflected first 7.5 cm of a dose profile measured in a 300 mm length phantom with FOC dosimeter placed at $z = 7.5$ cm, and the reflected 450 mm length profile.

Table 5-7 also displays a significant increase in dose ratios with corresponding increases in pitch. This trend is also seen in the head phantom ratios (Table 5-5, 5-6), but not as extensively as in the larger diameter body phantom. As pitch is increased, scatter-to-primary ratios increase as well at points further away from the peak dose. Thus, for dose profiles acquired in longer (450 mm) length phantoms that collect the extended scatter tails not measured in shorter (150 mm) phantoms, dose ratios increase with pitch. In the body phantom, where scatter-to-primary ratios are already high to begin with, this trend can be even more significant.

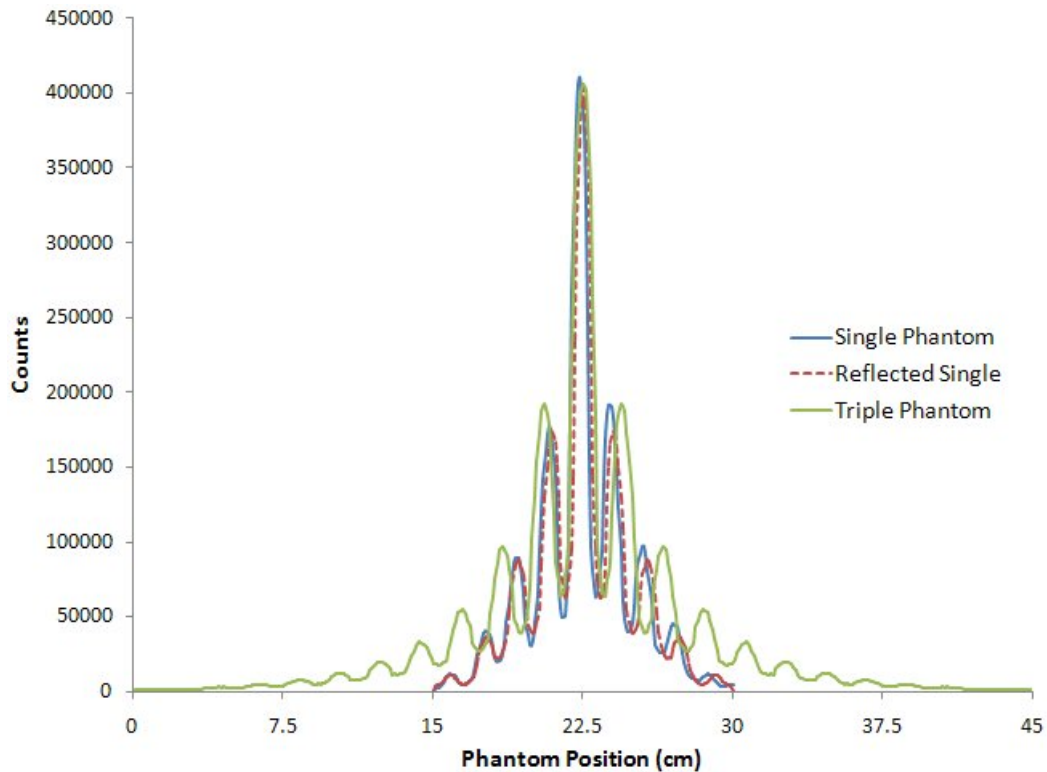


Figure 5-5. Helical scan dose profiles in the 12 o'clock (top) position of CTDI head phantoms measured with fiber-optic coupled dosimeters. CT scans were performed at 120 kVp and 82 effective mAs for a selected pitch of 1.0 and a slice thickness of 24 mm. Plotted are the dose profiles measured in a single (15 cm length) head phantom, the reflected first 7.5 cm of a dose profile measured in a 300 mm length phantom with FOC dosimeter placed at $z = 7.5$ cm, and the reflected 450 mm length profile.

Table 5-7. Accumulated dose ratios measured from helical dose profiles of 450 mm and 150 length PMMA *body* phantoms. Single phantom (150 mm length) dose profiles were predicted from the reflected first 7.5 cm ($z = 0$ to 7.5 cm) of the double phantom study, while $z = 7.5$ to 30 cm was reflected about the peak dose ($z = 7.5$ cm) to predict the helical dose profiles for a 450 mm length phantom.

slice thickness	12 mm			24 mm		
pitch	0.5	1	1.5	0.5	1	1.5
module	CTDI ₄₅₀ / CTDI ₁₅₀ **					
Center	1.31	1.35	1.42	1.43	1.47	1.56
Top	1.10	1.13	1.24	1.27	1.38	1.58
Left	1.19	1.28	1.33	1.30	1.38	1.38
Bottom	1.33	1.47	1.52	1.43	1.49	1.58

**Calculated from reflected $z = 0$ to 7.5 cm for the 300 mm length phantom dose profile

CTDI₁₀₀ Efficiency Revisited

The ϵ_{450} was determined as the ratio of the accumulated dose integral measured in the center 100 mm of the predicted head and body phantom dose profiles divided by the total 450 mm scan length of the PMMA phantom that includes the scatter edges. Also listed are the ϵ_{150} efficiencies measured above and the corresponding CTDI₁₀₀ efficiencies simulated by *Boone*.²⁵

Table 5-8. CTDI₁₀₀ efficiency (CTDI₁₀₀ / CTDI_L) calculated as the ratio of the accumulated dose measured in the center 100 mm of a standard PMMA phantom divided by the total scan length L of the phantom. CTDI₁₀₀ efficiencies were calculated for 150 mm (ϵ_{150}) and 450 mm (ϵ_{450}) length dose profiles. Also listed are Monte Carlo simulations performed by *Boone* for calculating CTDI₁₀₀ efficiency (ϵ_{∞}) as the ratio of the accumulated dose measured in the center 100 mm of an infinitely long PMMA phantom divided by the total dose in the infinite phantom.

slice thickness	Center			
	Head Phantom		Body Phantom	
	12 mm	24 mm	12 mm	24 mm
ϵ_{150}	0.92	0.95	0.90	0.95
ϵ_{450}	0.71	0.71	0.59	0.61
ϵ_{∞}	0.82 ^a	0.81 ^b	0.63 ^a	0.62 ^b
slice thickness	Peripheries _{avg}			
	Head Phantom		Body Phantom	
	12 mm	24 mm	12 mm	24 mm
ϵ_{150}	0.92	0.95	0.92	0.95
ϵ_{450}	0.74	0.74	0.72	0.70
ϵ_{∞}	0.90 ^a	0.89 ^b	0.88 ^a	0.87 ^b

^aCalculated with profiles acquired at slice thickness of 10 mm

^bslice thickness of 20 mm

The ϵ_{450} efficiency at the four peripheries (top, left, right, bottom) has been averaged and compared with corresponding values at the center position of the two phantoms. Profiles predicted at varying pitches (0.5, 1.0, 1.5) for a given slice thickness showed little change, given by the variance (Table 5-9). Therefore, the ϵ_{450} efficiencies listed were calculated as the average of measured values at the three pitches for each given slice thickness and phantom position permutation.

Table 5-9. Variance of ϵ_{450} efficiencies calculated from helical scan dose profiles acquired at the three pitches for each combination of slice thickness and phantom position utilized. Scans were predicted for the five positions of both the head and body PMMA phantoms for two slice thicknesses at each position.

slice thickness	Head Phantom		Body Phantom	
	12 mm	24 mm	12 mm	24 mm
	Variance			
Center	1.39%	1.86%	0.50%	0.47%
Peripheries _{avg}	3.09%	3.35%	2.90%	7.26%

The ϵ_{150} efficiencies measured earlier showed good agreement with *Boone's* data at all slice thicknesses for peripheries of both the head and body phantoms. Such agreement was not seen, however, at the center of the two phantoms due to the finite size of the 150 mm length phantom, resulting in the inability to record the scatter of larger beam widths that extend beyond the limits of the phantom. The ϵ_{450} efficiencies, on the other hand, show good agreement with *Boone's* simulations in the center position as the longer length (450 mm) phantom is sufficient in collecting the scatter tail contributions at the edges of the dose profiles. The ϵ_{450} , however,

overestimates the scatter contributions in the peripheries when compared to the other CTDI efficiency metrics (ϵ_{150} , ϵ_{∞}).

Conclusions

Analyses of single scan dose profiles measured with standard pencil ion chambers^{22,25-26} have illustrated the shortfall of traditional CTDI to accurately predict the dose delivered from helical image acquisitions. Fiber-optic dosimeters' ability both discriminate the scatter tails associated with helical CT and measure dose for clinically relevant scan lengths where ion chamber collected charge measurements fail gives credence to the already established thought that longer phantoms are needed for clinical CT dosimetry.^{47,49}

Novel Method for Predicting Helical Scan Dose Profiles

Outlined above is a novel and yet simple method for predicting helical scan dose profiles using fiber-optic coupled dosimeters in extended length phantoms. The active area of the fiber-optic dosimeter was placed at $z = 7.5$ cm in a 300 mm length PMMA phantom and CT acquisitions were performed for the entire length of the phantom ($L = 300$ mm). When the dose profile is plotted versus phantom position, the dose peak occurs at $z = 7.5$ cm (Figure 5-1). By reflecting both sides of the dose profile across the center line in the peak dose, helical dose profiles for both a 150 and 450 mm length phantom can be simultaneously predicted in a single measurement.

Need for Longer Phantoms

Accumulated dose ratios ($CTDI_{450} / CTDI_{150}$) of these predicted profiles verify the failure of CTDI measurements, performed in a standard 150 mm length phantom, to sufficiently measure the scatter radiation of clinically relevant scan lengths. Figures 4-4 and 4-5 illustrate the fact that 150 mm length dose profiles fail significantly to measure the scatter tails associated with longer scan lengths. The figures show that the center peak does not change as the phantom

size is lengthened and thus, accumulated dose differences in longer (e.g. 450 mm length) phantoms when compared to shorter (150 mm) phantom profiles are ascribed almost exclusively to scatter radiation.

CHAPTER 6 CONCLUSIONS

Prototypical Fiber-Optic Coupled Point Dosimetry System

Fiber-optic coupled dosimeters based on the sensitive elements of a coupled scintillation phosphor demonstrate strong sensitivity, reproducibility, and excellent dose linearity across the diagnostic energy range. The dosimetry system's radiation detection capabilities are due to the absorption of x-rays in a gadolinium oxy-sulfate scintillation phosphor material that is coupled to the end of a fused silica, 400 μm diameter, optical fiber. The phosphor's absorption of incident x-rays via the photoelectric effect provides a conversion of x-ray photon energy to visible light, which then travels the length of the fiber to a photomultiplier tube (PMT). The PMT converts the incident light photons to an output voltage signal proportional to the number of light photons incident at the photomultiplier tube interface. This output is then relayed in terms of (photon) *counts* to a PC.

The FOC point dosimeter approach provides remote detection of the dose associated with diagnostic imaging modalities such as x-ray and computed tomography (CT). The real-time response of the system allows for the direct recording of helical scan dose profiles that contain the essential information for the characterization of the dosimetry quantities fundamental to multi-detector computed tomography. The acquisition of empirical helical scan dose profiles using FOC dosimeters distinguishes the primary radiation from the scatter contributions that makeup the dose delivery of a given CT system and isolate the effect of specific scanner parameters on patient absorbed dose.

Helical Computed Tomography Dose Profiles

Helical scan dose profiles measured with fiber-optic coupled dosimeters and plotted versus time and/or phantom position provide information of CT delivery characteristics that more

traditional computed tomography dosimetry metrics lack. They portray the periodic motion of helical scanning from above to below the table top, clearly seen in the peaks and valleys of the measured dose profiles as the scanner cycles around the dosimeter. Peaks in the dose profile correspond to an x-ray tube position closest to the detector. Corresponding minima occur when the source-to-detector distance is at a maximum and demonstrate the effect of phantom and/or table attenuation on patient absorbed dose. Dose profiles acquired in the center position of CTDI phantoms show both a lowering and flattening out of the central dose peak due to the symmetry of x-ray attenuation from the cylindrical phantom and the constant source-to-detector distance. The scatter tails not measured by conventional $CTDI_{100}$ are also seen in helical dose profiles that scan the entire length of the phantom.

Helical scan dose profiles display the attenuation effects of PMMA material and the CT table itself when fiber-optic dosimeters are placed in the various positions of the CTDI phantom. Body phantom data shows an even more significant reduction of dose at the center of the scan length in the measured profile as a result of the increased amount of phantom material when a larger diameter phantom is chosen. The lowering and flattening of the central dose and the broadening of the scatter tails in the central position dose profile is also enhanced due to the increased x-ray attenuation and the higher scatter-to-primary ratio of the larger diameter body phantom.

The measurement of single scan dose profiles only provides information regarding a single axial slice. Thus, the effect on changes in dose delivered due to a change in pitch in contiguous scanning cannot be determined from conventional SSDPs. However, helical scan dose profiles measured with fiber-optic coupled dosimeters can provide information regarding the characteristic effect of pitch on a CT system's dose delivery. Measured data shows the increased

dose typical of overscanning when scanner pitch is less than 1.0, despite the scanner's use of *effective* mAs to maintain dose with changes in pitch. The primary (central peak) dose delivered to a cylindrical PMMA phantom does not change significantly when pitch is changed.

Therefore, the overscanning typical of low pitch selection leads to an increase in dose due to FOC dosimeter efficient measurement of the scatter radiation at the edges of standard dosimetry phantom lengths.

Novel Method for Predicting Helical Scan Dose Profiles

Analyses of single scan dose profiles measured with standard pencil ion chambers have illustrated the shortfall of traditional CTDI to accurately predict the dose delivered from helical image acquisitions. Fiber-optic dosimeters' ability both discriminate the scatter tails associated with helical CT and measure dose for clinically relevant scan lengths where ion chamber collected charge measurements fail gives credence to the already established thought that longer phantoms are needed for clinical CT dosimetry.

A novel and yet simple method for predicting helical scan dose profiles using fiber-optic coupled dosimeters in extended length phantoms was developed in this study. The active area of the fiber-optic dosimeter was placed at $z = 7.5$ cm in a 300 mm length PMMA phantom and CT acquisitions were performed for the entire length of the phantom ($L = 300$ mm). When the dose profile is plotted versus phantom position, the dose peak occurs at $z = 7.5$ cm. By reflecting both sides of the dose profile across the center line in the peak dose, helical dose profiles for both a 150 and 450 mm length phantom can be simultaneously predicted in a single measurement.

Need for Longer Phantoms

Accumulated dose ratios ($CTDI_{450} / CTDI_{150}$) of these predicted profiles verify the failure of CTDI measurements, performed in a standard 150 mm length phantom, to sufficiently measure the scatter radiation of clinically relevant scan lengths. An evaluation of the $CTDI_{100}$

metric in various length phantoms along with plots of their corresponding dose profiles (Figures 4-4 and 4-5) show that the center peak does not change as the phantom size is lengthened. Thus, accumulated dose differences in longer (e.g. 450 mm length) phantoms when compared to shorter (150 mm) phantom profiles are ascribed almost exclusively to scatter radiation.

Future Work

Extended Characterization of the Point Dosimetry System

Fiber-optic coupled dosimeters show strong energy dependence, specifically sensitivity to lower energies in the diagnostic range, due to the photoelectric absorption K-edge (50 keV) of the gadolinium oxy-sulfate scintillation phosphor. An extended characterization of the point dosimetry system is therefore needed to calibrate fiber response relative to the energy technique chosen. An inherent angular dependence seen in the fiber's coupled active area must also be re-addressed. The sinusoidal response with perpendicular-to-axial fiber positioning can be significantly reduced when the dose measurements are performed within a scattering medium. An angular dependence for axial positioning, when the x-ray tube is directed "head-on" still remains.

Verification of Predicted Dose Profiles in Extended Length Phantoms

This study provided a simple method for determining the helical scan dose profiles of extended length phantoms when extra phantom equipment is either unavailable or too cumbersome to transport. By placing the FOC dosimeter at $z = 7.5$ cm in a 300 mm length phantom, two helical scan dose profiles could be predicted (150 and 450 mm length phantoms) in a single measurement. The effectiveness of the 150 mm length phantom predicted dose profiles was verified when compared to measured helical scan dose profiles across the entire 150 mm length phantom. Central peak and scatter dose contributions to the profiles showed good correlation with integral dose measurements across the profile length having strong agreement.

Physical measurements 450 mm length PMMA phantom profiles are therefore needed to verify the accuracy of the corresponding predicted profiles for this phantom length.

Multi-Fiber-Optic Coupled Dosimeter System

Development of a multi-fiber system to allow for the simultaneous recording of multiple absorbed dose measurements has begun in the Nuclear & Radiological Engineering Department at the University of Florida under the advisement of Dr. David Hintenlang. The fiber-optic coupled dosimeters are based on the same properties of the couple scintillation phosphors as described in this study. Multiple photo-multiplier tubes and a custom designed software program allow for the recording of simultaneous dose measurements.

Anthropomorphic Phantoms

These dose profiles at the center and peripheries of CTDI phantoms indicate the differences in dose delivery to organs within the body, and will be improved with applications with anthropomorphic phantom. Such a series of anatomical physical phantoms have been fabricated for research applications at the University of Florida (UF).^{51,52} A unique feature of this family of phantoms is that each one has been developed to correspond precisely with a complementary computational model, permitting a direct correlation of organ dosimetry between computational simulations and empirical measurements for identical models. The phantom series has been constructed to represent a range of ages and incorporates real-time dosimeters for a large number of organ locations in order to perform rapid measurements of both specific organ doses and Effective Dose.⁵³⁻⁵⁷

The early phantoms demonstrated the value of a physical phantom that could be utilized for dosimetry measurements at a wide variety of clinical facilities, and were the first to incorporate an array of immediate read-out dosimeters that facilitated the examination of doses for a series of radiographic examinations and varying techniques.⁵⁸ Since the phantoms were

also identically matched to a computational model, they also provided a unique opportunity to benchmark and compare the results of physical measurements with computational simulations.⁵⁹ More recent investigations have focused on doses delivered from helical and MDCT systems. *Jones*⁵⁶ performed a comprehensive evaluation of the effect of CT acquisition parameters on organ doses and Effective Dose of a newborn. Currently, a series of adult physical phantoms are under development to evaluate the absorbed dose associated with CT image acquisitions in both male and female patients.

Final Thoughts

Fiber-optic coupled dosimeters provide the potential for improvements in standard CT dosimetry where pencil ion chamber methods fail to sufficiently measure the scatter radiation associated with large diameter phantoms and longer, more clinically relevant scan lengths. Helical scan dose profiles measured with FOC dosimeters differentiate the primary radiation from the scatter contributions associated with a given CT system to evaluate the effect of specific scanner parameters on patient absorbed dose. The potential to measure specific organ dose and effective dose measurements using fiber-optic dosimeters along with anatomical physical phantoms can allow a description of CT dose beyond the limits of standard dosimetr

LIST OF REFERENCES

1. American Association of Physicists in Medicine, AAPM Report 96, "The Measurement, Reporting, and Management of Radiation Dose in CT" (AAPM, College Park, MD, 2008).
2. FDA, "FDA public health notification, reducing radiation risk of computed tomography for pediatric and small adult patients," *Pediatr. Radiol.* **32**, 314-216 (2002).
3. E. L. Nickoloff, and P. O. Alderson, "Radiation exposures to patients from CT. Reality, public perception, and policy," *AJR Am. J. Radiol.* **177**, 285-287 (2001).
4. H. Hu, "Multi-slice helical CT, Scan and reconstruction," *Med. Phys.* **26**, 5-18 (1999).
5. C. H. McCollough, and F. E. Zink, "Performance evaluation of a multi-slice CT system," *Med. Phys.* **26**, 2223-2230 (1999).
6. T. G. Flohr, K. Stierstorfer, S. Ulzheimer, H. Bruder, A. N. Primak, and C. H. McCollough, "Image reconstruction and image quality evaluation for a 64-slice CT scanner with z-flying focal spot," *Med. Phys.* **32**, 2536-2547 (2005).
7. T. G. Flohr, S. Schaller, K. Stierstorfer, H. Bruder, B. M. Ohnesorge, and U. J. Schoepf, "Multi-detector row CT systems and image-reconstruction techniques," *Radiology* **235**, 756-773 (2005).
8. S. Mori, M. Endo, T. Tsunoo, S. Kandatsu, S. Tanada, H. Aradate, Y. Saito, H. Miyazaki, K. Satoh, S. Matsushito, and M. Kusakabe, "Physical performance evaluation of a 256-slice CT-scanner for four-dimensional imaging," *Med. Phys.* **31**, 1348-1356, (2004).
9. IMV, "Benchmark Report CT," (In: Young L, ed. Des Plaines, IL, IMV Medical Information Division, Inc., 2006) www.IMVinfo.com.
10. O.W. Linton, and F.A. Mettler, Jr., "National conference on dose reduction in CT, with an emphasis on pediatric patients," *AJR Am. J. Roentgenol.* **181**, 321-329, (2003).
11. F.A. Mettler, Jr., P. W. Wiest, J. A. Locken, and C. A. Kelsey, "CT scanning: Patterns of use and dose," *J. Radiol. Prot.* **20**, 353-359, (2000).
12. J. T. Bushberg, J. A. Seibert, E. M. Leidholdt, and J. M. Boone, *The Essential Physics of Medical Imaging*, (Lippincott Williams & Wilkins, Philadelphia, Pennsylvania, 2002).
13. International Atomic Energy Agency, IAEA Safety Series No. 115, "International Basic Safety Standards for Protection Against Ionizing Radiation and for the Safety of Radiation Sources" (IAEA, Vienna, Austria, 1996).
14. American Association of Physicists in Medicine, AAPM Report 74, "Quality Control in Diagnostic Radiology," (AAPM, Chicago, IL, 2002).

15. U.S. FDA Code of Federal Regulations, "Diagnostic x-ray systems and their major components," 21 CFR 1020.33, Govt. Printing Office, 1984.
16. American Association of Physicists in Medicine, AAPM Report 31, "Standardized Methods for Measuring Diagnostic X-ray Exposures," (AAPM, New York, 1990).
17. American Association of Physicists in Medicine, AAPM Report 39, "Specification and Acceptance Testing of Computed Tomography Scanners," (AAPM, New York, 1993).
18. International Electrotechnical Commission, International Standard 61223-2-6, "Evaluation and Routine Testing in Medical Imaging Department, Part 2-6: Constancy Tests - X-ray Equipment for Computed Tomography," (IEC, Geneva, Switzerland, 1994).
19. American Association of Physicists in Medicine, AAPM Report 1, "Phantoms for Performance Evaluation and Quality Assurance of CT Scanners," (AAPM, Chicago, IL, 1997).
20. K. A. Jessen, W. Panzer, P. C. Shrimpton, et al., EUR 16262, European Guidelines on Quality Criteria for Radiological and Electromedical Healthcare IT Industry (COCIR), Frankfurt, 2000
21. International Electrotechnical Commission, International Standard 60601-2-44, Edition 2.1, "Medical Electrical Equipment - Part 2-44: Particular Requirements for the Safety of X-Ray Equipment for Computed Tomography" (IEC, Geneva, Switzerland, 2001).
22. H. Y. Tsai, C. J. Tung, M. H. Huang, and Y. L. Wan, "Analyses and applications of single scan dose profiles in computed tomography," *Med. Phys.* **30**, 1982-1989 (2003).
23. T. Cheung, Q. Cheng, D. Feng, M. J. Stokes, "Study on examinee's dose delivered in computed tomography," *Phys. Med. Biol.* **46**, 813-820 (2001).
24. T. B. Shope, R. M. Gagne, and G. C. Johnson, "A method for describing the doses delivered by transmission x-ray computed tomography," *Med. Phys.* **8**, 488-495 (1981).
25. J. M. Boone, "The trouble with CTDI 100," *Med. Phys.* **34**, 1364-1371 (2007).
26. R. L. Dixon, "A new look at CT dose measurement, Beyond CTDI," *Med. Phys.* **30**, 1272-1280 (2003).
27. J. M. Boone, V. N. Cooper III, W. R. Nemzek, J. P. McGahan, J. A. Seibert, "Monte Carlo assessment of computed tomography dose to tissue adjacent to the scanned volume," *Med. Phys.* **27**, 2393-2407 (2000).
28. J. Hecht, *Understanding Fiber Optics*, (Pearson Education, Inc., Upper Saddle River, NJ, 2006).

29. A. L. Huston, B. L. Justus, P. L. Falkenstein, R. W. Miller, H. Ning, and R. Altemus, "Remote optical fiber dosimetry," *Nucl. Instrum. Methods Phys. Res. B* **184**, 55–67 (2001).
30. A. L. Huston, B. L. Justus, P. L. Falkenstein, R. W. Miller, H. Ning, and R. Altemus, "Optically stimulated luminescent glass optical fiber dosimeter," *Radiat. Prot. Dosim.* **101**, 23–26 (2002).
31. B.L. Justus, C. D. Merritt, K. J. Pawlovich, A. L. Huston, and S. Rychnovsky, "Optically stimulated luminescence dosimetry using doped fused quartz," *Radiat. Prot. Dosim.* **84**, 189–192 (1999).
32. B. L. Justus, P.L. Falkenstein, A. L. Huston, M. C. Plazas, H. Ning, and R. W. Miller, "Gated fiber-optic-coupled detector for in vivo real-time radiation dosimetry," *Optical Society of America* **43** (8), 1663-1668 (2004).
33. M. J. Marrone, *Appl. Phys. Lett.* **38** (3) 115 (1981).
34. www.oceanoptics.com
35. R. D. Evans, *The Atomic Nucleus*, (Krieger Publishing Company, Inc., Malabar, FL, 1982).
36. K. Ursel, and A. Richards A, Kodak Publication No. M3-103, "Kodak MIN-R 2000 Mammography Screen/Film Systems User Guide," (Eastman Kodak Company, 2006).
37. W. E. Moore, R. Dickerson, and D. Steklenski, "Design and performance features of a new mammographic film/screen system," No. 54, *Proc. SPIE*, 5368 (2004).
38. www.e-radiography.net/radtech/f/film.htm
39. Hamamatsu Photonics K.K., "Hamamatsu Preliminary Data: Photon Counting Head with Microcontroller and RS-232C Interface, H7467 Series," (Nov. 1999). www.hamamatsu.com
40. G. F. Knoll, *Radiation Detection and Measurement*, (John Wiley & Sons, Inc., New York, 2000).
41. M. Mahesh, J. C. Scatarige, J. Cooper, and E. K. Fishman, "Dose and pitch relationship for a particular multi-slice CT scanner," *AJR Am. J. Roentgenol.* **177**, 1273-1275 (2001).
42. MHRA Evaluation Report MDA 04037, "ImPACT Report: Siemens SOMATOM Sensation 16 CT Scanner," (MHRA, London, 2004).
43. W. Huda, "Dose and image quality in CT," *Pediatr. Radiol.* **32**, 709-713 (2002).
44. D. J. Brenner, E. J. Hall, and D. Phil, "Computed tomography – an increasing source of radiation exposure," *N. Eng. J. Med.* **357**, 2277-2284 (2007).

45. D. J. Brenner DJ, "Is it time to retire the CTDI for CT quality assurance and dose optimization?" *Med. Phys.* **32**, 3225-3226 (2005).
46. D. J. Brenner, C. H. McCollough, and C. G. Orton, "Is it time to retire the computed tomography dose index (CTDI) for CT quality assurance and dose optimization," *Med. Phys.* **33**, 1189-1191 (2006).
47. K. D. Nakonechny, B. G. Fallone, and S. Rathee, "Novel methods of measuring single scan dose profiles and cumulative dose in CT," *Med. Phys.* **32**, 98-109 (2005).
48. R. L. Dixon, M. T. Munley, and E. Bayram, "An improved analytical model for CT dose simulation with a new look at the theory of CT dose," *Med. Phys.* **32**, 3712-3728 (2005).
49. R. L. Dixon, and A. C. Ballard, "Experimental validation of a versatile system of CT dosimetry using a conventional ion chamber: Beyond CTDI₁₀₀," *Med. Phys.* **34** (8), 3399-3413 (2007).
50. H. Zhou, and J. M. Boone, "Monte Carlo evaluation of CTDI_∞ in infinitely long cylinders of water, polyethylene and PMMA with diameters from 10 mm to 500 mm," *Med. Phys.* **35** (6), 2424-2431 (2008).
51. M. A. Tressler, D. E. Hintenlang, "Construction of a newborn dosimetry phantom for measurement of effective dose," *Health Phys.* **76** (6) S190 (1999).
52. A. K. Jones, T. A. Simon, W. E. Bolch, M. M. Holman, and D. E. Hintenlang, "A tomographic physical phantom of the newborn patient with real-time dosimetry I: Methods and techniques for construction," *Med. Phys.* **33** (9) 3274-3282 (2006).
53. M. Bower, and D. E. Hintenlang, "The characterization of a commercial MOSFET dosimeter system for use in diagnostic x-ray," *Health Phys.* **75**, 197-204 (1998).
54. A. K. Jones, F. D. Pazik, D. E. Hintenlang, and W. E. Bolch, "MOSFET dosimeter depth-dose measurements in heterogeneous tissue-equivalent phantoms at diagnostic x-ray energies," *Med. Phys.* **32** (10), 3209-3213 (2005).
55. R. J. Staton, A. K. Jones, C. Lee, D. E. Hintenlang, M. M. Arreol, J. L. Williams, and W. E. Bolch, "A tomographic physical phantom of the newborn child with real-time dosimetry II: Scaling factors for calculation of mean organ dose in pediatric radiography," *Med. Phys.* **33** (9), 3283-3289 (2006).
56. A. K. Jones, "Dose versus image quality in pediatric radiology, Studies using a tomographic newborn physical phantom with an incorporated dosimetry system," Ph.D. Dissertation, University of Florida, Gainesville, FL (2006).
57. A. K. Jones, A. L. Huston, P. L. Falkenstein, and D. E. Hintenlang, "Evaluation of a fiber optic coupled dosimeter for use in computed tomography dose measurements," *Radiat. Prot. Dosimetry*; In Review (2008).

58. K. M. Hintenlang, J. L. Williams, and D. E. Hintenlang DE, "A survey of radiation dose associated with pediatric diagnostic x-ray," *Pediatr. Radiol.* **32**, 771-777 (2002).
59. J. B. Sessions, J. N. Roshau, M. A. Tressler, D. E. Hintenlang, M. M. Arreola, J. L. Williams, L. G. Bouchet, and W. E. Bolch WE, "Organ doses in pediatric radiology: A comparison of an anthropomorphic physical phantom with MOSFET dosimetry and a computational patient model," *Med. Phys.* **29** (6) (2002).

BIOGRAPHICAL SKETCH

William Edward Moloney was born in Brooklyn, New York, on May 1, 1982, to William and Jane Moloney. He is one of five children including his older sister Liz and three younger brothers Matthew, John, and Robert. He attended Xaverian High School in Brooklyn, New York, graduating in 2000. He then earned his Bachelor of Science degree in physics in 2004 from Saint Joseph's University in Philadelphia, Pennsylvania. In August 2008, he received his Master of Science degree in nuclear engineering sciences with a concentration in medical physics from the University of Florida in Gainesville, Florida.